

AD-A192 357

DTIC FILE COPY



**RADC-TR-87-54**  
**Final Technical Report**  
**August 1987**

**THERMOCHEMISTRY OF DISPENSER  
CATHODE IMPREGNANT MATERIALS:  
Phase Equilibria In The  
BaO-CaO-Al<sub>2</sub>O<sub>3</sub> System**

Georgia Institute of Technology

DTIC  
ELECTE  
MAR 11 1988  
S D

D. N. ... ..

APPROVED FOR PUBLIC RELEASE; DISTRIBUTION UNLIMITED

**ROME AIR DEVELOPMENT CENTER**  
**Air Force Systems Command**  
**Griffiss Air Force Base, NY 13441-5700**

88 3 7 103

**Best  
Available  
Copy**

This report has been reviewed by the RADC Public Affairs Office (PA) and is releasable to the National Technical Information Service (NTIS). At NTIS it will be releasable to the general public, including foreign nations.

RADC-TR-87-54 has been reviewed and is approved for publication.

APPROVED: *Edward J. Daniszewski*

EDWARD J. DANISZEWSKI  
Project Engineer

APPROVED: *David J. Pratt*

DAVID J. PRATT, Colonel, USAF  
Director of Surveillance

FOR THE COMMANDER:

*John A. Ritz*

JOHN A. RITZ  
Directorate of Plans & Programs

If your address has changed or if you wish to be removed from the RADC mailing list, or if the addressee is no longer employed by your organization, please notify RADC (OCTP) Griffiss AFB NY 13441-5700. This will assist us in maintaining a current mailing list.

Do not return copies of this report unless contractual obligations or notices on a specific document require that it be returned.

UNCLASSIFIED

SECURITY CLASSIFICATION OF THIS PAGE

REPORT DOCUMENTATION PAGE				Form Approved OMB No. 0704-0188	
1a. REPORT SECURITY CLASSIFICATION UNCLASSIFIED			1b. RESTRICTIVE MARKINGS N/A		
2a. SECURITY CLASSIFICATION AUTHORITY N/A			3. DISTRIBUTION/AVAILABILITY OF REPORT Approved for public release; distribution unlimited		
2b. DECLASSIFICATION/DOWNGRADING SCHEDULE N/A			5. MONITORING ORGANIZATION REPORT NUMBER(S) RADC-TR-87-54		
4. PERFORMING ORGANIZATION REPORT NUMBER(S) N/A			7a. NAME OF MONITORING ORGANIZATION Rome Air Development Center (OCTP)		
6a. NAME OF PERFORMING ORGANIZATION Georgia Institute of Technology		6b. OFFICE SYMBOL (if applicable)		7b. ADDRESS (City, State, and ZIP Code) Griffiss AFB NY 13441-5700	
6c. ADDRESS (City, State, and ZIP Code) School of Materials Engineering Atlanta GA 30332		9. PROCUREMENT INSTRUMENT IDENTIFICATION NUMBER F30602-81-C-0185			
8a. NAME OF FUNDING/SPONSORING ORGANIZATION Rome Air Development Center		8b. OFFICE SYMBOL (if applicable)		10. SOURCE OF FUNDING NUMBERS	
8c. ADDRESS (City, State, and ZIP Code) Griffiss AFB NY 13441-5700		PROGRAM ELEMENT NO. 62702F		PROJECT NO. 4506	TASK NO. 12
				WORK UNIT ACCESSION NO. PB	
11. TITLE (Include Security Classification) THERMOCHEMISTRY OF DISPENSER CATHODE IMPREGNANT MATERIALS: PHASE EQUILIBRIA IN THE BaO-CaO-Al <sub>2</sub> O <sub>3</sub> SYSTEM					
12. PERSONAL AUTHOR(S) D.N. Hill, R.E. Hann, P.R. Smith					
13a. TYPE OF REPORT Final		13b. TIME COVERED FROM Feb 86 to Sep 86		14. DATE OF REPORT (Year, Month, Day) August 1987	
				15. PAGE COUNT 204	
16. SUPPLEMENTARY NOTATION N/A					
17. COSATI CODES			18. SUBJECT TERMS (Continue on reverse if necessary and identify by block number)		
FIELD	GROUP	SUB-GROUP	Phase Equilibria, Phase Diagram		
18	04		Barium-Calcium-Aluminate System,		
20	10, 12		Subsolidus		
19. ABSTRACT (Continue on reverse if necessary and identify by block number)					
<p>The goal of this study was to establish the subsolidus and liquid-solid equilibrium relationships in the high-baria portion of the barium calcium aluminate system.</p> <p>The solidus and liquidus temperatures were determined for forty different compositions. From these data, the liquidus and solidus surfaces were characterized and presented in the form of a ternary diagram. Four vertical (isoplethic) sections were also constructed which describe the crystallization sequences along non-binary planes in the system.</p> <p>Two isothermal sections were constructed describing the subsolidus equilibria in the high-baria corner at 1100°C and 1475°C. The solubility of calcium in the crystal structures of Ba<sub>2</sub>Al<sub>2</sub>O<sub>7</sub> and Ba<sub>3</sub>Al<sub>2</sub>O<sub>6</sub> was 20.5 and 18.8 mole percent respectively and was found to be independent of temperature over the range 1100°C to 1475°C. The unit cell dimensions of two polymorphic modifications of the Ba<sub>4-x</sub>C<sub>x</sub>Al<sub>2</sub>O<sub>7</sub> solid series were determined along with the unit cell of B<sub>5</sub>A.</p> <p style="text-align: right;">(Key words: Yover)</p>					
20. DISTRIBUTION/AVAILABILITY OF ABSTRACT <input checked="" type="checkbox"/> UNCLASSIFIED/UNLIMITED <input type="checkbox"/> SAME AS RPT <input type="checkbox"/> DTC USERS			21. ABSTRACT SECURITY CLASSIFICATION UNCLASSIFIED		
22a. NAME OF RESPONSIBLE INDIVIDUAL Edward J. Daniszewski			22b. TELEPHONE (Include Area Code) (315) 330-4381		22c. OFFICE SYMBOL RADC (OCTP)

DD Form 1473, JUN 86

Previous editions are obsolete.

SECURITY CLASSIFICATION OF THIS PAGE

UNCLASSIFIED

UNCLASSIFIED

Block 18. Abstract (Cont'd)

The melting point of BaO (2250°C) was determined by in-situ oxidation of barium metal using a controlled atmosphere tungsten-strip microfurnace. Finally, a calculation BaO-CaO binary generated from molal freezing-point depression theory and end-member melting points and heats of fusion is presented.

UNCLASSIFIED

# TABLE OF CONTENTS

	<u>Page</u>
LIST OF TABLES . . . . .	iv
LIST OF ILLUSTRATIONS . . . . .	vi
SUMMARY . . . . .	xi

## Chapter

I INTRODUCTION . . . . .	1
II SURVEY OF LITERATURE . . . . .	8
Thermal Analysis	
Microfurnace for Melting Point	
Determinations	
BaO-Al <sub>2</sub> O <sub>3</sub> System	
CaO-Al <sub>2</sub> O <sub>3</sub> System	
BaO-CaO System	
BaO-CaO-Al <sub>2</sub> O <sub>3</sub> System	
Experimental Difficulties Associated	
with BaO	
Crystallography of Barium Aluminates	
III PROCEDURE . . . . .	53

Sample Preparation	
Isothermal Heat Treatments	
Microfurnace Operation	
Equipment	
Vacuum System	
Strip Heater	
Temperature Measurement	
Power Supply	
X-ray Analysis	
Scanning Electron and Optical Microscopy	
Differential Thermal Analysis	
Oxidation of Barium Metal	
Reaction of Barium Calcium Aluminates	
with Tungsten	



Accession For	
DTIS GRA&I	<input checked="" type="checkbox"/>
DTIC TAB	<input type="checkbox"/>
Unannounced	<input type="checkbox"/>
Justification	
By	
Distribution/	
Availability Codes	
Dist	Avail and/or Special
A-1	

IV RESULTS AND DISCUSSION . . . . .	74
-------------------------------------	----

Subsolidus Equilibria	
Solid Solubility Limits and Alkemade	
Lines at 1475°C	
Equilibria at 1100°C	
Verification of Equilibrium at 1100°C	
Polymorphism in the BCA System	
Polymorphism of $B_{4-x}C_xA$ Solid Solutions	
Comparison of Diagrams with Previous	
Investigations	
Crystallography of Barium Calcium	
Aluminate Phases	
Interpretation of Heating and Cooling Curves	
Solidus and Liquidus Temperature	
Determinations	
Vertical Section at 25 Mole Percent $Al_2O_3$	
Vertical Section at 20 Mole Percent $Al_2O_3$	
Vertical Section from $B_3A$ to $CaO$	
Vertical Section at 15 Mole Percent $Al_2O_3$	
Crystallization and Microstructure	
Melting Point Determination of Barium Oxide	
Calculation of the $BaO-CaO$ Binary Diagram	
Determination	

V CONCLUSIONS . . . . .	162
-------------------------	-----

## APPENDIX

XRD Data for Various Barium Calcium	
Aluminate Compositions . . . . .	165

BIBLIOGRAPHY . . . . .	183
------------------------	-----

## LIST OF TABLES

<u>Table</u>	<u>Page</u>
2.1 Compounds and Eutectic Compositions As Found by Purt (18) and the Toropov and Galachov (17) . . . . .	21
2.2 XRD Patterns for B <sub>4</sub> A, B <sub>5</sub> A, B <sub>7</sub> A, B <sub>8</sub> A and B <sub>10</sub> A by Appendino (19) . . . . .	25
2.3 Solidus and Liquidus Temperatures of BCA Compositions by Asselanis (11) . . . . .	40
2.4 Solidus and Liquidus Temperatures of BCA Compositions by Tarter (12) . . . . .	43
3.1 Compositions Used for Solidus and Liquidus Determinations. . . . .	54
4.1 Crystal Data for B <sub>3</sub> CA Type I and Type II Polymorphs . . . . .	103
4.2 Crystal Data for B <sub>3</sub> A and B <sub>3</sub> A <sub>SS1</sub> . . . . .	103
4.3a Solidus and Liquidus Temperatures of Compositions along the Constant 25 Mole Percent Al <sub>2</sub> O <sub>3</sub> Plane . . . . .	116
4.3b Solidus and Liquidus Temperatures along the B <sub>3</sub> A-CaO Psuedo-Binary . . . . .	117
4.3c Solidus and Liquidus Temperatures along the Constant 20 Mole Percent Al <sub>2</sub> O <sub>3</sub> Plane . . . . .	118
4.3d Solidus and Liquidus Temperatures along the Constant 15 Mole Percent Al <sub>2</sub> O <sub>3</sub> Plane . . . . .	119
4.4 Ternary Eutectic Compositions and Temperatures . . . . .	122
A-1 XRD Data for B <sub>3</sub> A Quenched from above the Liquidus . . . . .	166



<u>Table</u>		<u>Page</u>
A-2	XRD Data for $B_{3.70}C_{0.30}A$ Quenched from 1100°C/1 Hour Soak . . . . .	168
A-3	XRD Data for $B_4A$ Quenched from 1100°C/1 Hour Soak . . . . .	170
A-4	XRD Data for $B_{2.5}C_{0.5}A$ Quenched from above the Liquidus . . . . .	172
A-5	XRD Data for $B_3CA$ Quenched from 1100°C/1 Hour Soak . . . . .	174
A-6	XRD Data for $B_{3.38}C_{0.63}A$ Quenched from 1100°C/1 Hour Soak . . . . .	176
A-7	XRD Data for $B_3CA$ Quenched from above Liquidus . . . . .	178
A-8	XRD Data for $B_{3.70}C_{0.92}A$ Quenched from 1100°C/1 Hour Soak . . . . .	179
A-9	XRD Data for $B_{3.47}C_{0.79}A$ Quenched from 1100°C/1 Hour Soak . . . . .	181

## LIST OF ILLUSTRATIONS

Figure	Page
2.1 DTA Curves of (a) a Eutectic Mixture, (b) a Mixture Lying Between a Eutectic and a Congruently Melting Compound, (c) a Composition lying Near a Eutectic (3) . . . . .	11
2.2 Theoretical Heating Curves Developed by Wisnyi (5) . . . . .	13
2.3 Heating Curve Interpretation by Latta and Fryxell (6) . . . . .	15
2.4 Phase Diagram of the BaO-Al <sub>2</sub> O <sub>3</sub> System by Toropov and Galachov (17) . . . . .	20
2.5 Phase Diagram of the BaO-Al <sub>2</sub> O <sub>3</sub> System by Purt (18) . . . . .	22
2.6 Sub-solidus BaO-Al <sub>2</sub> O <sub>3</sub> Phase Diagram by Appendino (19) . . . . .	24
2.7 Phase Diagram of the BaO-Al <sub>2</sub> O <sub>3</sub> System by Lambert (1) . . . . .	28
2.8 Comparison of Previous BaO-Al <sub>2</sub> O <sub>3</sub> Phase Diagrams. . . . .	29
2.9 CaO-Al <sub>2</sub> O <sub>3</sub> System, at Normal Humidity, by Lea and Desch (21) . . . . .	31
2.10 CaO-Al <sub>2</sub> O <sub>3</sub> System, under Anhydrous Conditions, by Nurse, <u>et al.</u> (22) . . . . .	32
2.11 Partial Isothermal section at 1250°C of the BaO-CaO-Al <sub>2</sub> O <sub>3</sub> System by Brisi and Montorsi (25) . .	34
2.12 Partial Isothermal Section at 1400°C of the BaO-CaO-Al <sub>2</sub> O <sub>3</sub> System by Massazza (26) . . . . .	36

Figure		Page
2.13	Partial Isothermal Section at 1250°C of the BaO-CaO-Al <sub>2</sub> O <sub>3</sub> System by Appendino (23) . . . . .	37
2.14	Composite BaO-CaO-Al <sub>2</sub> O <sub>3</sub> Diagram Constructed by Wolten (27) . . . . .	39
2.15	Heating Curve of BaO by Asselanis (11) . . . . .	42
2.16	BaO-BaCO <sub>3</sub> System by Baker (29) . . . . .	46
3.1	Schematic Diagram of Furnace System . . . . .	58
3.2	Photograph of Microfurnace . . . . .	59
3.3	Close-up View of Electrode-Strip-Thermocouple Assembly . . . . .	60
3.4	Heating Curve for Al <sub>2</sub> O <sub>3</sub> . . . . .	64
4.1	Partial Isothermal Section at 1475°C of the BaO-CaO-Al <sub>2</sub> O <sub>3</sub> System . . . . .	76
4.2	Partial Isothermal Section at 1100°C of the BaO-CaO-Al <sub>2</sub> O <sub>3</sub> System . . . . .	77
4.3	Plot of a <sub>o</sub> of B <sub>3-x</sub> C <sub>x</sub> A versus Calcium Content at 1475°C . . . . .	78
4.4	Plot of the (400) Interplaner Spacing of B <sub>4-x</sub> C <sub>x</sub> A Versus Calcium Content at 1475°C . . . . .	81
4.5	Plot of a <sub>o</sub> of B <sub>3-x</sub> C <sub>x</sub> A Versus Calcium Content at 1100°C . . . . .	85
4.6	Plot of the (400) Interplaner Spacing of B <sub>4-x</sub> C <sub>x</sub> A Versus Calcium Content at 1100°C . . . . .	86
4.7	Comparison of the XRD Traces of B <sub>4-x</sub> C <sub>x</sub> A Solid Solutions Showing the Effect of Calcium Substitution in the Lattice . . . . .	87

Figure		Page
4.8	XRD Traces of (a) $B_{3.47}C_{0.79}A$ and (b) $B_{3.70}C_{0.92}A$ quenched from $1100^{\circ}C$ . . . . .	90
4.9	DTA Curve for Pure $B_3A$ Showing Heat Effect of Polymorphic Transformation . . . . .	92
4.10	XRD Traces containing the (800) and (840) Reflection Groups for (a) Pure $B_3A$ and (b) $B_{3.80}C_{0.20}A$ Solid Solution . . . . .	96
4.11	Partial Sub-solidus Vertical Section Containing the $B_{3-x}C_xA$ Solid Solution Series . . . . .	97
4.12	Comparison of the XRD Traces of the Two Polymorphic Forms of $B_{4-x}C_xA$ containing 20 Mole Percent . . . . .	99
4.13	Comparison of the XRD Traces of $B_4A$ and $B_{3.80}C_{0.20}A$ . . . . .	106
4.14	DTA Curve for a 50%Pb-50%Sn Mixture Showing Heat Effect Resulting from Melting . . . . .	108
4.15	Heating Curve of $B_{3.00}C_{0.88}A$ Showing Thermal Arrest . . . . .	111
4.16	Partial Ternary Diagram of the BaO-CaO- $Al_2O_3$ System Showing Location of Compositions used in Solidus/Liquidus Determinations . . . . .	115
4.17	Projection of the Liquidus Surface onto the $1475^{\circ}C$ Isothermal Section for the High-BaO Portion of the BaO-CaO- $Al_2O_3$ System . . . . .	120
4.18	Vertical Section at the 25 Mole Percent $Al_2O_3$ Plane . . . . .	123

Figure	Page
4.19 Illustration of the Relationship between the Vertical Section at the 25 Mole percent $\text{Al}_2\text{O}_3$ Plane and the BCA Ternary Diagram . . . . .	124
4.20 Vertical Section at the 20 Mole Percent $\text{Al}_2\text{O}_3$ Plane . . . . .	130
4.21 Illustration of the Relationship between the Vertical Section at the 20 Mole Percent $\text{Al}_2\text{O}_3$ Plane and the BCA Ternary Diagram . . . . .	131
4.22 Revised Portion of the $\text{BaO-Al}_2\text{O}_3$ Diagram Showing the Congruently Melting Compound $\text{B}_4\text{A}$ . . .	133
4.23 Vertical Section Along the $\text{B}_3\text{A-CaO}$ Pseudo-binary . . . . .	136
4.24 Illustration of the Relationship between the Vertical Section Vertical Section along the $\text{B}_3\text{A-CaO}$ Pseudo-binary and the BCA Ternary Diagram . . . . .	137
4.25 Vertical Section at the 15 Mole Percent $\text{Al}_2\text{O}_3$ Plane . . . . .	142
4.26 Illustration of the Relationship between the Vertical Section at the 15 Mole Percent $\text{Al}_2\text{O}_3$ Plane and the BCA Ternary Diagram . . . . .	143
4.27 Scanning Electron Micrograph of a Polished Section of $\text{B}_5\text{C}_3\text{A}_2$ . . . . .	146
4.28 EDS Spectra of (a) Dendrite and (b) Matrix Region of the Polished Section of $\text{B}_{2.75}\text{C}_{1.25}\text{A}$ . . . . .	147
4.29 Reflecting Light Micrograph of a Polished Section of $\text{B}_2\text{CA}$ . . . . .	150
4.30 Heating/Cooling Curve of $\text{BaO}$ from the In-situ Oxidation of Barium Metal . . . . .	151

4.31	Comparison of Eutactic Points in the BaO-CaO System Calculated on the Basis of Melting Point Data for BaO (a) obtained in this Study, and (b) Published by Schumacher <sup>7</sup> . . . . .	151
4.32	X-ray Diffraction Patterns for a 0.15B <sub>3</sub> A-0.85W Mixture, heat Treated at 1100°C in Ar for 2, 4, 8, 17, 34, 39, 45, 69, & 90 Hours . . . .	157
4.33	X-ray Diffraction Patterns for a 0.15B <sub>4</sub> CA-0.85W Mixture, Het Treated at 1100°C in Ar for 2, 4, 8, 17, 34, 39, 45, 69, & 90 Hours . . . .	159
4.34	X-ray Diffraction Patterns for a 0.15B <sub>6</sub> CA <sub>2</sub> -0.85W Mixture, Heat Treated at 1100°C in Ar for 2, 4, 8, 17, 34, 39, 45, 69, & 90 Hours . . . .	160
4.35	X-ray Diffraction Patterns for a 0.15B <sub>5</sub> C <sub>3</sub> A <sub>2</sub> -0.85W Mixture, Heat Treated at 1100°C in Ar for 2, 4, 8, 17, 34, 39, 45, 69, & 90 Hours . . . . .	161

## SUMMARY

Impregnated dispenser cathodes serve as the electron current sources in vacuum-tube microwave devices. These cathodes are manufactured by capillary-filling impregnation of a porous tungsten matrix with molten barium calcium aluminate compositions. Up to the present time, selection of commercial impregnant compositions has proceeded on a nearly empirical basis. This has resulted in less than ideal cathode performance due to a lack of understanding of impregnant chemistry.

The limited choices of impregnant compositions can be primarily attributed to an insufficient data base which should provide information concerning solid-state equilibria of the impregnant materials along with solid-liquid equilibrium relationships associated with melting sequences involved with cathode impregnation. The goal of this study was to establish the sub-solidus and liquid-solid equilibrium relationships in the high-baria portion of the barium calcium aluminate system.

The solidus and liquidus temperatures were determined for forty different compositions. From these data, the liquidus and solidus surfaces were characterized

and presented in the form of a ternary diagram. Four vertical (isoplethic) sections were also constructed which describe the crystallization sequences along non-binary planes in the system.

Two isothermal sections were constructed describing the sub-solidus equilibria in the high-baria corner at 1100°C and 1475°C. The solubility of calcium in the crystal structures of  $\text{Ba}_4\text{Al}_2\text{O}_7$  and  $\text{Ba}_3\text{Al}_2\text{O}_6$  was 20.5 and 18.8 mole percent respectively and was found to be independent of temperature over the range 1100°C to 1475°C. The unit cell dimensions of two polymorphic modifications of the  $\text{Ba}_{4-x}\text{Ca}_x\text{Al}_2\text{O}_7$  solid series were determined along with the unit cell of  $\text{B}_3\text{A}$ .

The melting point of  $\text{BaO}$  (2250°C) was determined by in-situ oxidation of barium metal using a controlled-atmosphere tungsten-strip microfurnace. Finally, a calculated  $\text{BaO}$ - $\text{CaO}$  binary diagram generated from molal freezing-point depression theory and end-member melting points and heats of fusion is presented.



## CHAPTER I

### INTRODUCTION

Impregnated dispenser cathodes are used as electron current sources in high-power vacuum tube electron devices. These cathodes normally provide current densities ranging from 1 to 15 A/cm<sup>2</sup>, depending on the application. Over the past decade, increased research efforts have been directed toward improving cathode performance and lifetime. The research has generally concentrated on understanding the operating mechanism of dispenser cathodes through modern surface analysis techniques and surface structure models.

The mechanism of dispensing material (normally barium or barium oxide) to the cathode surface, which involves internal thermochemical processes, has received relatively little attention compared to emitter surface studies. In order to completely understand the cathode operating mechanisms, all surface models must be complemented by accurate models describing the internal production of active species and the transport of active materials to the emitting surface.

Since tube demands vary depending on their application, it is necessary for impregnant compositions to be tailored to meet optimum cathode operating conditions. However, up to now there has not been a sufficient understanding of impregnant chemistry to adequately select proper impregnant compositions for a particular application. In the past, the primary objectives for specifying an impregnant composition for long-life, space-based travelling-wave-tube (TWT) applications included producing an adequate barium/oxygen surface coverage while avoiding excessive contamination of the tube by evaporation products which might result in electrical leakage and spurious emission. However, these objectives have only been partially met due to limited choices of compositions and lack of understanding of impregnant chemistry. Tubes for electronic warfare (EW) applications pose an even more complex and challenging problem in selecting an impregnant composition which will provide an adequate barium supply for the high current density requirements of these tubes. For these applications, the impregnant composition is considered to be the most critical specification for obtaining optimum performance and minimal tube

contamination.

An additional concern which is universal for all tube applications is the reliability of the cathodes as influenced by the reproducibility of manufacture. From the evidence obtained to date, it appears that specific choices of impregnant composition may play a major role in assuring reproducible cathode impregnation as a result of composition-controlled melting and crystallization sequences.

In 1978, research aimed at characterizing the interior thermochemistry of barium-calcium-aluminate dispenser cathodes was initiated at Ga. Tech. Early work concentrated on the chracterization of reactions involved in the production of impregnants from starting materials and the determination of melting points for several commercial impregnant compositions. As the research effort proceeded, major emphasis was placed on characterization of the chemical phase equilibria in the  $\text{BaO-CaO-Al}_2\text{O}_3$  system. The first extensive phase analysis work was performed by Lambert (1) in an investigation of the high-baria portion of the  $\text{BaO-Al}_2\text{O}_3$  binary system. This was to provide the initial basis for complete characterization of the phase

equilibria of the high-baria portion of the barium-calcium-aluminate ternary system.

The goal of this investigation was to construct sub-solidus isothermal sections describing the equilibrium relationships at 1100°C and 1475°C, and to present a ternary diagram illustrating the accurate location of primary phase fields, invariant points and temperatures, and crystallization paths. Chapter Two begins with a review of thermal analysis techniques, in particular the use of heating and cooling curves to establish solidus and liquidus temperatures. A review of the development of strip-type microfurnaces for performing melting point determinations is presented with respect to design and capabilities. This is followed by a description of previous investigations of the systems BaO-Al<sub>2</sub>O<sub>3</sub>, CaO-Al<sub>2</sub>O<sub>3</sub>, BaO-CaO and BaO-CaO-Al<sub>2</sub>O<sub>3</sub>. The experimental difficulties associated with BaO and high-baria compositions are discussed, along with the special techniques used to study baria-containing systems. Finally, the crystallography of various barium calcium aluminate phases, as reported by previous investigators, is summarized.

Chapter Three gives a detailed account of the preparation and analyses of the various BCA compositions including the determination of solid solubility limits, resulting phase assemblages, and solid-liquid equilibrium relationships. The design of the furnace, vacuum system, and temperature measurement system is also described along with special techniques used for inorganic phase identification and analysis. Finally, the mathematical methods used in determining solubility limits from XRD data and the procedure used in indexing the XRD powder patterns of various BCA phases are given.

In Chapter Four, the sub-solidus equilibrium relationships are presented in the form of isothermal sections located at  $1475^{\circ}\text{C}$  and  $1100^{\circ}\text{C}$  along the vertical temperature axis. A discussion of solid-state polymorphism in the system is given in terms of the effect on the sub-solidus equilibrium. The results of the XRD powder pattern indexing work is summarized and discussed with relation to the polymorphism of the various phases. A comparison of the sub-solidus isothermal sections with previous investigations is also given. Results of the solidus and liquidus temperature measurements are presented along with

a ternary diagram showing crystallization paths, invariant points and primary phase fields. Four vertical sections are also presented, with a discussion of their relationship to the ternary diagram. The determination of the melting point of BaO using a novel, in-situ oxidation technique is given, with a discussion of the technique and a comparison with the results of previous investigations. Finally, a calculated BaO-CaO binary diagram is presented and its relation to the ternary is considered.

In order to better understand the chemical operation of dispenser cathodes, a preliminary investigation was conducted to determine the reaction products that form in mixtures of commercial barium-calcium-aluminate impregnants and tungsten powder. The identity and thermal stability of the various phases were determined using x-ray powder diffraction (XRD) after each sample was heat treated for various times in an oxygen-free argon atmosphere.

In the following chapters, conventional cement chemistry abbreviations have been adapted for the various barium aluminate compounds and solid solutions, i.e. BaO will be indicated by the letter B, CaO will be indicated by

the letter C and  $\text{Al}_2\text{O}_3$  will be indicated by the letter A.

Formulas such as  $\text{Ba}_{3-x}\text{Ca}_x\text{Al}_2\text{O}_7$  will appear as  $\text{B}_{3-x}\text{C}_x\text{A}$ .

## CHAPTER II

### LITERATURE

This chapter contains a survey of the literature pertaining to thermal analysis theory and techniques used in determining equilibrium phase diagrams and the results of investigations on the  $\text{BaO-CaO-Al}_2\text{O}_3$  system and its associated binary systems. Thermal analysis theory is presented first, along with the design and use of a microfurnace for determining solidus and liquidus temperatures. Each individual binary system is discussed followed by a review of previous work on the ternary system. A section on the experimental difficulties associated with BaO and high-baria compositions is presented, with particular attention directed to a low-melting  $\text{BaO-BaCO}_3$  eutectic and the loss of BaO through evaporation at elevated temperatures. Finally, a section on the crystallography of the various barium calcium aluminate phases is presented, including a description of the crystal structure of the compound tri-barium aluminate.



A.        THERMAL ANALYSIS

The generation of heating and cooling curves is a classic technique for determining the temperature of phase inversions in minerals. In this method the sample temperature is the measured parameter while the sample is heated at a constant rate. Enthalpic changes such as phase inversions or chemical reactions either interrupt or increase the flow of heat from the sample to the thermocouple, and which are observed as deviations from a linear programmed heating rate. In 1909, White (2) used heating and cooling curves to study the melting and freezing curves of various minerals. He reported that melting and freezing proceeded over a range of temperatures and not at a single constant temperature as required by theory. He stated that the prime cause of the observed range of melting was the presence of impurities in the minerals. He also suggested that temperature gradients within the sample charge could also contribute to the occurrence of melting over a temperature interval. White also noted that the thermal arrests which occurred in cooling curves were more pronounced than those in heating

curves. However, materials which exhibit subcooling below the freezing point will not yield cooling curves suitable for the determination of accurate equilibrium freezing points.

Carlson (3) developed a phase equilibrium diagram for the  $\text{CaO-B}_2\text{O}_3$  system by using a differential thermocouple, with corundum as a reference. A detailed discussion of the heating curves was included in his report and the three sample curves used in his discussion are shown in Figure 2.1. The first curve (a) represents the melting of a congruently melting compound. Curve (b) represents the melting of mixtures lying between a eutectic composition and a congruently melting compound. The first endotherm was ascribed to the formation of the eutectic liquid and the solidus temperature was assigned to the first minimum.

Carlson stated that continued heating of the mixture resulted in gradual fusion of the remaining solid and consequently a gradual decrease in the differential curve. The liquidus temperature was assigned to the minimum of the second endotherm. An interpretation of these type curves is also given in Chapter 4. Curves of

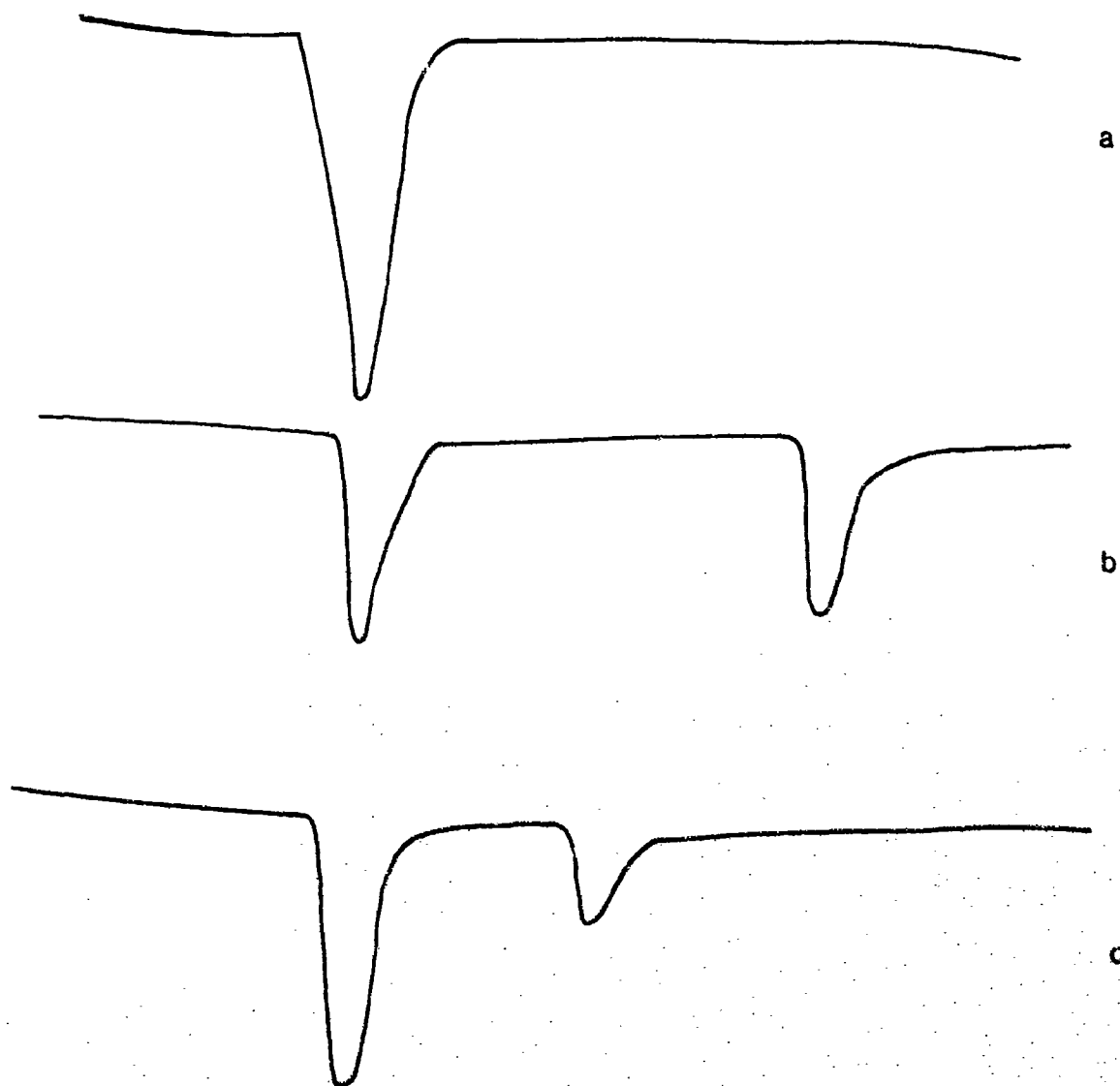


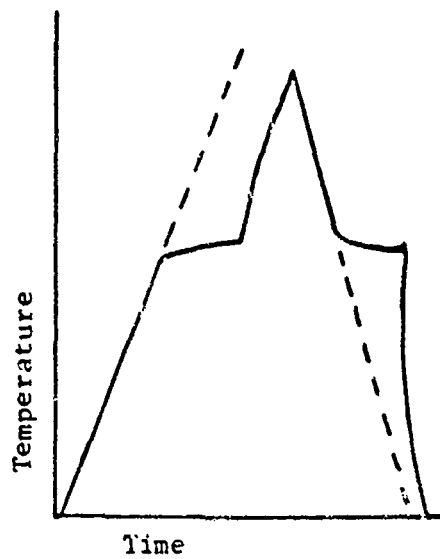
Figure 2.1. DTA Curves of (a) a Eutectic Mixture, (b) a Mixture Lying Between a Eutectic and a Congruently Melting Compound, (c) a Mixture Lying Near a Eutectic (3).

the type (c) are generated from mixtures whose composition lies closer to the eutectic composition than the congruently melting compound.

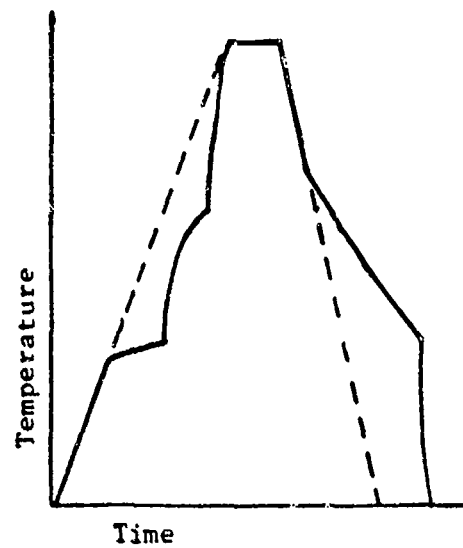
In 1951, Smyth (4) reported the results of a quantitative analysis of the temperature distributions in a thin slab of material during a phase inversion. In his model, a differential thermocouple configuration was considered, where both the sample and reference were heated from the outside at a uniform rate. A discussion of the application of his calculations to the interpretation of experimental thermal analysis data was also included.

In an investigation of the high-alumina portion of the  $\text{CaO-Al}_2\text{O}_3$  system, Wisnyi (5) used heating and cooling curves to determine solidus and liquidus temperatures. In his work he employed the quantitative theory developed by Smyth to construct theoretical heating and cooling curves for: a pure congruently melting or eutectic composition (Figure 2.2a), compositions containing both a solidus and a liquidus (Figure 2.2b), and compositions containing two solidi and a liquidus (Figure 2.2c.)

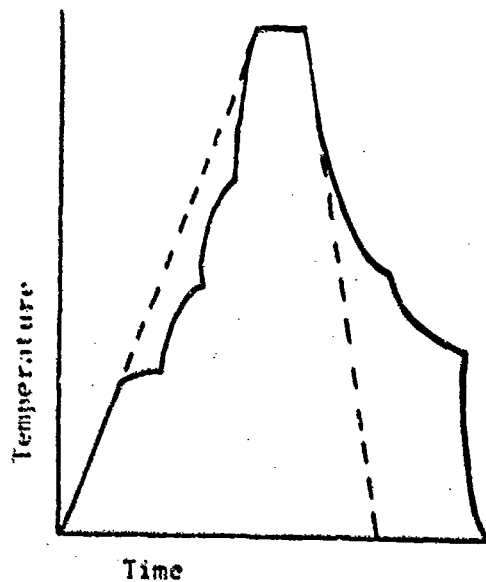
In work on liquid/solid equilibrium in the  $\text{UO}_2\text{-x}$  system Latta and Fryxell (6) used heating and cooling



(a) Congruently melting or eutectic composition.



(b) Composition with a solidus and liquidus.



(c) Composition with two solidi and one liquidus.

Figure 2.2. Theoretical Heating Curves Developed by Wisnyi (5).

curves generated by an automatic recording optical pyrometer to determine solidus and liquidus temperatures. Figure 2.3 shows their interpretation of the solidus and liquidus events. They assigned the solidus as the initial deviation from a straight line extension of the slope of the programmed heating rate. The liquidus temperature was taken as the intersection of the straight line extension of the slope of the arrest plateau and a straight line extension of the recovery portion of the heating curve.

B. MICROFURNACE FOR MELTING POINT DETERMINATIONS

Schumacher (7) reported using a tungsten strip microfurnace in determining the melting points of BaO, SrO and CaO. The strip measured 3.8 cm. long, 0.635 cm. wide and 0.025 mm. thick and had a 2 cm. uniform temperature zone. Although he did not discuss the maximum temperature capability of the furnace, the melting point of CaO was determined at 2516°C. In 1930, Roberts and Morey (8) described a microfurnace capable of attaining a maximum temperature of 1835°C. The heating element of the microfurnace was a strip of alloy having the composition of 60% platinum-40% rhodium. The strip was 0.01 mm. thick and

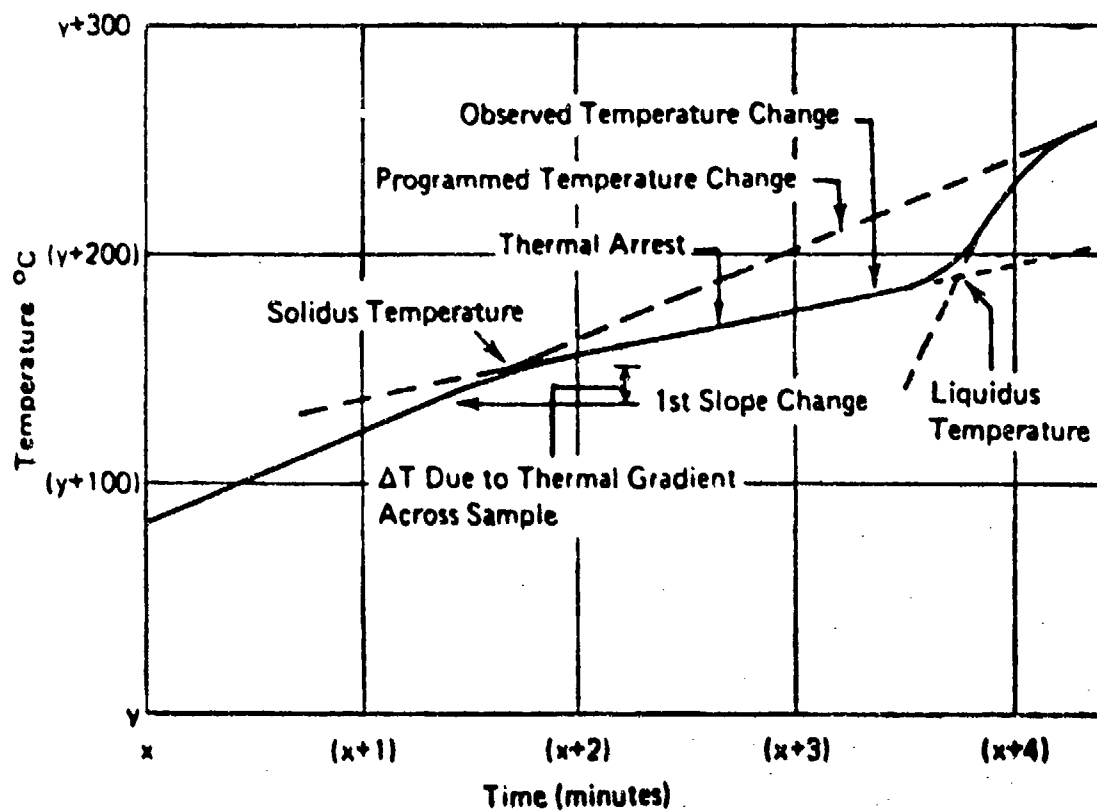


Figure 2.3. Heating Curve Interpretation by Latta and Fryxell (6).

8 mm. wide and was formed in the shape of a "U". Another advantage aside from the high temperature capability was the ability to heat and cool rapidly (allowing quenching during cooling). Roberts and Morey also discussed the presence of thermal gradients in samples heated on strips and the uncertainties associated with measuring strip temperatures by optical methods.

Keith and Roy (9) modified the Roberts-Morey microfurnace design for performing melting and quenching studies on binary oxides containing tri-valent metal cations. In their furnace the 60% platinum-40% rhodium strip was re-dimensioned in a smaller configuration which was supported by thin copper cooling fins. The furnace was used for heating in the temperature range of 1650 to 1900°C. The same microfurnace design was used by Rase and Roy (10) in 1955 in an investigation of the  $\text{BaO-TiO}_2$  system. An optical pyrometer was used to measure the temperature of the strip furnace. The solidus temperatures were reported with an accuracy of  $\pm 10^\circ\text{C}$ . The modified Roberts-Morey design was used again in a phase equilibria study of the  $\text{BaTiO}_3\text{-SrTiO}_3$  system. An accuracy of  $15^\circ\text{C}$



was assigned to solidus and liquidus measurements obtained by optical methods and on certain runs the accuracy was increased to  $\pm 5^{\circ}$  C by attaching a Pt-Pt/10% Rh thermocouple directly to the strip heater.

In 1979, Asselanis (11) built a microfurnace that was used to determine solidus and liquidus temperatures in the BaO-CaO-Al<sub>2</sub>O<sub>3</sub> system. The microfurnace could operate in a controlled atmosphere and attain a maximum temperature of 2200°C. The furnace design featured a tungsten strip heater positioned between two water-cooled copper electrodes. The electrodes were connected to copper rods supported by a brass top plate. Power was supplied to the electrode assembly by a transformer, controlled by a variable autotransformer. The strip temperature was monitored by a type C, tungsten-tungsten/26% rhenium thermocouple. The thermocouple output was recorded on a strip chart recorder and the solidus and liquidus temperatures were determined by examining the generated heating and cooling curves. This furnace design was modified by Tarter (12) by improving the cooling system and using a cam-driven temperature programmer to provide a more nearly linear heating rate. He also provided a calibration

for the type C thermocouple by comparing observed and published melting points of 99.997% pure single crystal sapphire.

C. BaO-Al<sub>2</sub>O<sub>3</sub> SYSTEM

In 1925, Schumacher (7) determined the melting point of BaO using a tungsten strip microfurnace. The barium oxide was obtained by decomposing the carbonate under vacuum in the microfurnace. The temperature was monitored with an optical pyrometer and the melting point was determined to be 1915°C. The existence of a 1:1 compound (BaAl<sub>2</sub>O<sub>4</sub>) containing BaO and Al<sub>2</sub>O<sub>3</sub> was first reported by Wartenberg and Rensch (13) in 1932. Toropov (14) reported three compounds in the BaO-Al<sub>2</sub>O<sub>3</sub> system; BA, B<sub>3</sub>A, BA<sub>6</sub>. An x-ray investigation of the BaO-Al<sub>2</sub>O<sub>3</sub> system was conducted by Wallmark and Westgreen (15). They determined the compounds BA and BA<sub>6</sub> were both hexagonal with the latter being isostructural with  $\beta$ -alumina. X-ray analyses of the compounds more basic than BA were unsuccessful due to excessive reaction of the materials to atmospheric moisture. Carlson, et al (16)., made a study

of the  $\text{BaO-Al}_2\text{O}_3\text{-H}_2\text{O}$  system at  $30^\circ\text{C}$  and found that the various barium aluminates formed an entirely different series of hydrates than their analog calcium aluminates. They also discovered that the barium aluminates exhibited a greater solubility in water than the corresponding calcium aluminates.

In 1952, Toropov and Galakhov (17) determined that  $\text{BA}$ ,  $\text{B}_3\text{A}$  and  $\text{BA}_6$  all melt congruently and assigned the melting points as  $1830^\circ\text{C}$ ,  $1750^\circ\text{C}$  and  $1900^\circ\text{C}$  respectively. They also established liquidus curves for the system and reported the existence of four eutectics. The phase diagram constructed from their work is shown in Figure 2.4. Purt (18) also investigated the  $\text{BaO-Al}_2\text{O}_3$  system and reported the melting points of  $\text{BA}$ ,  $\text{B}_3\text{A}$  and  $\text{BA}_6$  as  $1815^\circ\text{C}$ ,  $1620^\circ\text{C}$  and  $1915^\circ\text{C}$  respectively. A comparison of the data published by Purt and the Russian investigators is given in Table 2.1. The phase diagram given by Purt is shown in Figure 2.5. His samples were prepared by decomposition of barium carbonate in mechanical mixtures of alumina. Slumping of the pellets during heating were taken as liquidus temperatures; however, there is no mention of how solidus temperatures were determined. Purt reported the

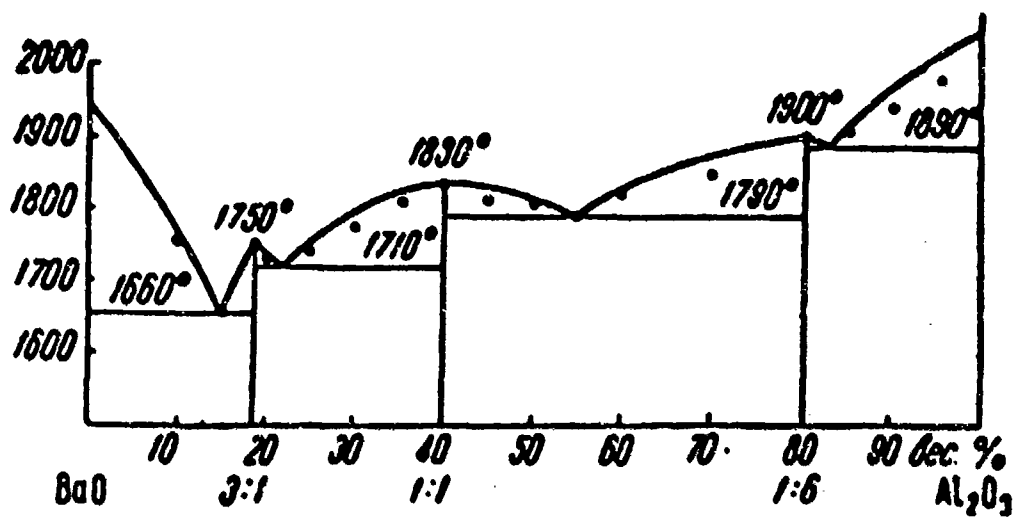


Figure 2.4. Phase Diagram of the BaO-Al<sub>2</sub>O<sub>3</sub> System by Toropov and Galachov (17).

Table 2.1. Compounds and Eutectic Compositions As Found by Purt (18) and the Toropov and Galachov (17).

Compositions	Toropov and Galachov		Purt	
	% Wt. BaO	Melting Point (°C)	% Wt. BaO	Melting Point (°C)
Compounds				
BA <sub>6</sub>	20.1	1900	20.1	1915
BA	60.2	1830	60.2	1815
B <sub>3</sub> A	81.8	1750	81.8	1620
Eutectics				
A-BA <sub>6</sub>	17	1890	16	1875
BA <sub>6</sub> -BA	45	1790	38	1620
BA-B <sub>3</sub> A	77.5	1710	76.5	1480
B <sub>3</sub> A-B	85	1660	87	1425

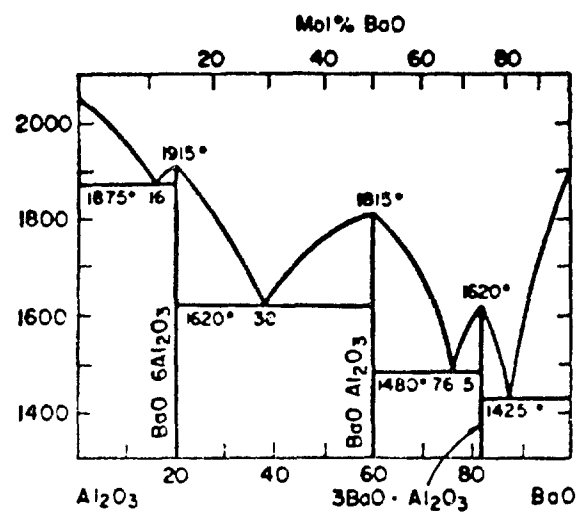


Figure 2.5. Phase Diagram of the BaO-Al<sub>2</sub>O<sub>3</sub> System by Purt (18).

compound  $B_3A$  to have a body centered cubic unit cell with the lattice parameter,  $a_0=14.151 \text{ \AA}$ .

Both Puri and Toropov and Galakhov reported that no compound more basic than  $B_3A$  existed in the  $BaO-Al_2O_3$  system. It was not until 1971 that any new barium aluminate compounds were discovered. In an investigation by Appendino (19), five compounds more basic than  $B_3A$  were identified by x-ray diffraction analysis. The compounds identified were  $B_4A$ , stable above 940 C;  $B_5A$ , stable under 940 C;  $B_7A$ , stable under 1050 C;  $B_8A$ , stable under 1050 C; and  $B_{10}A$ , stable under 1130 C. The subsolidus portion of the system is shown in Figure 2.6, and the original unindexed x-ray diffraction patterns are listed in Table 2.2. Lambert (1) determined solidus and liquidus temperatures in the high-baria portion of the  $BaO-Al_2O_3$  system using a tungsten strip microfurnace. The compounds BA and  $B_3A$  were reported as congruently melting, with melting points of 2170°C and 1580°C respectively. The melting point for BA is over three hundred degrees higher than those reported by Toropov and Galackov and by Puri. The compound  $B_4A$  was reported to melt incongruently to

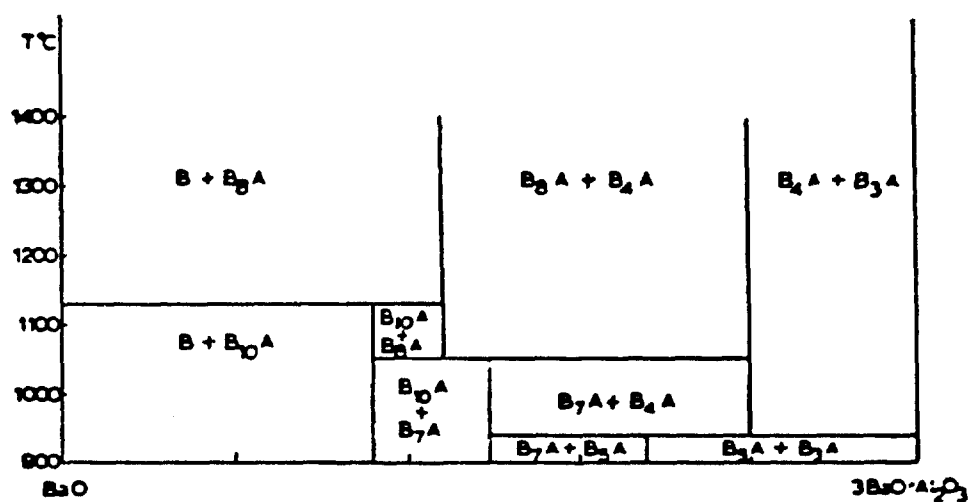


Figure 2.6. Sub-solidus BaO-Al<sub>3</sub>O<sub>3</sub> Phase Diagram by Appendino (19).



Table 2.2. XRD Patterns for B<sub>4</sub>A, B<sub>5</sub>A, B<sub>7</sub>A, B<sub>8</sub>A and B<sub>10</sub>A by Appendino (19).

4BaO·Al <sub>2</sub> O <sub>3</sub>				8BaO·Al <sub>2</sub> O <sub>3</sub>				5BaO·Al <sub>2</sub> O <sub>3</sub>			
d	i	d	i	d	i	d	i	d	i	d	i
5.342	6	2.259	25	5.075	4	1.904	5	5.007	10	2.088	15
5.193	11	2.208	3	4.263	5	1.884	3	4.152	50	2.083	20
4.498	10	2.159	4	3.914	4	1.850	6	3.847	8	2.002	10
4.048	15	2.104	4	3.536	40	1.807	5	3.501	30	1.935	10
3.550	3	2.026	30	3.509	8	1.777	5	3.391	40	1.915	3
3.493	3	1.972	3	3.383	15	1.738	8	3.373	35	1.785	8
3.458	7	1.922	3	3.336	10	1.718	2	3.144	15	1.757	10
3.391	2	1.873	4	3.264	20	1.698	20	2.995	100	1.751	8
3.321	8	1.847	10	3.195	6	1.664	5	2.900	80	1.697	10
3.243	5	1.832	5	3.138	50	1.641	10	2.754	5	1.668	10
3.227	3	1.812	2	3.108	100	1.570	6	2.712	7	1.522	3
3.121	3	1.800	5	2.992	20	1.319	4	2.666	10	1.501	2
3.015	100	1.783	18	2.964	50	1.289	3	2.487	10	1.452	15
2.913	35	1.761	15	2.889	15	1.252	2	2.463	12	1.435	5
2.818	40	1.741	4	2.615	30	1.207	3	2.424	15	1.373	3
2.685	2	1.701	25	2.580	25	1.154	2	2.284	30	1.349	3
2.647	7	1.662	20	2.561	7			2.236	10	1.336	5
2.584	2	1.636	2	2.479	5			2.188	10	1.302	7
2.564	3	1.508	12	2.450	4						
2.543	4	1.454	4	2.363	4						
2.490	5	1.410	10	2.240	5						
2.447	10			2.218	10						
2.416	4			2.155	30						
2.391	15			2.079	3						
2.327	5			1.962	15						
				1.946	10						

X-ray Diffraction Patterns for  $B_4A$ ,  $B_5A$ ,  $B_7A$ ,  $B_8A$ , and  $B_{10}A$   
by Appendino (concluded).

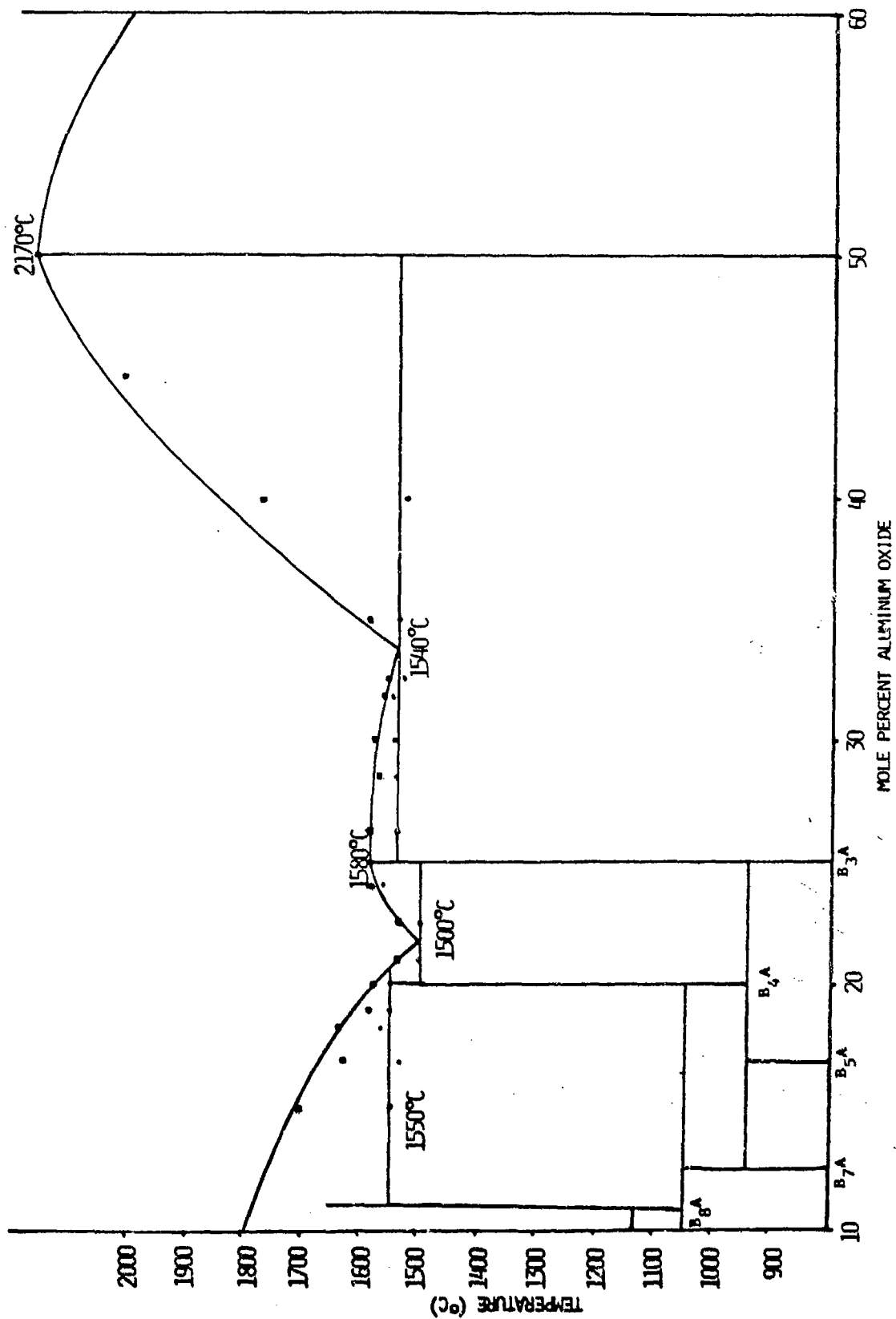
$10BaO \cdot Al_2O_3$				$7BaO \cdot Al_2O_3$			
d	I	d	I	d	I	d	I
5.618	10	1.634	10	5.012	10	2.045	5
5.157	26	1.603	10	4.211	40	1.953	10
3.808	30	1.412	3	3.409	50	1.905	8
3.162	100	1.393	3	3.213	15	1.888	10
3.064	80	1.389	5	3.157	4	1.846	8
2.811	15	1.347	3	3.066	100	1.805	10
2.583	100	1.291	2	2.904	80	1.748	2
2.466	50	1.254	10	2.889	60	1.721	15
2.310	80	1.219	5	2.535	10	1.699	4
1.994	8	1.193	3	2.497	15	1.671	5
1.904	10			2.399	10	1.618	5
1.857	8			2.383	20	1.580	3
1.787	10			2.298	3	1.479	2
1.751	30			2.164	10		
1.740	5			2.106	25		
1.722	10						
1.673	8						
1.647	15						

liquid and a more basic compound (most probably  $B_8A$ ,  $B_{10}A$  or  $BaO$ .) Two eutectic compositions were reported at 34 mole percent  $Al_2O_3$  and 23 mole percent  $Al_2O_3$ , with temperatures of  $1540^{\circ}C$  and  $1500^{\circ}C$  respectively. Figure 2.7 shows the phase diagram constructed from her data and a comparison of this diagram with those of previous investigators is shown in Figure 2.8.

D. CaO- $Al_2O_3$  SYSTEM

As a result of interest of the Portland cement industry, the  $CaO-Al_2O_3$  system has received a great deal of attention in the areas of phase equilibria and cement chemistry. Extensive literature surveys are available for the interested reader (20); however, a brief review of only that portion the system pertinent to this study will be given here.

Lea and Desch (21) published a phase diagram of the  $CaO-Al_2O_3$  system containing six intermediate binary compounds with formulae;  $C_3A$ ,  $C_{12}A_7$ ,  $CA$ ,  $C_3A_5$ ,  $CA_2$  and  $CA_6$ . Of these only the compound  $C_3A_5$  was not assigned a primary phase field. The diagram, constructed from data obtained under conditions of normal humidity, is shown in Figure



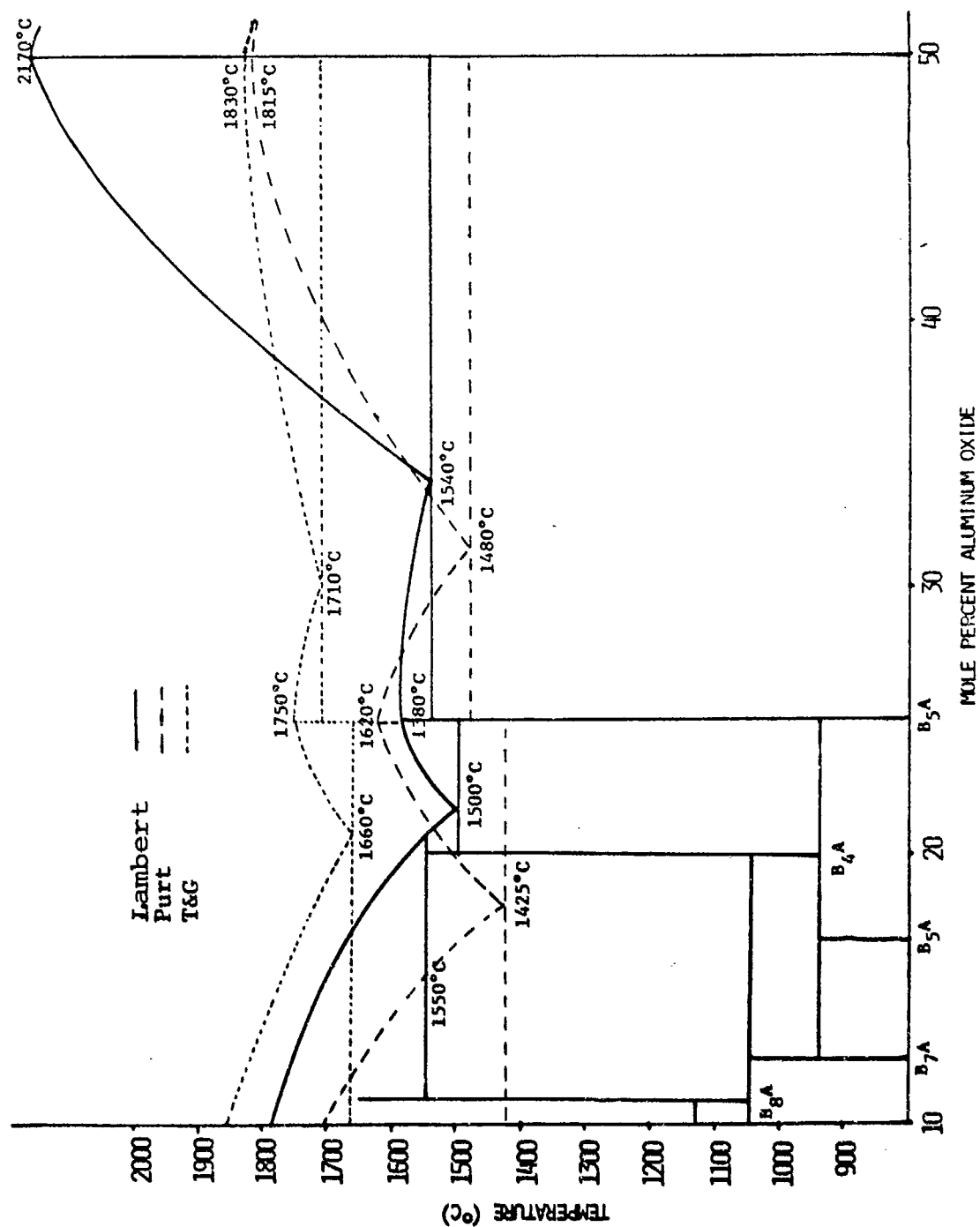


Figure 2.8. Comparison of Previous BaO-Al<sub>2</sub>O<sub>3</sub> Phase Diagrams.

2.9. Nurse, et al. (22) made a study of the calcium aluminate system under anhydrous conditions and published the diagram shown in Figure 2.10. This diagram does not feature a primary phase field for the compound  $C_{12}A_7$ , and it was determined that  $C_{12}A_7$  was actually a hydrated calcium aluminate that exhibited reversible equilibrium with  $H_2O$  in the temperature range  $950-1350^{\circ}C$ . They also present the results of thermochemical calculations demonstrating that a mechanical mixture of CA and  $C_3A$  corresponding to the same composition as  $C_{12}A_7$  was more stable at  $1361^{\circ}C$  than  $C_{12}A_7$ . Nurse, et al. presented  $C_3A$ , CA and  $CA_2$  as incongruently melting compounds. It is interesting to note that the corresponding barium compounds  $B_3A$ , BA and  $BA_6$  have all been reported to melt congruently. A great deal of controversy has surrounded the compound  $CA_6$  in terms of its exact stoichiometry and an excellent review of the pertinent literature is given by Day (20). Unlike the  $BaO-Al_2O_3$  system, no compound more basic than  $C_3A$  has been reported in the calcium aluminate system.

#### E. BaO-CaO SYSTEM

In Appendino's (23) investigation of the BaO-CaO-

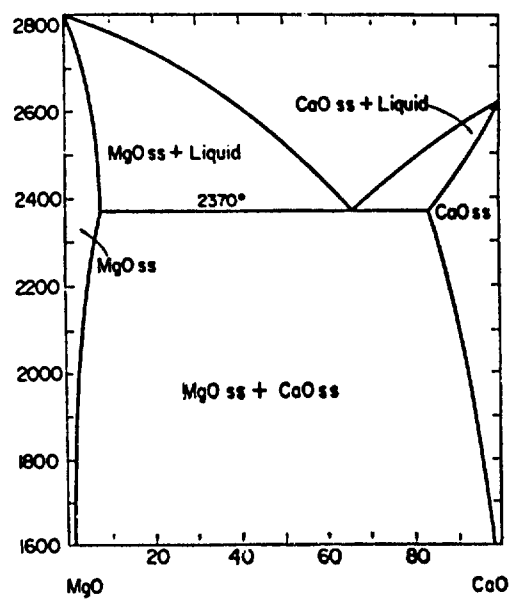


Figure 2.9. CaO-Al<sub>2</sub>O<sub>3</sub> System, at Normal Humidity, by Lea and Desch (21).

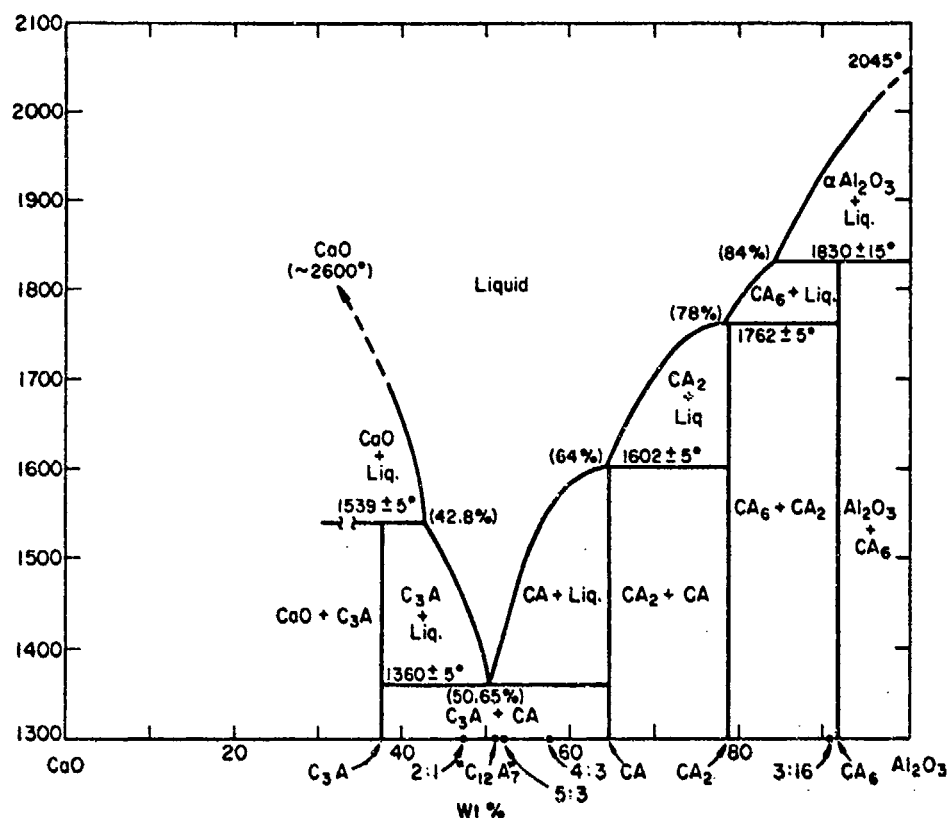


Figure 2.10. CaO-Al<sub>2</sub>O<sub>3</sub> System, under anhydrous conditions, by Nurse, et al. (22).



$\text{Al}_2\text{O}_3$  system it was determined that the solubility of  $\text{CaO}$  in  $\text{BaO}$  was virtually zero (although it is generally accepted that at least an infinitesimal amount of solid solubility must exist in all systems.) The system is most probably a simple eutectic with no detectable solid solution regions. No other specific information is available on the  $\text{BaO-CaO}$  system and all ternary phase diagrams featuring the  $\text{BaO-CaO}$  binary show this as an uninvestigated region.

F.  $\text{BaO-CaO-Al}_2\text{O}_3$  SYSTEM

In 1954 Lapin (24) published the first mention of the  $\text{BaO-CaO-Al}_2\text{O}_3$  system in a paper where he reported isolating the ternary compound  $\text{BCA}_2$  in a metallurgical slag. In a later investigation, Brisi and Montorsi (25) were unable to synthesize  $\text{BCA}_2$  and concluded that the composition was actually a mechanical mixture of BA and CA. They also constructed a partial isothermal section at  $1250^\circ\text{C}$  (Figure 2.11) which contained the compound  $\text{BC}_2\text{A}_4$ . The solubility of  $\text{CaO}$  in the compound  $\text{B}_3\text{A}$  was determined to be 24 mole percent and the unit cell was reported to be cubic with lattice parameter,  $a_0=16.51 \text{ \AA}$ . It was also

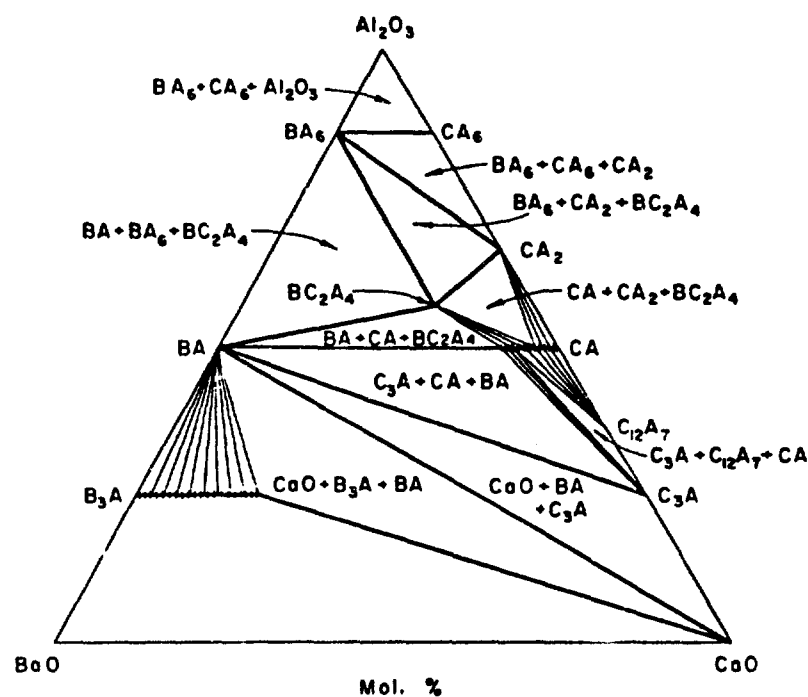


Figure 2.11. Partial Isothermal section at 1250°C of the BaO-CaO-Al<sub>2</sub>O<sub>3</sub> System by Brisi and Montorsi (25).

noted that no true binary join exists between  $B_3A$  and  $C_3A$  as a result of a miscibility gap located between the two compounds.

Massazza (26) presented a partial isothermal section of the barium calcium aluminate system at  $1400^{\circ}\text{C}$  (Figure 2.12.) He determined that the ternary compound  $BC_2A_4$  exhibited a range of compositions as a result of the solubility of  $\text{CaO}$  in the crystal structure. Partial solid solubility was also detected along the join connecting  $BA_6$  and  $CA_6$ . Massazza determined the compatibility relationships in the partial phase diagram entirely by optical microscopy.

In 1972, Appendino (23) reported the results of an investigation on the more basic portion of the  $\text{BaO-CaO-Al}_2\text{O}_3$  system. The study involved the construction of a partial isothermal section at  $1250^{\circ}\text{C}$  (Figure 2.13.) He reported finding a ternary compound having the formula  $B_3CA$ . It was found that  $B_4A$  formed a solid solution series with  $\text{CaO}$  with a solubility limit of 10 mole percent  $\text{CaO}$ . Solid solubility of  $\text{CaO}$  in the structure of  $B_5A$  was determined to be only 2.5 mole percent and the compound

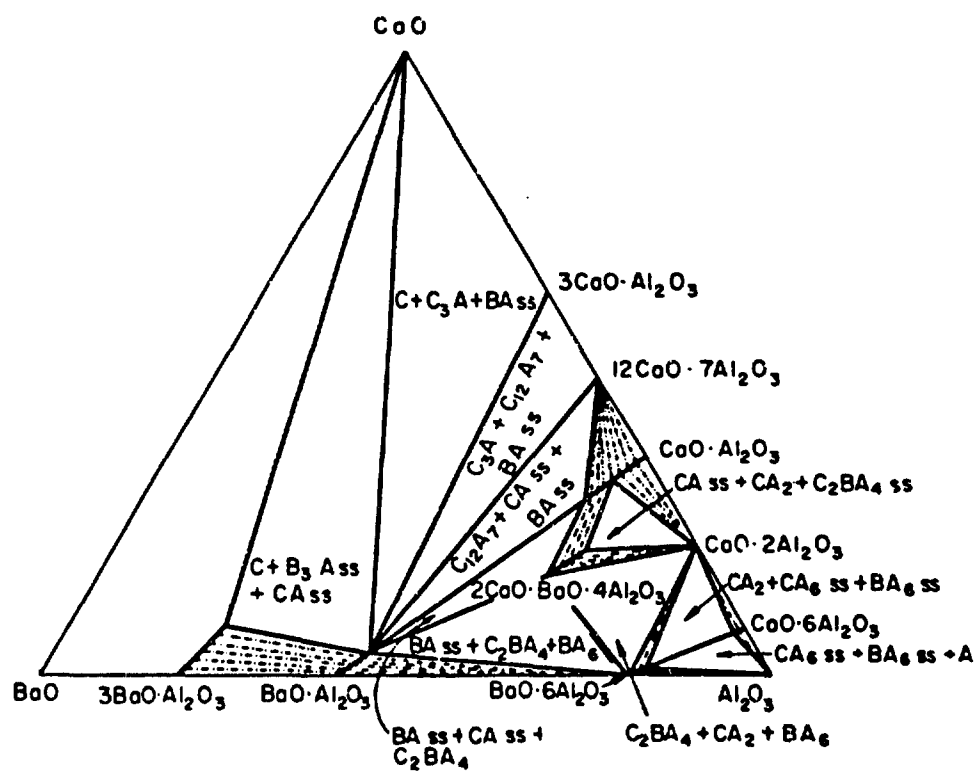


Figure 2.12. Partial Isothermal Section at 1400°C of the BaO-CaO-Al<sub>2</sub>O<sub>3</sub> System by Massazza (26).

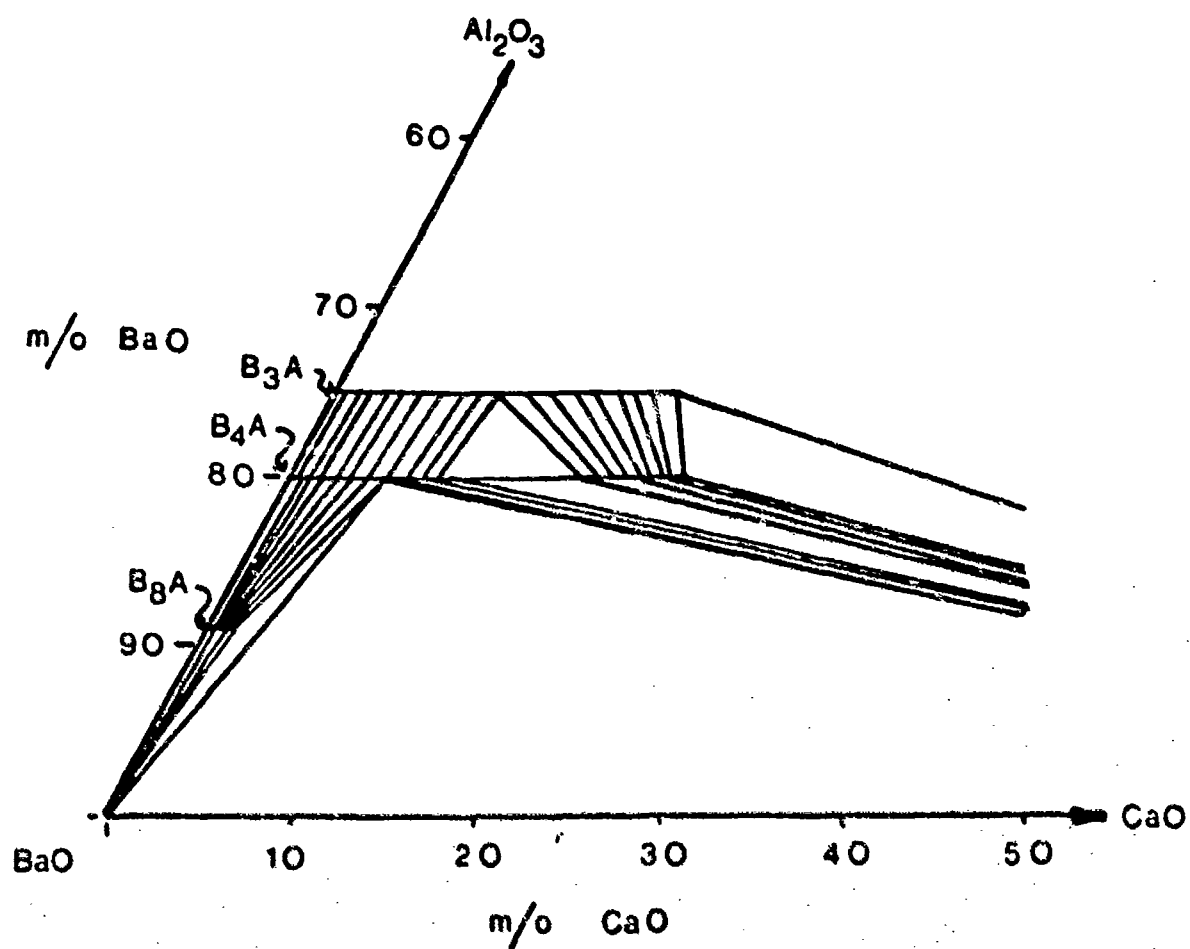


Figure 2.13. Partial Isothermal Section at 1250°C of the BaO-CaO-Al<sub>2</sub>O<sub>3</sub> System by Appendino (23).

$B_3CA$  was said to exist over a range of compositions as a result  $Ba^{2+}$  replacement by  $Ca^{2+}$ . Wolten (27) suggested that the composition  $B_3CA$  may actually be a part of the  $B_{4-x}C_xA$  solid solution series, where exactly one-quarter of the barium atoms have been substituted for calcium atoms. His suggestion was based on the location of the composition on the ternary diagram and the similarity in the x-ray diffraction patterns of  $B_3CA$  and  $B_{4-x}C_xA$  solid solutions. Wolten also constructed a composite phase diagram from data given by Brisi and Montorsi, Massazza, and Appendino. This phase diagram is shown in Figure 2.14.

Solidus and liquidus temperatures for the compositions  $B_5C_3A_2$ ,  $B_3CA$  and  $B_4CA$  were determined by Asselanis (11) using heating curves. Samples for his melting point analyses were obtained by dry-mixing the oxides, which were then fused with an oxygen-acetylene flame. Solidus and liquidus determinations were accomplished in argon at 0.5 atm. pressure, using a controlled-atmosphere microfurnace and a Type C thermocouple. The solidus and liquidus temperatures obtained by Asselanis are given in Table 2.3. Asselanis also attempted to determine the melting point of  $BaO$  since

# LEGEND

- |                        |                           |
|------------------------|---------------------------|
| 1. $B_{2.25}C_{0.75}A$ | 7. $B_{7.8}C_{0.2}A$      |
| 2. $B_{2.9}C_{1.1}A$   | 8. $B_3CA$                |
| 3. $B_{3.75}C_{0.25}A$ | 9. $BC_2A_4$              |
| 4. $B_{3.7}C_{0.3}A$   | 10. $B_{0.12}C_{0.88}A$   |
| 4a. $B_{3.6}C_{0.4}A$  | 11. $B_{0.064}C_{0.936}A$ |
| 5. $B_{3.2}C_{0.8}A$   | 12. $B_{0.15}C_{0.85}A$   |
| 6. $B_{2.6}C_{0.4}A$   |                           |

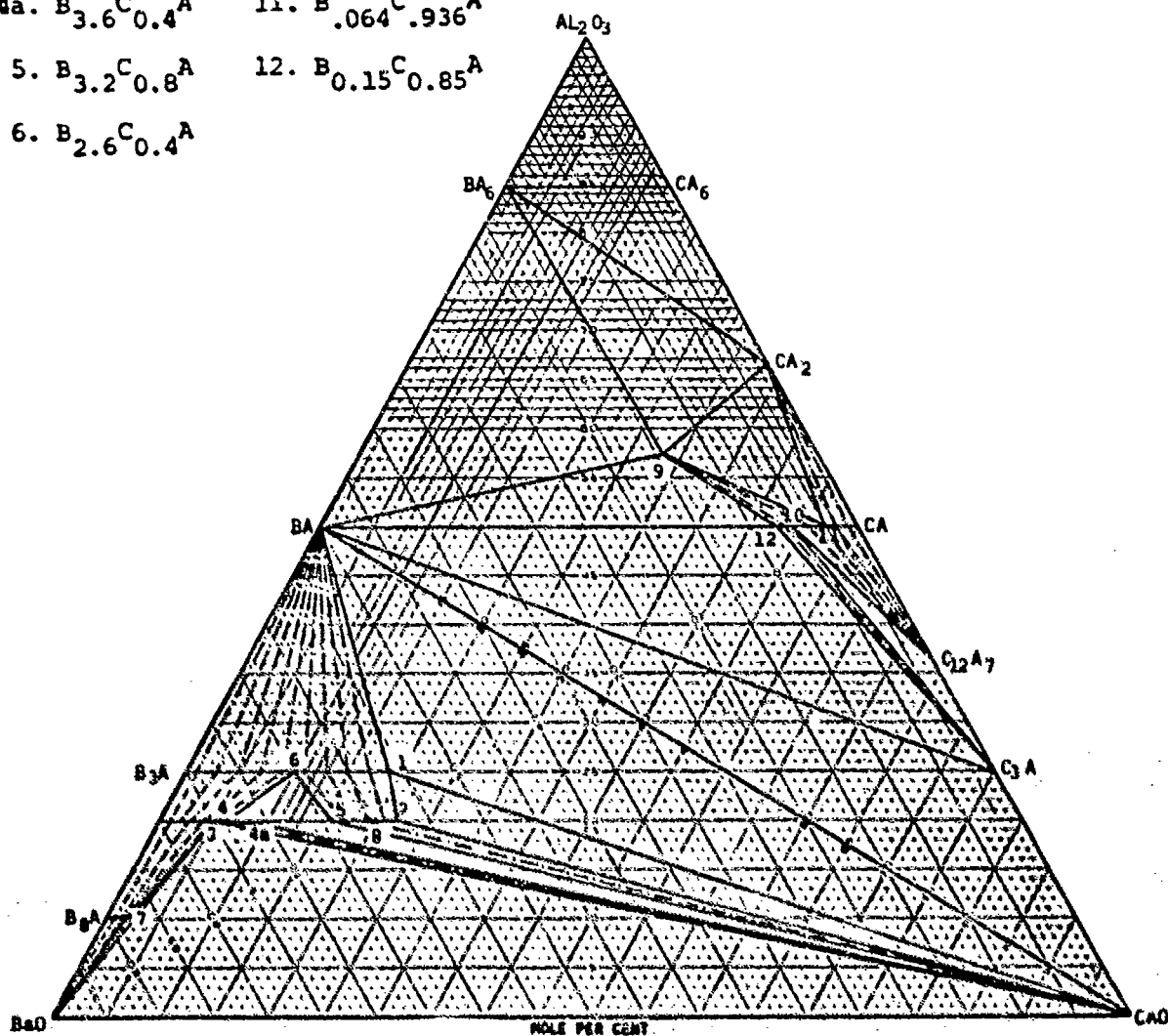


Figure 2.14. Composite BaO-CaO-Al<sub>2</sub>O<sub>3</sub> Diagram Constructed by Wolten (27).

Table 2.3. Solidus and Liquidus Temperatures of BCA Compositions by Asselanis (11).

<u>Compositions</u>	<u>Solidus (°C)</u>	<u>Liquidus (°C)</u>
3BaO·CaO·Al <sub>2</sub> O <sub>3</sub>	1684 ±28	1768 ±17
4BaO·CaO·Al <sub>2</sub> O <sub>3</sub>	1786 ±15	1879 ±15
5BaO·3CaO·2Al <sub>2</sub> O <sub>3</sub>	1762 ±40	1899 ±24



only one literature value was available. The value he obtained by melting BaO (technical powder, Fisher Scientific) was  $2074 \pm 15^{\circ}\text{C}$ . This is somewhat higher than Schumacher's value of  $1925^{\circ}\text{C}$ . However, Schumacher's determination was performed in hydrogen at a pressure of 0.2 atmospheres. The BaO heating curve given by Asselanis is shown in Figure 2.15.

In 1982, Tarter (12) determined the solidus and liquidus temperatures of seven barium calcium aluminate compositions (Table 2.4). He used a modified design of the microfurnace built by Asselanis, and melted the compositions in hydrogen at one atmosphere. The samples were prepared by dry mixing  $\text{BaCO}_3$ ,  $\text{CaCO}_3$  and gamma alumina in the proper proportions and then calcining the mixtures at 1180 C for 53 hours.

#### G. EXPERIMENTAL DIFFICULTIES ASSOCIATED WITH BaO

The major experimental difficulties encountered in working with BaO are: high reactivity with containment vessels at elevated temperatures; reactivity with atmospheric moisture and carbon dioxide; the presence of a low-temperature eutectic in the BaO- $\text{BaCO}_3$  system; and the

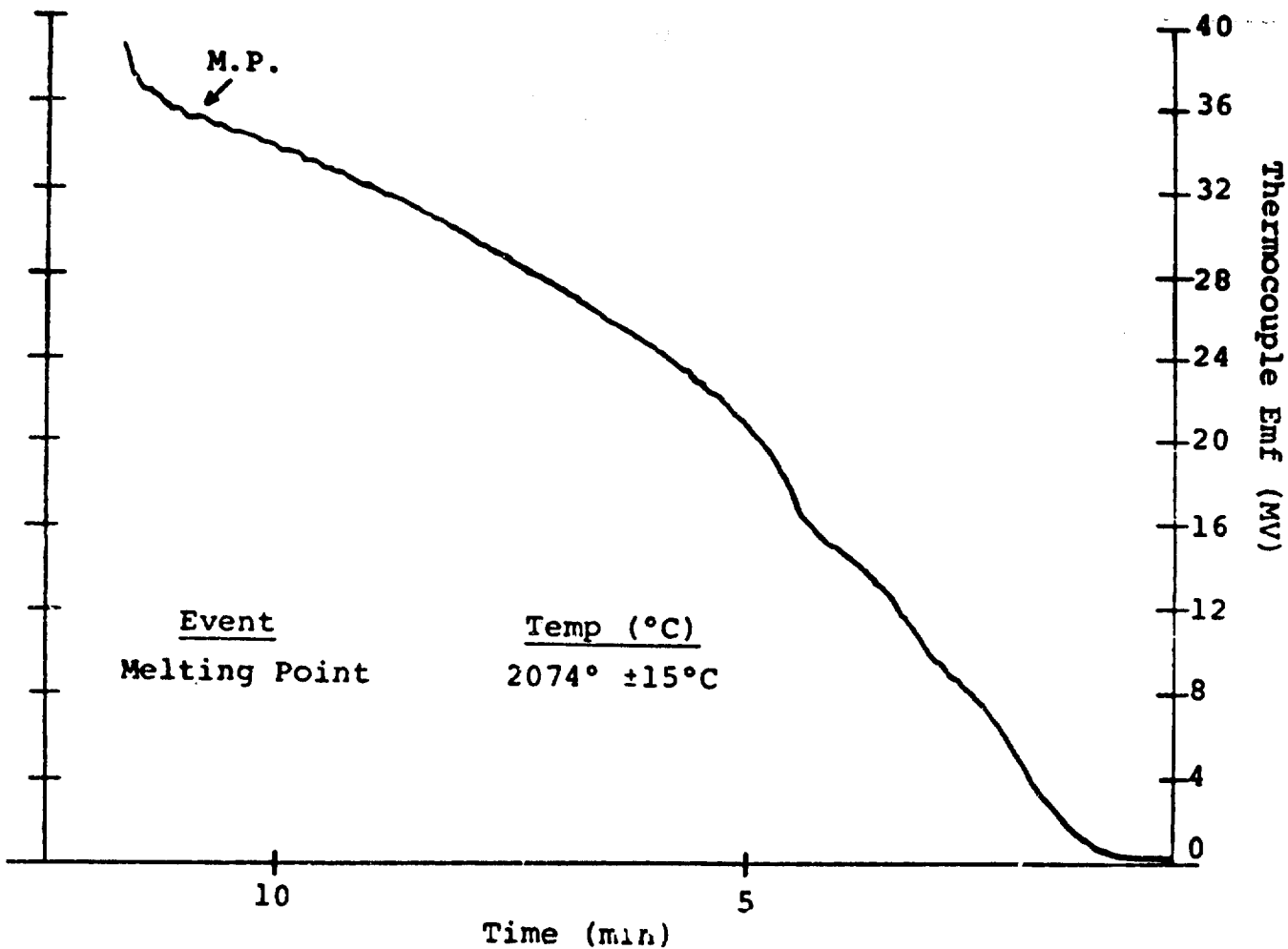


Figure 2.15. Heating Curve of BaO by Asselanis (11).

Table 2.4. Solidus and Liquidus Temperatures of BCA Compositions by Tarter (12).

Composition	Solidus (°C)	Liquidus (°C)
$B_5C_3A_2$	1585	1760
$B_4CA$	1490	1835
$B_6CA_2$	1550	1690
$B_3CA$	not observed	1775
$B_{11}C_6A_4$	1550	1795
$B_2CA$	1585	1835
BCA	1505	1775

high vapor pressure of BaO above the solid at elevated temperatures.

In a study of the BaO-B<sub>2</sub>O<sub>3</sub> system, Levin and McMurdie (28) observed the reaction of free BaO with platinum containers. Baker (29) suggested that, in high-BaO melts, platinum dissolves as an oxide. However, he also stated that the actual mechanism of the BaO-Pt reaction was unclear. In 1969, Schneider and McDaniel (30) reported the results of an investigation on the BaO-Pt system in air. They presented a BaO-PtO<sub>2</sub> pseudo-binary diagram containing the compound 4BaO-PtO<sub>2</sub> which was stable above 1050°C. They determined that for oxidation of platinum to occur in air the system must contain a material such as BaO.

The hydration of high-baria compositions poses a severe problem in x-ray diffraction studies. In an investigation of the BaO-NiO system, Lander (31) described the practice of mixing a small amount of dried pump oil with the sample to provide protection from atmospheric moisture. Using this method he was able to obtain powder diffraction patterns of excellent quality. Lambert (1) performed x-ray diffraction analyses on compositions in the

BaO-Al<sub>2</sub>O<sub>3</sub> system using a dynamic atmosphere of dry nitrogen. The nitrogen was contained by using a controlled-atmosphere radiation shield.

BaCO<sub>3</sub> is a common contaminant in high-baria compositions as a result of the reaction of free BaO with atmospheric CO<sub>2</sub>. A low-melting eutectic in the BaO-BaCO<sub>3</sub> system increases the difficulty in preparing and handling baria-rich compositions. Schumacher (7) mentioned the presence of a low-melting eutectic between BaO and BaCO<sub>3</sub> in his investigation of the melting point of BaO. Lander studied the BaO-BaCO<sub>3</sub> system and determined the eutectic temperature to be 1060 C and the eutectic composition to be 2BaCO<sub>3</sub>.BaO. Baker (29) reported the eutectic composition as 64% BaCO<sub>3</sub>-36% BaO and a eutectic temperature of 1060°C. He determined these values by thermogravimetric analysis and presented temperature vs. weight loss curves which featured a plateau region occurring at the temperature where the first liquid forms in the system. The phase diagram for the system is given in Figure 2.16.

Barium oxide and high-baria compositions typically exhibit high BaO vapor pressures above the solid at temperatures above 1400°C. Experimental difficulties are

**BaO-CO<sub>2</sub>**

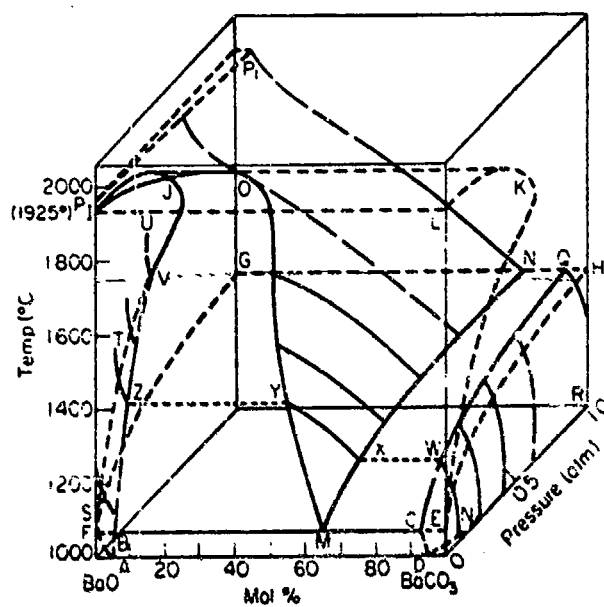


**Figure 2.16. BaO-BaCO<sub>3</sub> System by Baker (29).**

encountered at elevated temperatures when compositional changes occur as a result of the loss of BaO by evaporation. Several mass spectrometric studies conducted in the early 1950's have identified BaO as the principal evaporating species over solid barium oxide. Other gaseous species such as  $\text{Ba}_2\text{O}^+$  and  $\text{Ba}_2\text{O}_2^+$  were also detected but only in minor quantities. Inghram, et al. (32) observed the above mentioned vapor species, along with  $\text{Ba}_2\text{O}_3$ , using a mass spectrometer in association with a Knudsen cell. Using a thermodynamic treatment of the experimental ion currents, the  $\Delta H_{273}$  for the reaction,

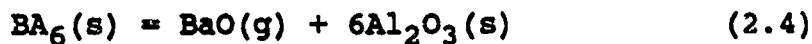
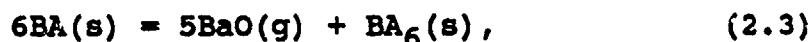


was determined to be 104 kcal/mole.

Hilpert and Gerads (33) also studied the vaporization of BaO by mass spectroscopy and found the relation of BaO vapor pressure as a function of temperature for equation 2.1 in the temperature range 1332° to 1681° Kelvin to be,

$$\log p(\text{atm}) = -(2.173)(10^4/T) + 7.19 \quad (2.2)$$

Hilpert, et al. (34) determined that the compounds BA, BA<sub>6</sub> and B<sub>3</sub>A evaporate incongruently by the reactions,



and



The equilibrium vapor pressures of BaO over the solid compounds were given by the relations;

$$\log p(\text{atm}) = -(2.814)(10^4/T) + 6.50 \quad (1840 \text{ to } 2086 \text{ K}), \quad (2.6)$$

$$\log p(\text{atm}) = -(2.830)(10^4/T) + 9.14 \quad (1897 \text{ to } 2170 \text{ K}), \quad (2.7)$$

and

$$\log p(\text{atm}) = -(2.362)(10^4/T) + 7.90 \quad (1469 \text{ to } 1745 \text{ K}) \quad (2.8)$$

respectively.

Lipeles and Kan (35) calculated the equilibrium vapor pressure of BaO over the compounds B<sub>4</sub>A and B<sub>8</sub>A and also for several CaO solid solutions in the BaO-CaO-Al<sub>2</sub>O<sub>3</sub>



system. The compositional dependence of vapor pressure is such that the equilibrium vapor pressure increases as the molar content of BaO within the system increases. Substitution of  $\text{Ca}^{2+}$  for  $\text{Ba}^{2+}$  in the crystal structures of the barium aluminates results in a decrease of the equilibrium BaO vapor pressure due to the increase in configurational entropy.

#### H. CRYSTALLOGRAPHY OF BARIUM ALUMINATES

This section contains a review of the literature pertaining to the crystallography of compounds and solid solutions in the  $\text{BaO-Al}_2\text{O}_3$  and  $\text{BaO-CaO-Al}_2\text{O}_3$  systems. Few crystallographic investigations have been conducted on the portions of the systems containing greater than 50 mole percent BaO due to the excessive reactivity of these compositions with atmospheric moisture. However, the less basic compounds are easier to work with, and these regions have been studied extensively. In 1937, Wallmark and Westgren (15) used Hull-Debye-Scherer x-ray powder photographs to determine the unit cells of BA and  $\text{BA}_6$ . The quadratic forms of the compounds were determined using Hull-Davey curves. The unit cells of both compounds were

found to have hexagonal symmetry. The powder pattern for BA was found to index most satisfactorially in the space group  $C6_32$ . The lattice dimensions were determined to be  $a_0=5.209 \text{ \AA}$  and  $c_0=8.761 \text{ \AA}$ . The aluminum ions in this structure were found to have tetrahedral coordination with oxygen. The compound  $BA_6$  was determined to be isostructural with  $\beta$ -alumina, with the lattice dimensions  $a_0=5.577 \text{ \AA}$  and  $c_0=22.67 \text{ \AA}$ . They stated that analog structures of the aluminates also existed in the systems  $SrO-Al_2O_3$ ,  $SrO-Fe_2O_3$ ,  $BaO-Fe_2O_3$  and  $PbO-Fe_2O_3$ .

Purt (18) reported the compound  $B_3A$  as having a body-centered unit cell, with the cell edge  $a_0=14.151 \text{ \AA}$ . Later, Brisi and Montorsi (25) published a 21-line diffraction pattern for  $B_3A$  indexed on the basis of a primitive cubic lattice. The lattice parameter for this cell was  $a_0=16.51 \text{ \AA}$ . Wolten (27) suggested that the compounds  $B_3A$  and  $C_3A$  are isostructural, along with any substitutional solid solutions formed between the two (assuming the absence of any unique intermediate phase.) According to Mondal and Jeffery (36), this structure has a cubic unit cell possessing symmetry consistent with the

space group Pa3. The unit cell can be reduced to an assemblage of 64 cubic substructural units having cell edges of  $a_0/4$ . The complete unit cell contains 72 divalent ion sites, 48 aluminum, and 144 oxygen sites. The divalent ions are distributed on six non-equivalent sites plus their symmetry-related positions. Eight of the 64 subcells contain six-fold rings composed of two types of spatially non-equivalent  $AlO_5$  tetrahedra. The  $[Al_6O_{18}]^{18-}$  rings are centered on the three-fold axes of the cubic cell, and are located near the corners of the unit cell at the coordinates  $(1/8, 1/8, 1/8)$ . The aluminum ions are located nearly at the corners of the subcells. Eight subcells are occupied by the six-membered rings. The 56 remaining subcells are occupied by divalent ions at body-centering positions. The additional divalent ions are located on the three-fold axes, very near the corners of their associated subcells. Wolten provided unit cells for the compounds  $B_4A$ ,  $B_5A$ ,  $B_7A$ ,  $B_8A$ ,  $B_{10}A$  and  $B_3CA$ . Each compound indexed satisfactorily to an orthorhombic unit cell and all with the exception of  $B_{10}A$  gave similar lattice parameters. Wolten stated that the unit cells obtained from his indexings were only tentative, and that the true symmetry

of the the cells may be lower than orthorhombic.

## CHAPTER III

### PROCEDURE

In this study, various barium calcium aluminate compositions were prepared by solid state reaction of raw materials. The chemical phase equilibrium relationships were determined by solidus and liquidus temperature measurements and phase analyses of isothermally heat treated compositions. The crystallography of several phases was studied, along with their thermal behavior in the temperature range 25 to 1500°C. This section describes the procedure and techniques used in the investigation.

#### A. SAMPLE PREPARATION

Fourty powder samples, weighing approximatly 300 gms. each (Table 3.1) were prepared at Semicon Associates by wet-mixing the proper proportions of  $\text{BaCO}_3$  (J.T. Baker),  $\text{CaCO}_3$  (J.T. Baker) and alpha alumina (Reynolds) in a two-liter polyethelene jar containing 300 cc. of water and 50 percent alumina grinding media. After one-half hour of mixing, the powders were transferred to a porcelain evaporating dish and dried at 200°C for 12 hours. The powders were then lightly ground in the dish with a pestle

Table 3.1. Compositions Used for Solidus and Liquidus Determinations.

Composition No.	mole percent		
	BaO	CaO	Al <sub>2</sub> O <sub>3</sub>
1	75.00	0.00	25.00
2	70.00	5.00	25.00
3	65.00	10.00	25.00
4	60.00	15.00	25.00
5	56.25	18.75	25.00
6	52.50	22.50	25.00
7	50.00	25.00	25.00
8	45.00	30.00	25.00
9	40.00	35.00	25.00
10	73.12	2.50	24.38
11	71.25	5.00	23.75
12	69.38	7.50	23.12
13	67.50	10.00	22.50
14	66.67	11.11	22.22
15	65.62	12.50	21.88
16	63.75	15.00	21.25
17	61.88	17.50	20.62
18	60.00	20.00	20.00
19	58.12	22.50	19.38
20	56.25	25.00	18.75
21	52.50	30.00	17.50
22	50.62	32.50	16.88
23	80.00	0.00	20.00
24	75.00	5.00	20.00
25	72.00	8.00	20.00
26	67.50	12.50	20.00
27	64.00	16.00	20.00
28	60.00	20.00	20.00
29	59.00	21.00	20.00
30	55.00	25.00	20.00
31	50.00	30.00	20.00
32	45.00	35.00	20.00
33	80.00	5.00	15.00
34	75.00	10.00	15.00
35	70.00	15.00	15.00
36	65.00	20.00	15.00
37	60.00	25.00	15.00
38	55.00	30.00	15.00
39	50.00	35.00	15.00
40	45.00	40.00	15.00

and placed in an alumina boat. The boat was loaded into an electric furnace where the powders were calcined in air at 1180°C for 53 hours. The powders were removed from the furnace at 200°C, then sealed in foil packages, and then sent to Ga. Tech for analysis. Here, the powder samples were removed from the foil packages as needed and quickly pressed into pellets 0.75 inch in diameter and 0.25 to 0.5 inch thick. The pellets were either used whole for isothermal heat treatments or broken into smaller pieces for solidus/liquidus determinations.

1. Isothermal Heat Treatments

The BCA compositions were heated for 30 minutes at 1475°C and one hour at 1100°C in the tungsten-strip microfurnace in dynamic hydrogen at one atmosphere. A number of samples were heated for 24 hours in a SiC electric furnace in static air. Five sample were subjected to heat treatments of 500 hours in a SiC electric tube furnace in air in order to verify that equilibrium had been established during the shorter heat treatments.

B. MICROFURNACE OPERATION

Fragments of a sample pellet were placed in the tungsten boat and the cover was positioned over the boat.

The boat and cover were mounted between the two electrodes and the thermocouple was lowered through the small opening in the top cover until the bead was in contact with the bottom of the boat. This contact was confirmed by observing slight flexure of the wires. The radiation shield was fastened into place, and the brass top plate was lifted into position on the cylindrical pyrex bell jar. The furnace chamber was evacuated to a pressure of less than 100 millitorr, then backfilled with hydrogen to a pressure of one atmosphere. This procedure was repeated once to insure a relatively pure hydrogen atmosphere.

All melting point determinations were made in flowing hydrogen at one atmosphere. The hydrogen was passed through a drying column before entering the furnace chamber. Bubble bottles filled with pump oil were used in the exit line to give a slight positive pressure in the furnace chamber. The initial heating cycle was used to establish the liquidus and to allow the sample to melt and completely surround the thermocouple bead. Heating rates of 10-15°C per minute were used to determine the temperature at which the last solid disappeared into the melt. This temperature was recorded as the liquidus.



Solidus temperatures were established using heating curves generated by heating the strip at rates in the range of 300-400 C per minute. Each sample was cycled to the liquidus not more than three times to avoid possible compositional changes due to evaporation of BaO.

C. EQUIPMENT

Asselanis (11) originally built the controlled atmosphere microfurnace used in this work; it was later modified by Tarter (12) and then again by Hill (37). The main features of the system are: a temperature capability of 2200°C, capability of operation in a reducing or inert atmosphere as well as under vacuum, a controlled rate of temperature change, and a nearly linear heating rate throughout the entire temperature range.

Figure 3.1 shows a schematic diagram of the entire furnace system. Figure 3.2 and 3.3 shows photographs of the actual system and the strip heater/thermocouple assembly. The furnace housing consisted of an aluminum base plate containing a 3.75 inch-diameter vacuum port connected to a pumping station. A pyrex cylinder, 12 inches high and 10 inches in diameter, was positioned over the

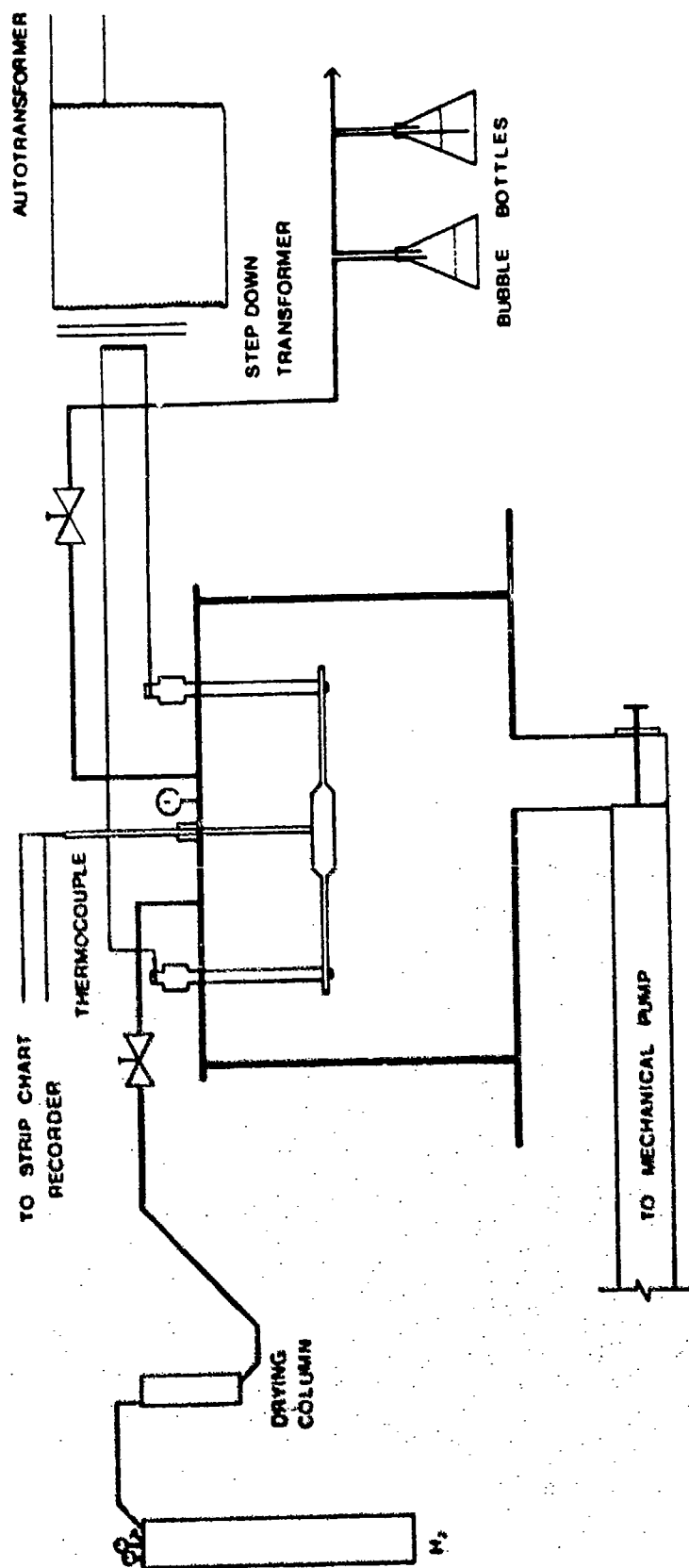


Figure 3.1. Schematic Diagram of Furnace System.

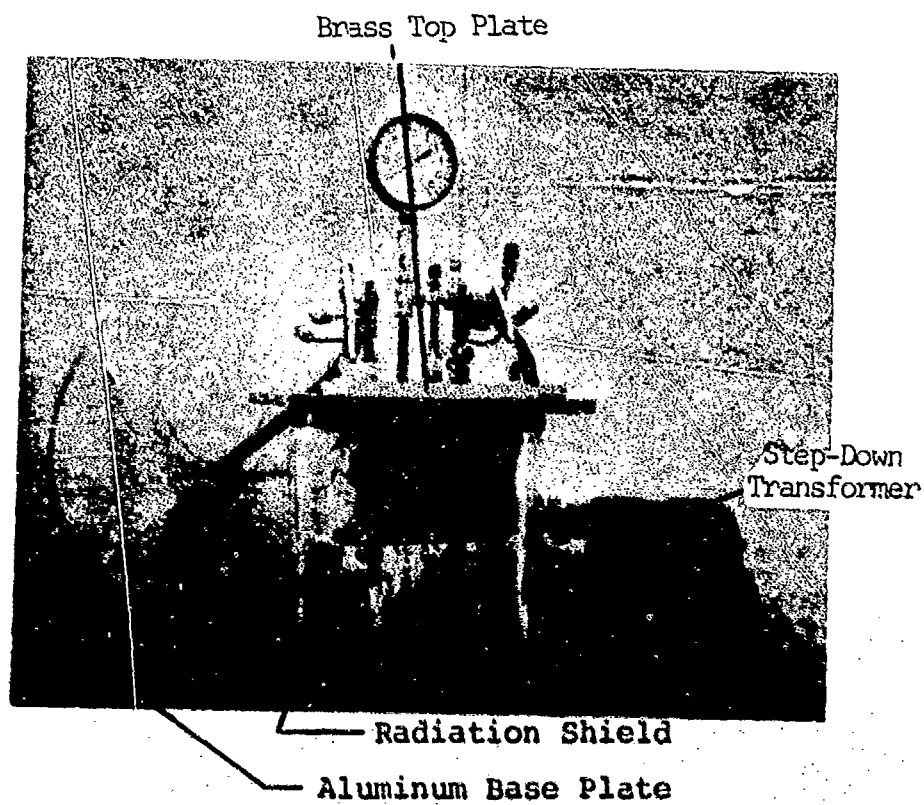


Figure 3.2. Photograph of Microfurnace

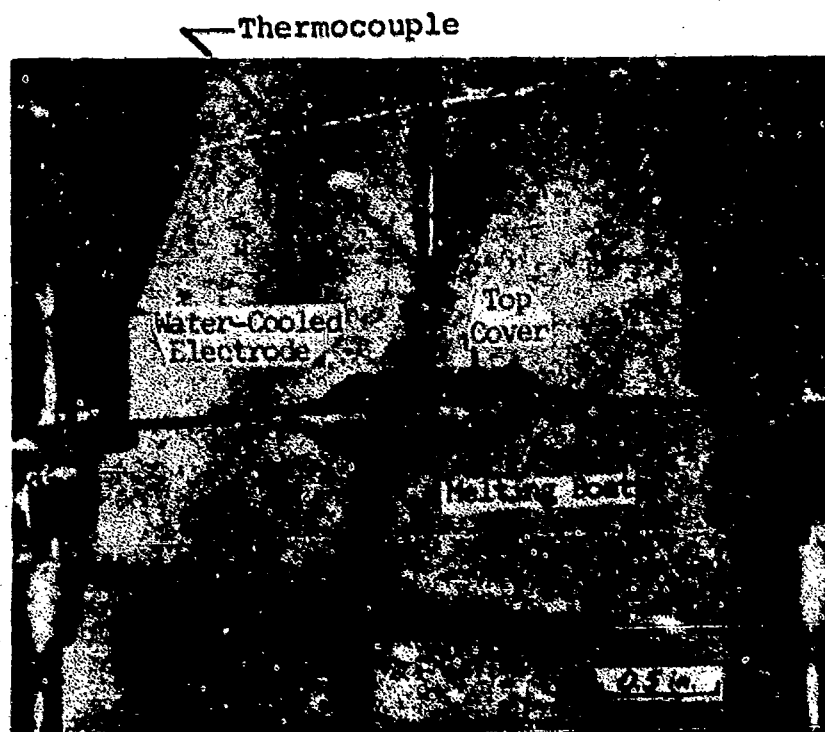
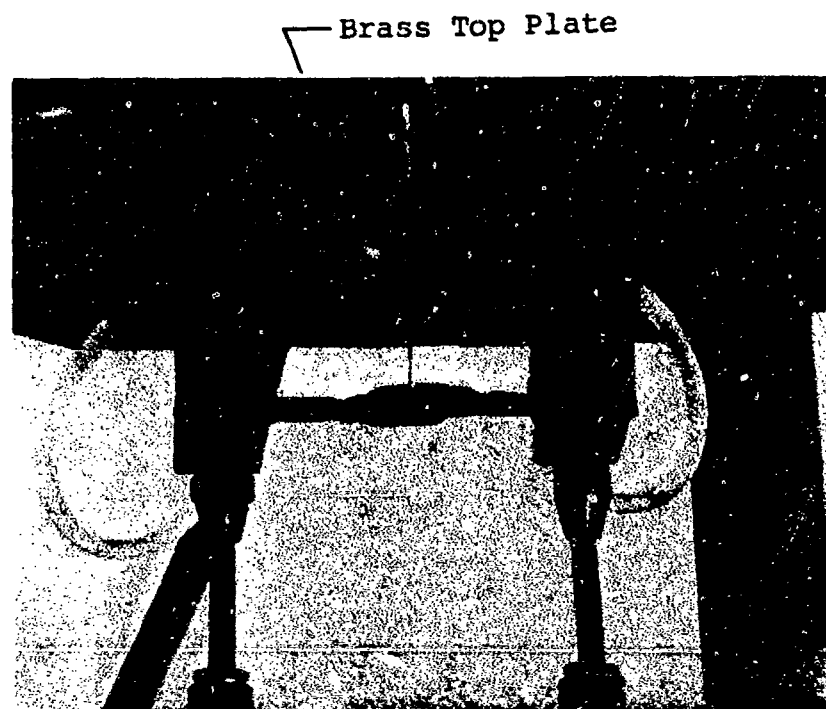


Figure 3.3 Close-up View of Electrode-Strip-Thermocouple Assembly.

base plate, and a 12 inch by 12 inch water-cooled brass top plate served to complete the enclosure and to support the strip heater assembly. Power was supplied to the strip heater via two 0.375-inch diameter, water-cooled copper rods contained within electrically insulated porcelain feedthroughs. Two water-cooled copper blocks (3.5 inches long, 1.25 inches high, and 0.875 inches wide) connected to the copper rods served as electrodes for the strip heater. A water-cooled radiation shield containing a small viewing port, an o-ring sealed thermocouple feedthrough, and a gas metering valve were also mounted on the top plate.

1. Vacuum System

The components of the vacuum system included a four-inch oil diffusion pump backed by a 50 liter/min. mechanical pump. The pressure monitoring system consisted of two thermocouple gages, an ionization gage, and a mechanical vacuum/pressure gage. Pressure control was provided by manual valving of the system.

2. Strip Heater

Previous investigations using the microfurnace (11) reported that tungsten was the most suitable material for use as a heating element/sample boat. The strip heater

used in this study was three inches long and 0.75 inches wide and featured an indentation for sample containment which measured 0.125-inch in depth. A cover strip containing a 0.25-inch circular opening to allow passage of the thermocouple was placed over the bottom strip. The cover strip prevented excessive BaO evaporation and reduced the magnitude of thermal gradients in the boat.

### 3. Temperature Measurement

The temperature of the strip heater was monitored using a Type C, tungsten-5%rhenium vs. tungsten-26%rhenium thermocouple. The thermocouple wire was 0.010 inch diameter and was contained within an alumina insulating sheath. The thermocouple was butt-welded under oil using a thermocouple welder (Burrel, Kup-L-Weld). After welding, the thermocouple bead was cleaned with methanol and examined for the presence of oxidation.

A Type C thermocouple calibration given by Tarter (12) was verified by melting 99.997 % pure alumina (Union Carbide, single crystal) and comparing the observed melting point with the literature value for alumina at 2070°C (38). The observed melting point was 2010°C, which was also the value reported by Tarter. The heating curve for the single

crystal alumina is shown in Figure 3.3. The calibration curve incorporated the alumina reference melting point error and the cold junction corection. The accuracy of the temperature measurment was determined to be  $\pm 30^{\circ}\text{C}$  based on the sum of the following error limits: a  $\pm 5^{\circ}\text{C}$  error for the thermocouple; a  $\pm 10^{\circ}\text{C}$  error in the calibration (worst case); and a  $\pm 15^{\circ}\text{C}$  error in reading the strip chart.

The thermocouple output signal was filtered by an L-C low-pass network to remove any A. C. component induced by the strip heater. The filtered signal was recorded on a strip chart recorder (Gould Model 110) capable of variable chart speeds and a range of full-scale input spans. All runs were recorded using a full-scale span of 50 mV. and chart speeds of either one or two inches per minute. Heating rates of  $300^{\circ}\text{C}/\text{min.}$  or  $450^{\circ}\text{C}/\text{min.}$  were used to generate heating curves.

#### 4. Power Supply

The power required for resistance heating of the tungsten boat was supplied by a silicon-controlled-rectifier power supply. In order to generate meaningful heating curves the programmed rate of temperature change must be linear. To obtain a linear heating rate, the power

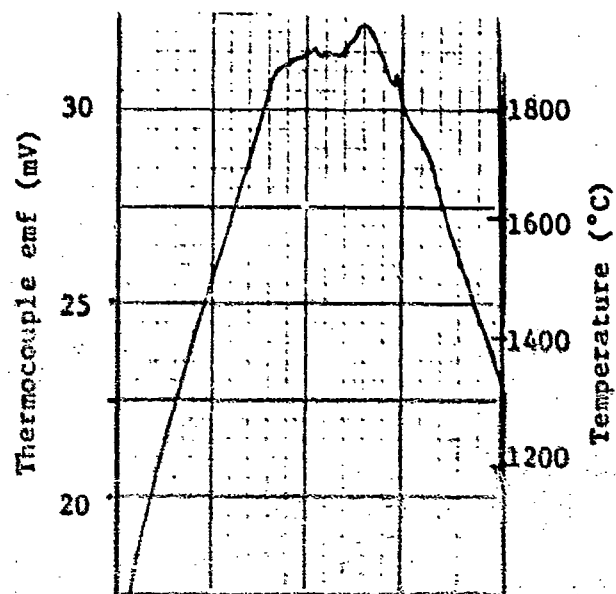


Figure 3.4. Heating Curve for  $\text{Al}_2\text{O}_3$ .



supplied to the furnace must be increased at an exponential rate. The power was controlled by using a specially shaped cam attached to the shaft of a variable resistor. The shape of the cam provided a nearly linear heating rate over the temperature range 25-2000°C. The resistor was located in the control circuit of the SCR power supply. The cam was driven through a friction drive by a variable speed motor so that a variety of heating rates could be used.

D. X-RAY ANALYSIS

X-ray powder diffraction analyses were performed on 32 compositions in order to determine the equilibrium phase assemblages at various temperatures. Samples were ground to -325 mesh in an alumina mortar and packed by a standard procedure (39) in an aluminum sample holder. The diffraction data was collected with a Philips-Norelco diffractometer using monochromated copper K-alpha x-radiation. The samples were analyzed at room temperature in a dynamic dry nitrogen atmosphere to prevent hydration. All precise measurements of interplanar spacings were made on data collected at a scan rate of 0.5 degrees per minute. Scattering angle values were corrected using tungsten

powder (cubic,  $Im\bar{3}m$ ,  $a_0 = 3.1648$  Å) as an internal standard. Qualitative analysis of chemical equilibrium phase assemblages were made on diffraction data collected at a scan rate of one degree per minute.

Powder patterns of various barium calcium aluminate phases were indexed with the aid of the computer program DICVOL (40). This program uses an algorithm based on variation of lattice parameters through successive dichotomies. An exhaustive search for unit cell solutions is performed over a user defined volume range. The volume space is divided into sections of  $400 \text{ Å}^3$  and possible solutions are searched for by variation of the direct parameters starting first with the smaller volume spaces. When suitable solutions are found, the lattice parameters are refined by the method of least squares. The first ten reflections of each XRD pattern were used to obtain the computer solutions. The lattice parameters from these solutions were then used to compute the position of the remaining interplanar spacings.

The lattice parameter,  $a_0$ , for compositions along the  $B_3A$ -CaO solid solution series was calculated from available XRD data. This was accomplished by calculating

$a_0$  values using the equation,

$$a_0 = d(h^2 + k^2 + l^2) \quad (3.2)$$

where  $a_0$  is the lattice parameter,  $d$  is the interplanar spacing and  $h$ ,  $k$  and  $l$  are components of the Bragg indices. The  $a_0$  values were then plotted as a function of  $\cos^2\theta$ . The lattice parameter was taken as the  $a_0$  value extrapolated to  $\cos^2\theta = 0$  using the method of least squares. Determinations using other extrapolation functions were attempted, however the results were considered unsatisfactory based on low correlation coefficients.

#### E. SCANNING ELECTRON AND OPTICAL MICROSCOPY

As a complement to the x-ray diffraction analyses, microscopic examination of several barium calcium aluminate compositions was also made to determine their equilibrium phase assemblages. The microscopic techniques used were scanning electron microscopy (SEM) and optical microscopy (petrographic and reflecting light.)

Samples were prepared for petrographic examination by the fusion of calcined powders in the tungsten-strip microfurnace. The resolidified material was crushed in an

alumina mortar and then separated into a -100 +150 mesh size fraction by passing the crushed fusion product through wire sieves. Sample grains were examined under oil and with crossed polarized white light. As a result of the high average refractive indices of the barium calcium aluminates and a large amount of associated dispersion, the anisotropic indices could not be determined. However, birefringence values could be estimated by observing the highest order interference color of the sample grains and using approximate values for the crystal thickness. The relation giving the estimated birefringence (N-n) is,

$$(N-n) = \Delta/t \quad (3.1)$$

where delta is the retardation value associated with the highest order interference color and t is the approximate crystal thickness. The optical sign of the grains was determined by conoscopic observations of the resulting interference figures and interference colors transmitted through a gypsum plate.

Polished sections for microscopic examination under reflected light were made by mounting fused barium calcium aluminate compositions in an epoxy resin (Quick

Mount) using 1.25 inch-diameter ring mounts. The samples were lapped with successively finer silicon carbide paper mounted on rotating wheels with final polishing accomplished on a cloth wheel charged with 1 um. diamond paste. Grinding and polishing was performed under kerosene to prevent hydration of the samples. Reflected light examinations were made with a metallograph (Richert) using white light from a xenon source.

Sample preparation for SEM analysis was identical to that for the preparation of polished sections, except that a 0.375 inch-diameter mounting ring was used to produce much smaller mounts. The samples were coated with either sputtered Au-Pd or deposited carbon to provide a conductive layer in order to prevent charging from the high energy electron beam. The scanning electron microscope (Coats and Welter, Cwikscan Model 100) was operated at an accelerating voltage of 16 kv. and a detector bias of 300 V. Image formation resulted from both secondary and backscattered electron components, with the majority being secondary electrons. There was enough compositional contrast present in the SEM images to see isolated phases dispersed in a polyphase matrix.

Energy dispersive x-ray spectrometry (EDS) was used to identify areas of free CaO in the polished sections. Energy spectra were acquired using the 16 KeV. electron beam and a KEVEX Microanalyst 1700 system. The spectra were collected after isolating various regions of the SEM images according to contrast and counting over small areas within those regions.

F. DIFFERENTIAL THERMAL ANALYSIS

Differential thermal analysis (DTA) curves were obtained for various barium calcium aluminate compositions using a Perkin-Elmer DTA 1700 system. Typical heating and cooling rates used were five and ten degrees per minute, with the exception of one series of runs which were made at 40°C/min. with approximately 100 mg. of sample in order to observe small heat effects associated with a displacive polymorphic transformation. In some cases, the DTA system was operated in a mode which performed microprocessor conditioning of the differential thermocouple signal to allow differential scanning calorimetric (DSC) interpretation of the observed thermal events. This mode of operation allowed the determination of heats of

transformation for the observed polymorphic phase transformations.

G.            OXIDATION OF BARIUM METAL

In an attempt to investigate the melting point of barium oxide a procedure was designed to allow complete in situ oxidation of barium metal in the tungsten-strip microfurnace to avoid contamination usually encountered with typical organic and carbonate decomposition reactions. Approximately 0.5 grams of pure barium metal was melted in the tungsten-strip microfurnace in dynamic hydrogen at one atmosphere pressure. The fused barium was then cooled to room temperature and the furnace chamber was evacuated to a pressure of 200 millitorr. Moist air was then bled into the furnace chamber until the pressure reached one atmosphere.

Power was then supplied to the strip and the temperature was slowly raised to 300°C. The sample temperature spontaneously increased to approximately 500°C as a result of the exothermic oxidation reaction. When the sample temperature maintained a constant value (300°C) the oxidation reaction was considered to be complete and the furnace chamber was again evacuated to 200 millitorr and then backfilled with hydrogen to a pressure of one

atmosphere. In order to insure a relatively oxygen free atmosphere the backfilling step was repeated once. The melting point was then determined using the procedure described in the section on microfurnace operation.



#### H. REACTION OF BARIUM CALCIUM ALUMINATES WITH TUNGSTEN

Compositions with molar ratios,  $B_3A$ ,  $B_4CA$ ,  $B_5C_3A_2$  and  $B_6CA_2$  were mixed with tungsten (in a ratio of 15 w% aluminate- 85w% tungsten) for 5 minutes in a alumina mortar. These mixtures were pressed into pellets using a 0.75 inch diameter stainless steel die, at 12,000 psi. The pellets, 0.25 to 0.50 inch thick, were then loaded into the strip furnace where the barium calcium aluminate was melted within the tungsten matrix in a dynamic hydrogen atmosphere. Temperatures for this operation were chosen just above the liquidous of the material ( $1700^{\circ}C$  for  $B_4CA$ ,  $B_5C_3A_2$  and  $B_6CA_2$  and  $1650^{\circ}C$  for  $B_3A$ ). The temperature was held for 1 minute inorder to insure complete melting of the aluminate. The BCA-W pellets were then transferred into a controlled-atmosphere SiC electric furnace where they were heat treated (in zero-grade argon gettered with tungsten powder) at  $1100^{\circ}C$  for 2, 4, 8, 17, 34, 39, 45, 69 and 90 hours. The pellets were removed from the furnace and stored in a vacuum desicator until they could be analyzed. Each sample was ground to <44 micron particle size and analyzed using x-ray powder diffraction to determine the reaction products.

## CHAPTER IV

### RESULTS AND DISCUSSION

Isothermal sections describing the equilibrium relationships in the high baria portion of the BCA system at  $1475^{\circ}\text{C}$  and  $1100^{\circ}\text{C}$  are presented in this chapter. A discussion of polymorphism and crystallography of various BCA phases is given with respect to the phase diagrams.

Solidus and liquidus temperatures are presented along with a critical interpretation of heating curves and thermal analysis theory. A phase diagram describing crystallization phenomena in terms of boundary curves, invariant points and primary phase fields is presented along with four vertical sections. Solid-liquid equilibria and crystallization sequences are presented and discussed by relating the vertical sections to features contained in the ternary diagram.

The melting point of  $\text{BaO}$  was determined by in situ oxidation of barium metal. This technique is discussed and the results are compared to previous investigations. Finally, a calculated  $\text{BaO-CaO}$  diagram is presented and discussed in terms of its relation to the ternary system.

A.        SUBSOLIDUS EQUILIBRIA

Using data obtained from x-ray diffraction and microscopic analysis of samples isothermally heat treated at 1475°C and 1100°C, the accurate locations of the solubility limits of  $B_{3-x}C_xA$  and  $B_{4-x}C_xA$   $Ca^{2+}$  substitutional solid solutions were determined. From this information Alkemade lines forming the BA- $B_3A_{ss1}$ -CaO and  $B_3A_{ss1}$ - $B_4A_{ss1}$ -CaO compatibility triangles were established. Approximate locations of Alkemade lines forming the two boundaries of the  $B_{4-x}C_xA$ -BaO-CaO compatibility triangle were derived from solidus temperature data. Isothermal sections constructed from these results depicting the 1475°C and 1100°C equilibria are presented in Figures 4.1 and 4.2. XRD results used to construct the isothermal sections are tabulated in Appendix A.

1.        Solid Solubility Limits and Alkemade Lines at 1475°C

The lattice parameter,  $a_0$ , was determined from XRD data of compositions located along the  $B_3A$ -CaO solid solution series. The lattice parameter was plotted as a function of composition (CaO content) as shown in Figure 4.3. This technique, known as the parametric method, was used to determine the  $Ca^{2+}$  solubility limit. As the calcium

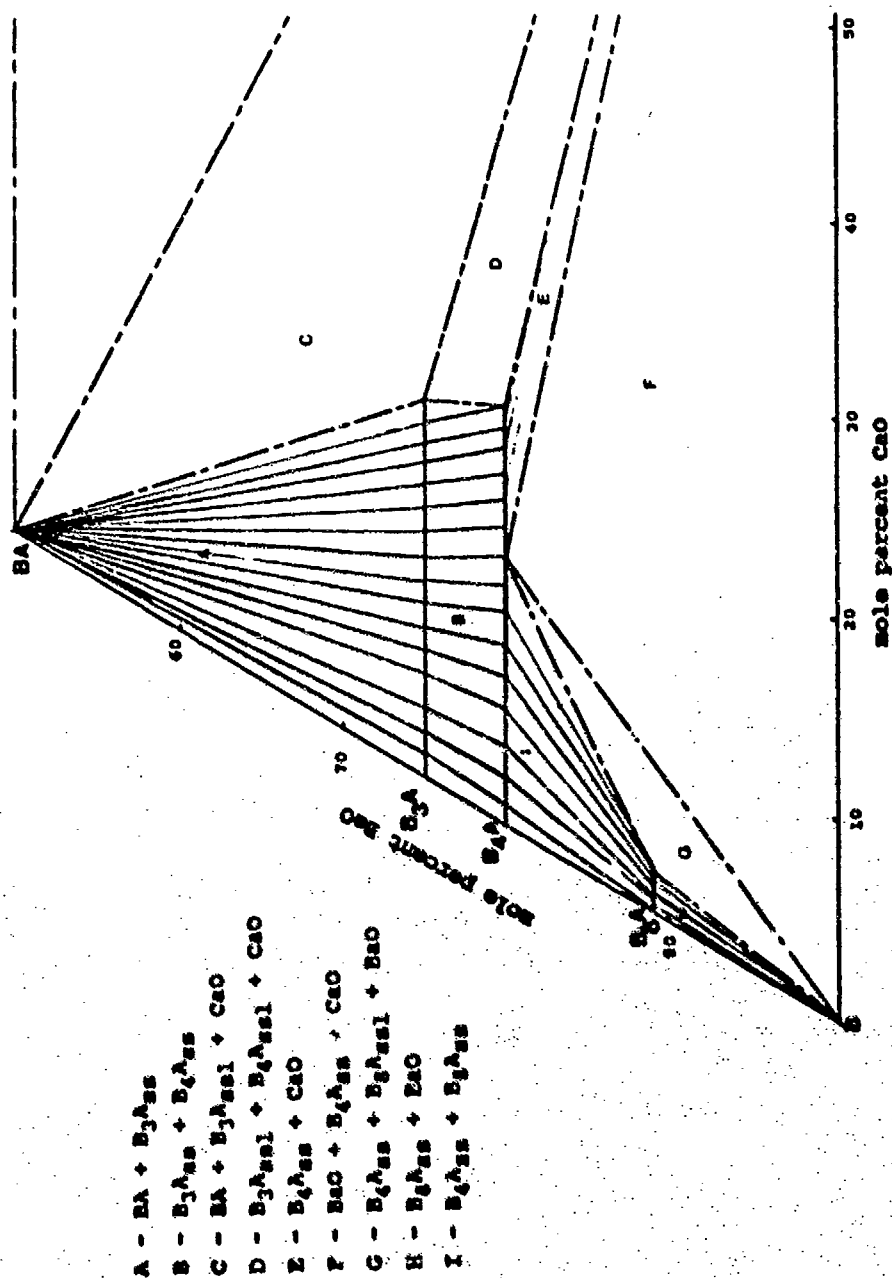


Figure 4.1. Partial Isothermal Section at 1475°C of the BaO-CaO-Al<sub>2</sub>O<sub>3</sub> System.



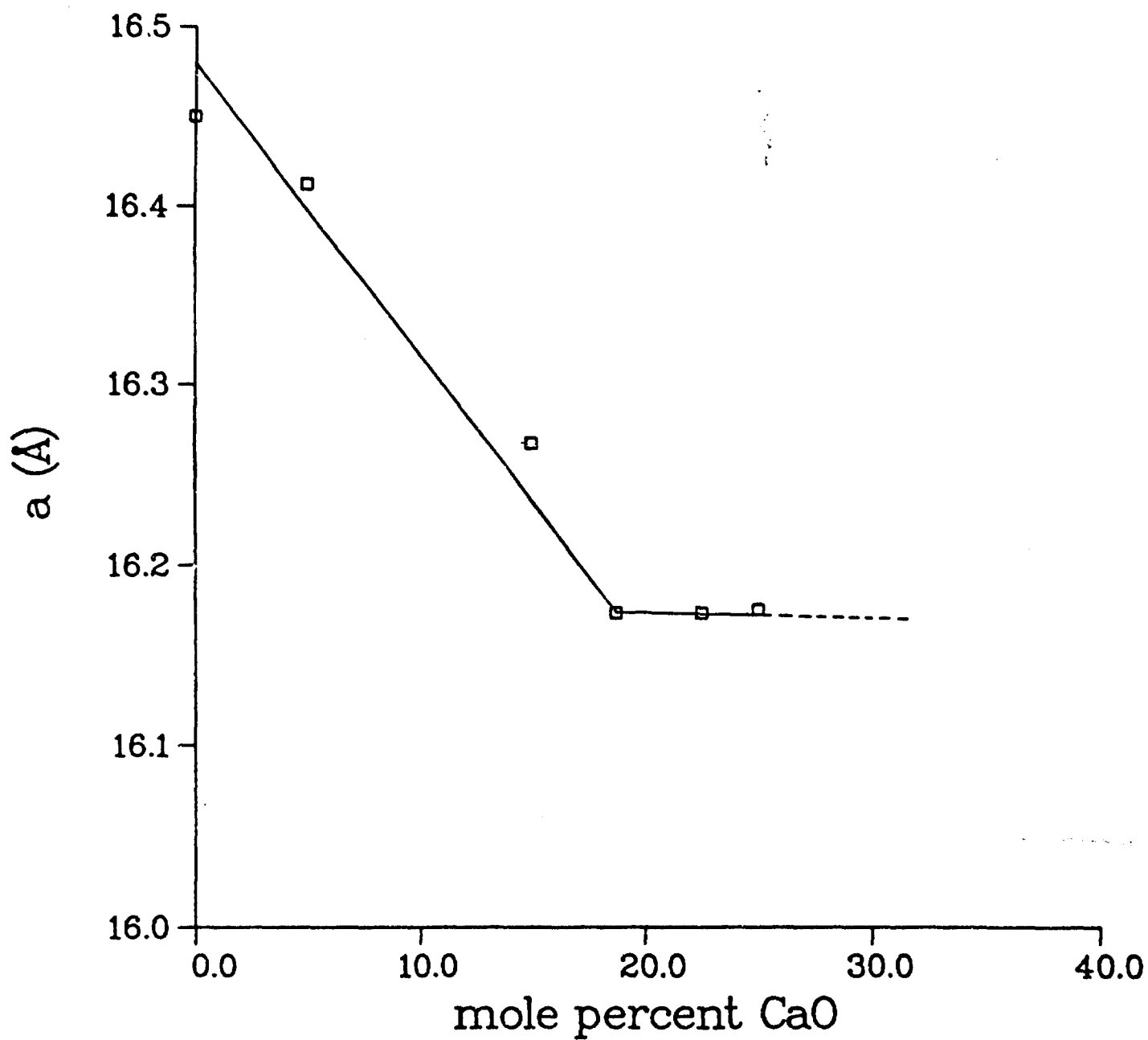


Figure 4.3. Plot of  $a_0$  of  $B_{3-x}C_xA$  versus Calcium Content at  $1475^\circ\text{C}$ .

content in the crystal structure increases, the length of the cell edge decreases. This is to be expected, since the smaller  $\text{Ca}^{2+}$  ions are substituting for the larger  $\text{Ba}^{2+}$  ions on the divalent metal ion sites and the obvious result would be a contraction of the unit cell volume.

At 18.75 mole percent  $\text{CaO}$ , contraction of the unit cell of the  $\text{B}_{3-x}\text{C}_x\text{A}$  stopped and the lattice parameter maintained a constant value for compositions with  $\text{CaO}$  contents greater than 18.75 mole percent. At the  $\text{Ca}^{2+}$  solubility limit, addition of any more  $\text{Ca}^{2+}$  would result in the formation of free  $\text{CaO}$  and  $\text{BA}$ . Since the number of phases in the system for compositions beyond the  $\text{Ca}^{2+}$  solubility limit is three, the composition of the  $\text{B}_{3-x}\text{C}_x\text{A}$  solid solution must remain constant as required by the phase rule. Under the condition of constant composition, no further changes in cell volume will occur past the solubility limit. Using this information the solubility limit of  $\text{Ca}^{2+}$  in  $\text{B}_{3-x}\text{C}_x\text{A}$  at  $1475^\circ\text{C}$  was taken as 18.75 mole percent  $\text{CaO}$ .

A similar method was used for determining the solubility limit of  $\text{Ca}^{2+}$  in  $\text{B}_{4-x}\text{C}_x\text{A}$ . The major difference in the graphical technique was that the interplanar spacing

for only one reflection was plotted as a function of CaO content as opposed to an extrapolated lattice parameter or cell volume. The use of only one interplanar spacing value is subject to greater error in measurement than the extrapolated lattice parameter; however, with an internal standard correction it was thought that a useful curve was obtained. A plot of the interplanar spacing of the 400 reflection as a function of composition is given in Figure 4.4. The composition at which the spacing became constant was determined to be 20.5 mole percent CaO and this was taken as the solubility limit. Compositions containing less than 21.00 mole percent CaO were fused, held at 1475°C for 30 minutes, and examined with a petrographic microscope. Only a single phase was observed. Compositions containing more than 21 mole percent CaO prepared in a like manner contained the limit solid solution phase of  $\text{Ca}^{2+}$  in  $\text{B}_{4-x}\text{C}_x\text{A}$  plus an isotropic phase which was suspected to be the limit solid solution of  $\text{Ca}^{2+}$  in  $\text{B}_{3-x}\text{C}_x\text{A}$ .

From the composition of the limit solid solution of  $\text{Ca}^{2+}$  in  $\text{B}_{3-x}\text{C}_x\text{A}$  the two Alkemade lines joining the limit with CaO and BA were established. The equation of the  $\text{B}_{3-}$



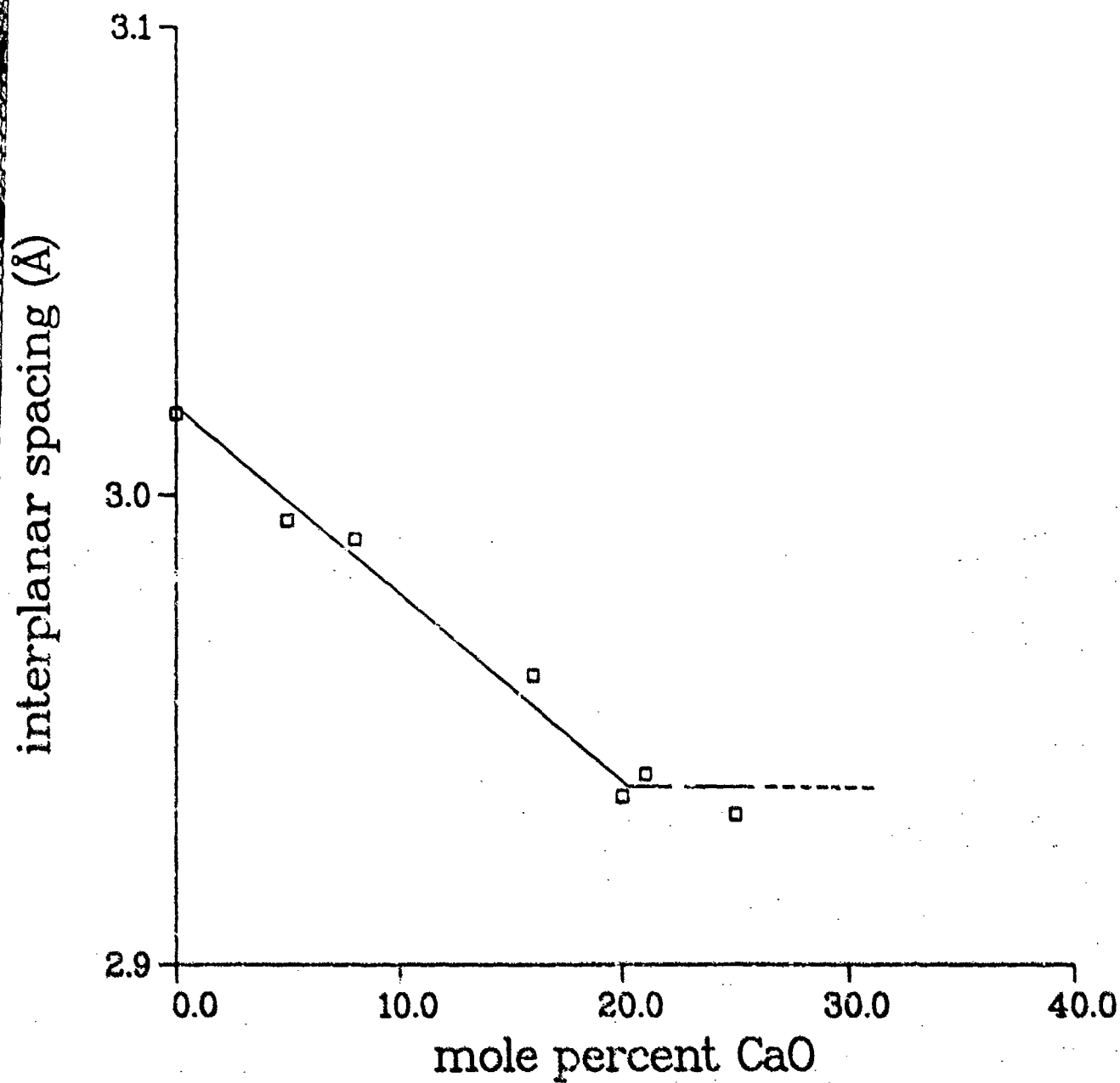


Figure 4.4. Plot of the (400) Interplaner Spacing of  $B_{4-x}C_xA$  Versus Calcium Content at  $1475^{\circ}\text{C}$ .

$x\text{C}_x\text{A}_{\text{ss1}}\text{-CaO}$  Alkemade line over the range, zero to 25 mole percent  $\text{Al}_2\text{O}_3$ , was determined as:

$$C = -3.25A + 100 \quad (4.1)$$

where C is the total mole percent CaO and A is the total mole percent  $\text{Al}_2\text{O}_3$ . Likewise, the equation of the  $\text{B}_{3-x}\text{C}_x\text{A-Ba}$  Alkemade line over the composition range 25 to 50 mole percent  $\text{Al}_2\text{O}_3$  has the form,

$$C = -0.75A + 37.5 \quad (4.2).$$

In a similar manner, the equation of the  $\text{B}_{4-x}\text{C}_x\text{A}_{\text{ss1}}\text{-CaO}$  Alkemade line was determined using the composition of the corresponding  $\text{B}_{4-x}\text{C}_x\text{A}$  solubility limit. The relation is given as,

$$C = -3.95A + 100 \quad (4.3).$$

The position of the Alkemade line separating the  $\text{B}_{4-x}\text{C}_x\text{A-BaO-CaO}$  compatibility triangle from the  $\text{B}_{4-x}\text{C}_x\text{A-CaO}$  two-phase compatibility region was determined by noting a discontinuity in the solidus temperature along the constant 15 mole percent  $\text{Al}_2\text{O}_3$  plane. This discontinuity indicated the point of intersection of the Alkemade line

with the plane. The position was established by extending the line to the CaO corner and calculating the equation,

$$C = -4.33A + 100 \quad (4.4).$$

From the equation of the line, the composition of the  $B_4A_{ss}$  end which forms the upper vertex of the  $B_{4-x}C_xA$ -BaO-CaO triangle could be determined by extrapolation to 20 mole percent  $Al_2O_3$ . This composition was calculated as  $B_{3.33}C_{0.67}A$  (13.4 mole percent CaO). However, since the occurrence of the discontinuity could only be determined to an accuracy of 2.5 mole percent CaO, the composition could be shifted as far as  $B_{3.5}C_{0.5}A$ .

The solubility of  $Ca^{2+}$  in  $B_{8-x}C_xA$  was taken to be 2 mole percent CaO as reported by Appendino (23). It was felt that this was a reasonable assumption since the  $Ca^{2+}$  solubility in  $B_{4-x}C_xA$  and  $B_{3-x}C_xA$  solid solutions appeared to be independent of temperature (temperature dependence of solubility will be discussed in the next section.) The position of the  $B_{4-x}C_xA$ -BaO Alkemade line was estimated from solidus data along the constant 15 mole percent  $Al_2O_3$  plane and is very close to Appendino's prediction at 1250°C. This established the  $B_{4-x}C_xA$ - $B_{8-x}C_xA_{ss1}$ -BaO

compatibility triangle as a narrow three-phase region.

## 2. Equilibria at 1100°C

Parametric plots for  $B_{3-x}C_xA$  and  $B_{4-x}C_xA$  solid solutions gave solubility limits of 18.75 and 20.50 mole percent CaO respectively for heat treatments at 1100°C for 24 hours (Figures 4.5 and 4.6.) Comparison of these values with the solubility limits determined at 1475°C show that the solubility of CaO in both crystal structures is independent of temperature from 1100°C to 1475°C (near the solidus.) Consequently, no changes in position of the  $B_{3-x}C_xA_{ssl}$ -BA,  $B_{3-x}C_xA_{ssl}$ -CaO and  $B_{4-x}C_xA_{ssl}$ -CaO Alkemade lines occurs over that temperature range. It was also assumed that the  $B_{3.33}C_{0.67}A$ -CaO Alkemade line remained stationary with respect to the 1475°C isothermal section.

Inspection of XRD traces of the  $B_{4-x}C_xA$  solid solution series (Figure 4.7) shows that, as the  $Ca^{2+}$  content of the solid solution increases, a number of new reflections appear and grow while others simply appear to split, with the total intensity distributed among the offspring reflections. The major reflections present in the XRD pattern of pure  $B_4A$  do not decrease in intensity as the new reflections grow. This suggests that the patterns

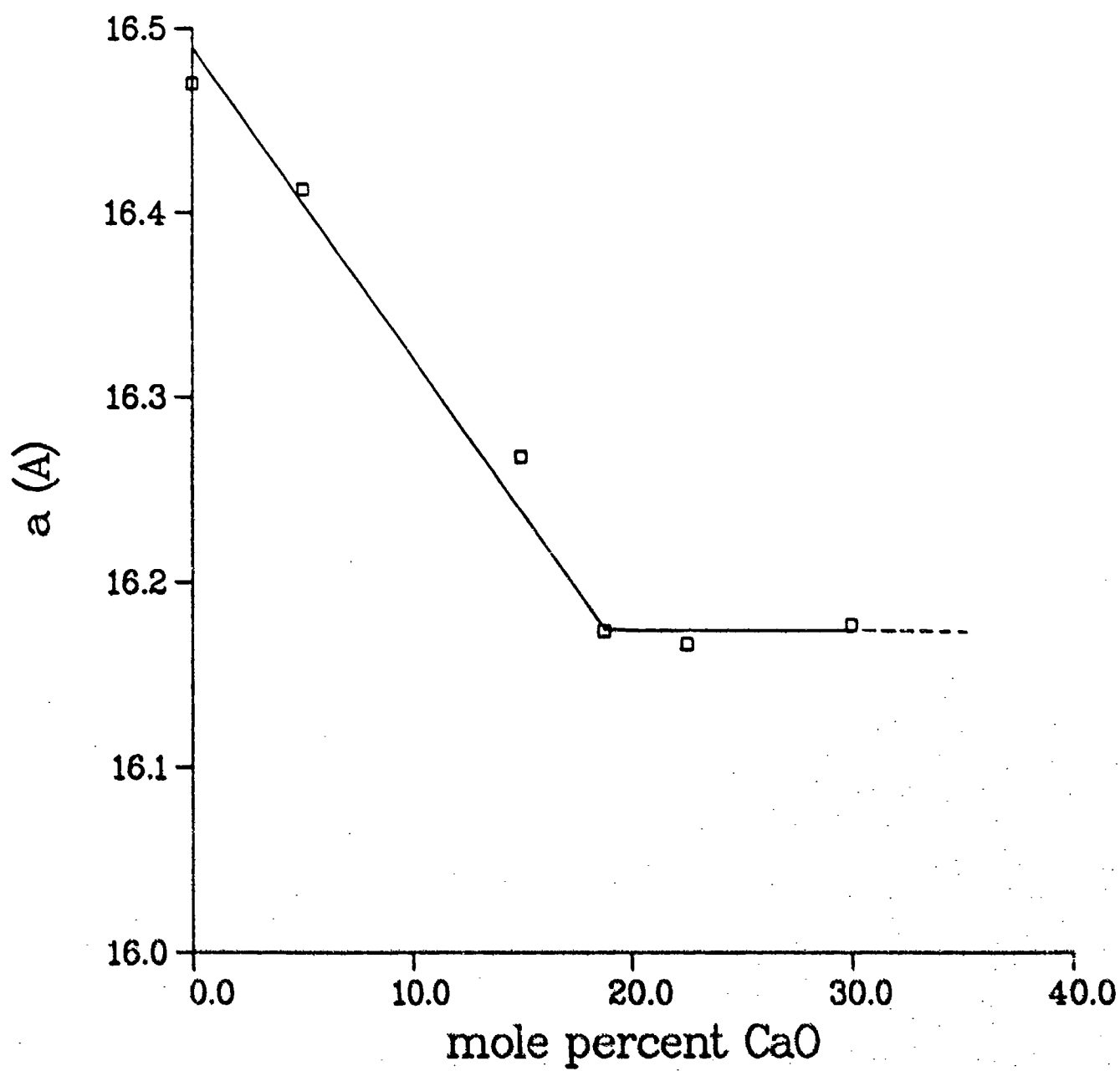


Figure 4.5. Plot of  $a_0$  of  $B_3-xC_xA$  Versus Calcium Content at  $1100^\circ\text{C}$ .

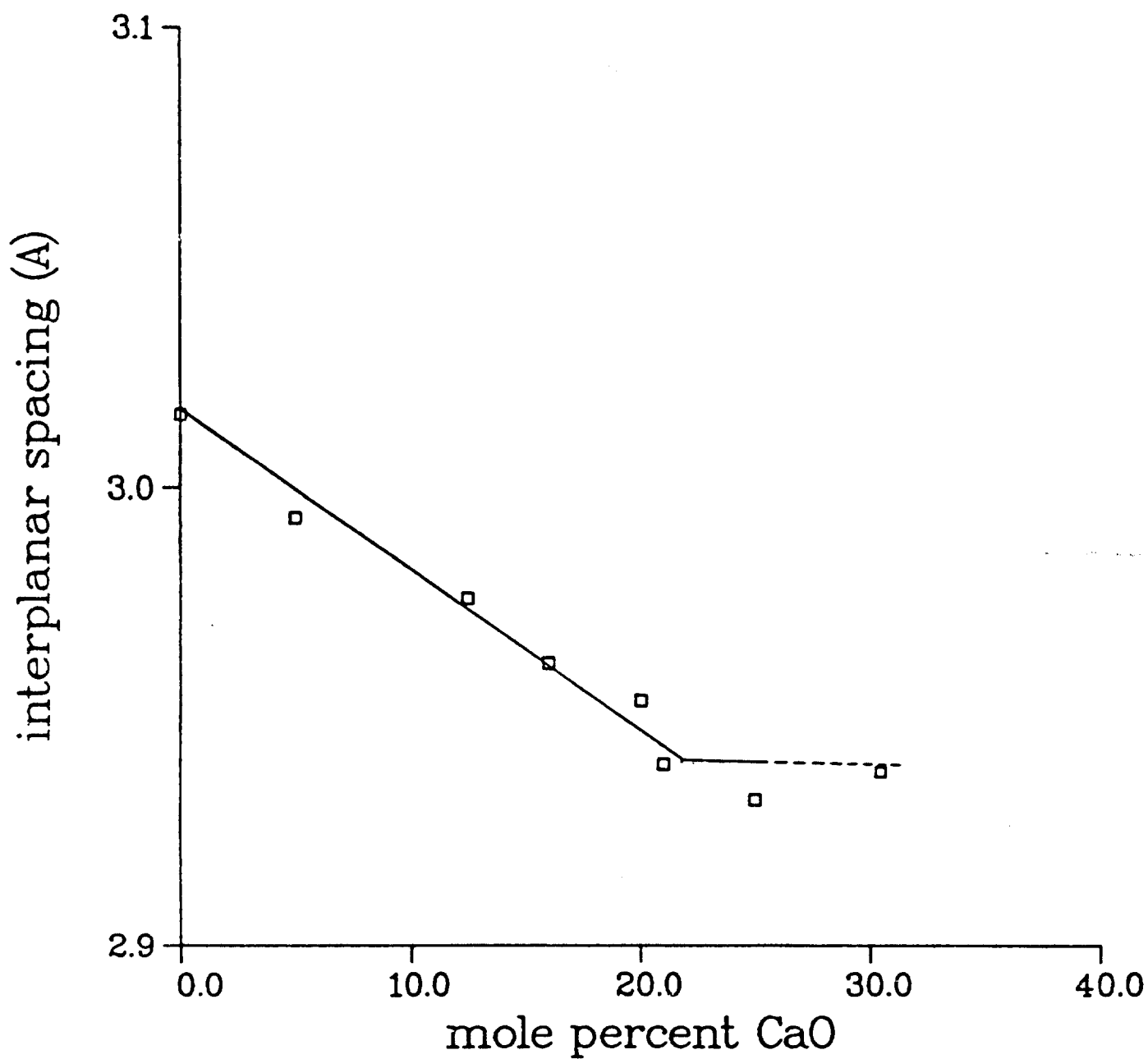


Figure 4.6. Plot of the (400) Interplaner Spacing of  $B_{4-x}C_xA$  Versus Calcium Content at  $1100^{\circ}\text{C}$ .

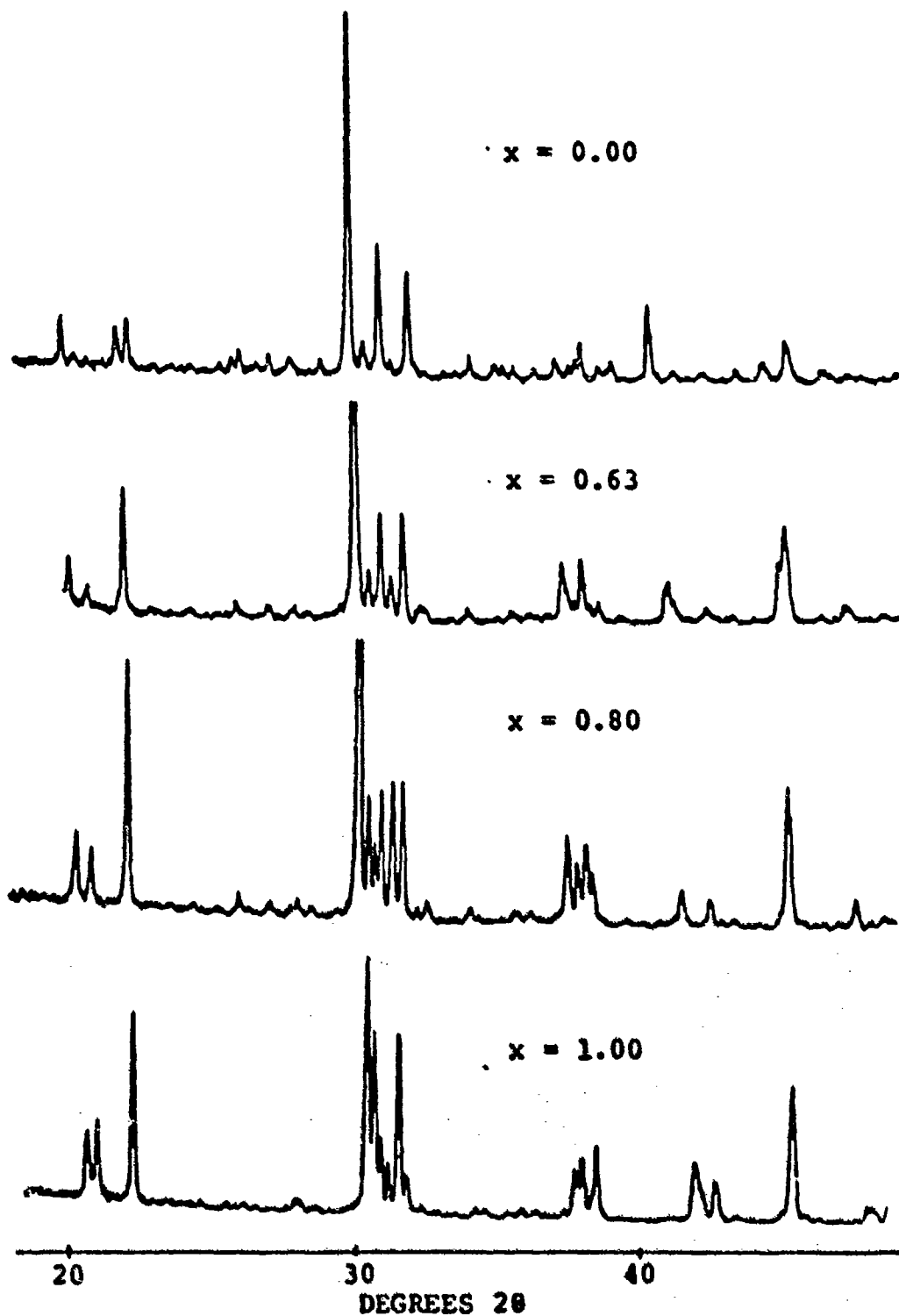


Figure 4.7. Comparison of the XRD Traces of  $B_{4-x}C_x$  Solid Solutions Showing the Effect of Calcium Substitution in the Lattice.

containing the new reflections are those of a polymorphic modification similar to pure  $B_4A$ . This effect is strongly indicative of a lowering of crystal symmetry by the substitution of a smaller  $Ca^{2+}$  ion for the  $Ba^{2+}$  ion in the crystal structure. Since the parametric plot showed a continuous decrease in the interplaner spacing with increasing  $Ca^{2+}$  content, the two-phase region required by the phase rule (which should contain the high- and low-symmetry polymorphs) was assumed to be very narrow. The polymorphic modifications appear to be structurally similar, based on the fact that both the high- and low-symmetry forms contain a large number of common reflections. This type of polymorphism has been found in numerous solid solution systems; some examples of this are the  $ZrO_2$ - $CeO_2$  system and the  $Ca_3Al_2O_6$ - $Na_2O$  system.

Since a two-phase region along the  $B_{4-x}C_xA$  solid solution series is indicated by the phase rule, a three-phase region must also exist in a region bounded by the two solid solution lines. The corner of the three-phase region having the composition,  $B_{3.33}C_{0.67}A$ , was the only vertex which could be firmly established since it was also the end composition of the  $B_{3.33}C_{0.67}A$ - $CaO$  Alkemade line. The



lower left-hand corner of the three-phase region corresponds to the composition,  $B_{3.60}C_{0.40}A$ . The location of this corner was estimated by noting that the XRD patterns of compositions  $B_{3.47}C_{0.79}A$  and  $B_{3.70}C_{0.92}A$  were significantly different in appearance (Figure 4.8.) The two compositions were concluded to be located near and on opposite sides of an Alkemade line. On this basis, an Alkemade line was drawn in such a way that these two compositions were located on opposite sides and equidistant from the line. The line was extrapolated to 20 mole percent  $Al_2O_3$  to give the terminal composition of the Alkemade line and consequently the left-hand corner composition.

### 3. Verification of Equilibrium at 1100°C

In order to verify that the 1100°C isothermal section was indeed an equilibrium diagram, several compositions located in various regions of the diagram were heated at 1100°C for 500 hours, quenched to room temperature and then analyzed by XRD. The compositions chosen for long-term heat treatment were:  $B_2CA$ ,  $B_3CA$ ,  $B_5C_3A_2$  and  $B_4CA$ . No significant differences were observed when XRD traces of these compositions were compared with

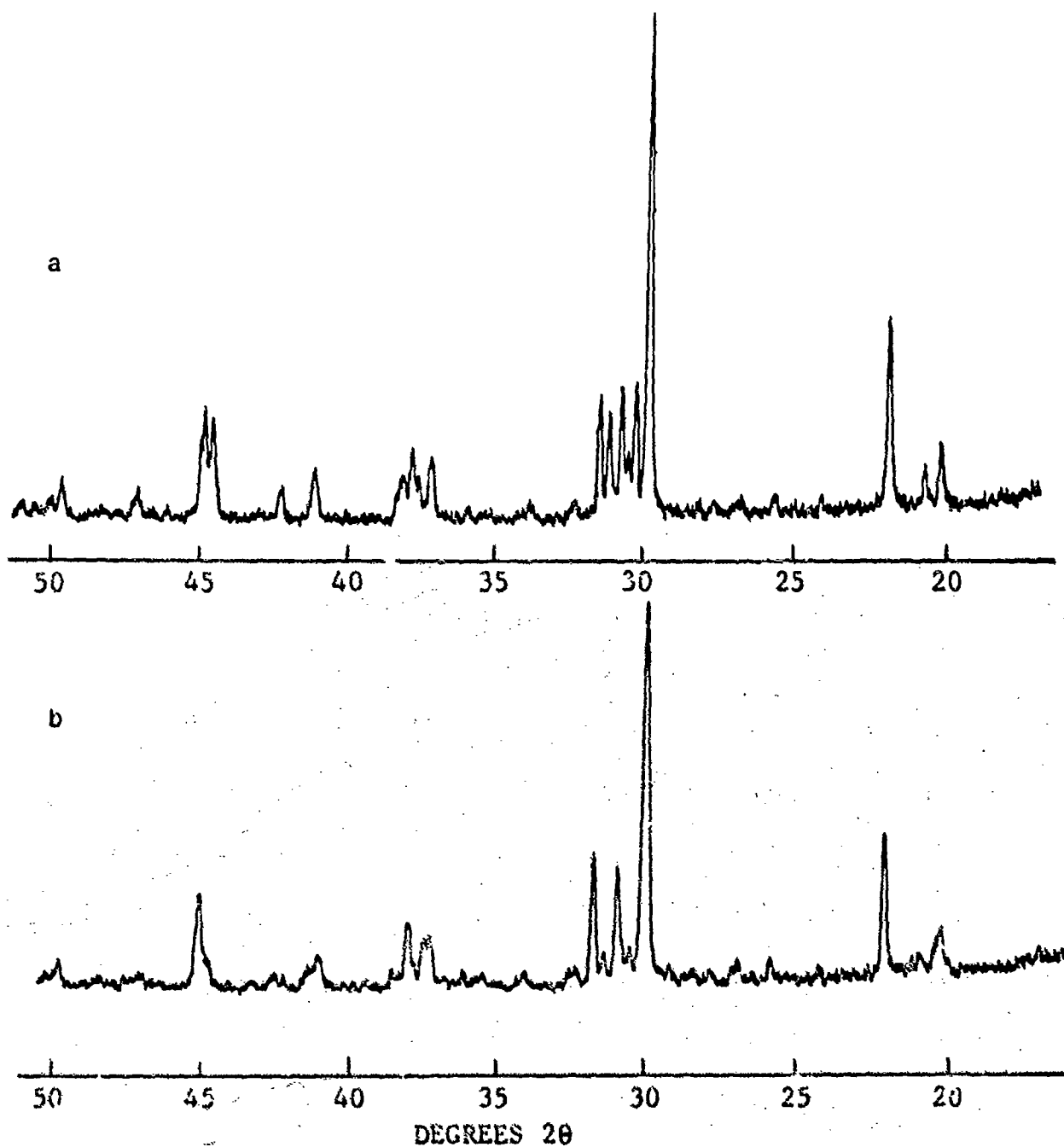


Figure 4.8. XRD Traces of (a)  $B_{3.47}C_{0.79}A$  and (b)  $B_{3.70}C_{0.92}A$  quenched from 1100°.

those of the same compositions heated for 24 hours at 1100°C, with the exception of B<sub>4</sub>CA. It should be noted that B<sub>4</sub>CA has the highest baria content of the four compositions, and furthermore, contains free BaO as a part of its three-phase assemblage. As mentioned in Chapter Two, free BaO exhibits a high vapor pressure at elevated temperatures and consequently a high evaporation rate. It is suspected that the difference in the XRD patterns of the 500 and 24 hour treated samples can be attributed to a compositional change resulting from BaO evaporation. The compositional change, if great enough, would place the resulting mixture in the B<sub>4-x</sub>C<sub>x</sub>A-CaO compatibility region, which would yield an XRD pattern with a different appearance.

#### B. POLYMORPHISM IN THE BCA SYSTEM

Differential thermal analysis curves (using "DSC" signal processing) were obtained for pure B<sub>3</sub>A and B<sub>3-x</sub>C<sub>x</sub>A solid solutions containing 5, 10, 15 and 18.75 mole percent CaO. The DTA curve for pure B<sub>3</sub>A is shown in Figure 4.9. The endotherm occurring at 366°C was associated with a rapid, reversible polymorphic inversion first reported by Glasser (41). It was noted that the inversion temperature

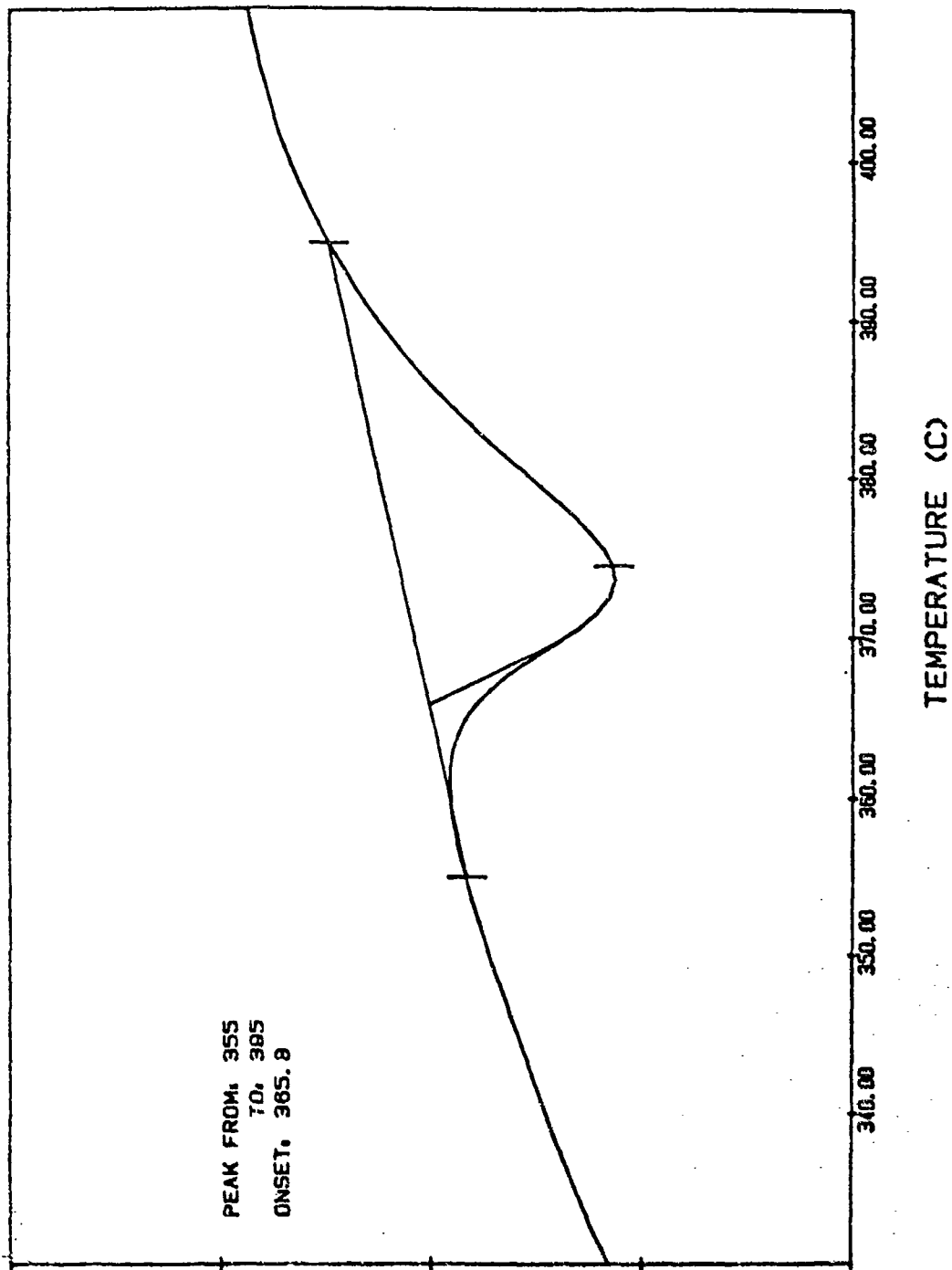


Figure 4.9. DTA Curve for Pure B<sub>3</sub>A Showing Heat Effect of Polymorphic Transformation.

observed in this study was 84°C lower than that reported by Glasser. The inversion was found to occur over a temperature interval of approximately 30 degrees, with a heat of transformation of 0.11 calories/gram. This small heat of inversion is only 1/25 that of the  $\alpha \rightarrow \beta$  quartz transformation, which strongly suggests the inversion is displacive and that the high and low temperature forms are structurally similar. The small heat effect associated with the inversion is most probably due to small changes in the second order atomic coordination.

The heat of inversion was reduced by substitution of  $\text{Ca}^{2+}$  for  $\text{Ba}^{2+}$  in the  $\text{B}_3\text{A}$  structure. DTA curves of samples containing greater than 5 mole percent  $\text{CaO}$  contained only extremely weak endotherms and the sample containing 18.75 mole percent  $\text{CaO}$  (the solubility limit) was completely thermally inactive from room temperature up to 1100°C. The inversion temperature of solid solutions containing less than 18.75 mole percent  $\text{CaO}$  was unaffected by  $\text{Ca}^{2+}$  substitution. The effect of  $\text{Ca}^{2+}$  on eliminating the polymorphic inversion indicates that either the high or the low temperature form is stabilized over the temperature interval 25 to 1100°C.

A sample of pure fused  $B_3A$  was crushed and examined with a petrographic microscope using crossed-polarized white light. The material exhibited distinct birefringence and it was concluded that the crystal symmetry of  $B_3A$  must be lower than cubic. This is in contradiction to the most recent Powder Diffraction File card (Number 25 - 75), which reports the compound  $B_3A$  as cubic with the space group symmetry,  $Pa\bar{3}$ . The card does not list any optical data and apparently no optical analysis has ever been reported in the literature. Based on the optical analysis performed in this work it appears that  $B_3A$  possesses only psuedo-cubic symmetry. The  $B_3A$  crystals produced an interference figure consistent with a uniaxial negative material. Unfortunately, it was not possible to determine the refractive indices due to reaction of the  $B_3A$  crystals with the higher-index oils.

Petrographic examination of the fused solid solution compositions revealed that substitution of  $Ca^{2+}$  reduced the birefringence of the crystals and that crystals which contained 18.75 mole percent  $CaO$  were completely isotropic. The decrease in optical birefringence by replacement of  $Ba^{2+}$  by  $Ca^{2+}$  suggests that the

crystallographic anisotropy is simultaneously being reduced until at some composition between 15 and 18.75 mole percent CaO the crystals acquire true cubic symmetry. This effect suggests that the most highly probable symmetry of the high-temperature polymorph of pure  $B_3A$  is cubic, and that substitution of  $Ca^{2+}$  in the lattice stabilizes this form at room temperature.

Close examination of the XRD pattern of pure  $B_3A$  revealed splitting of the 800 and 840 reflections (Figure 4.10 a.) This type of splitting is ascribed to separation of h00-type reflections into h00 and 00h components, resulting from lower multiplicities associated with tetragonal or lower crystal symmetries. Solid solutions containing 5 mole percent CaO or greater yielded XRD patterns consistent with a cubic lattice, with no resolved splitting of any observed reflections (Figure 4.10 b.)

A portion of the sub-solidus vertical section containing the  $B_3A$ -CaO solid solution series that exhibited the high-low type polymorphism is shown in Figure 4.11. Tentative boundaries were included to indicate two-phase regions required by the phase rule. However, it should be noted that these boundaries may be extremely narrow and

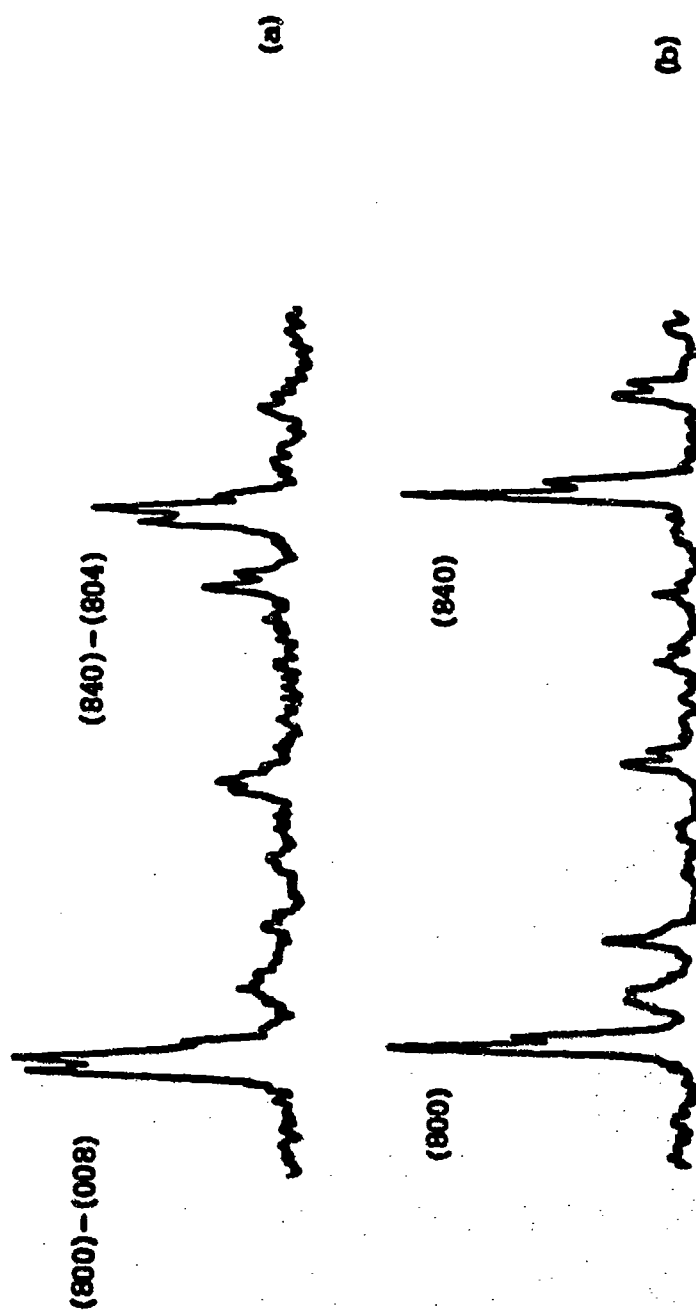


Figure 4.10. XRD Traces containing the (800) and (840) Reflection Groups for (a) Pure B<sub>3</sub>A and (b) B<sub>3.80</sub>Co<sub>0.20</sub>A Solid Solution.



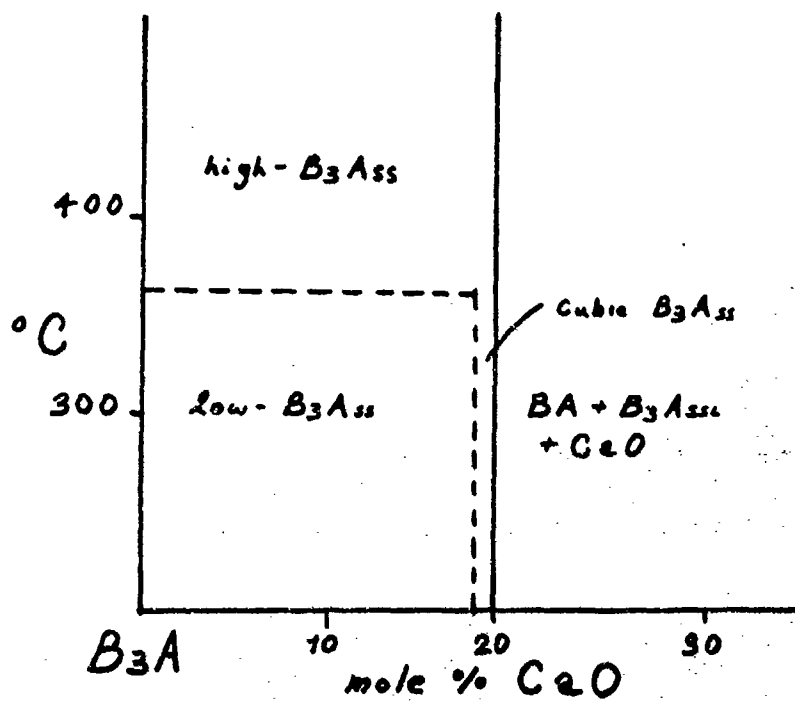


Figure 4.11. Partial Subsolidus Vertical Section Containing the  $B_{3-x}C_xA$  Solid Solution Series.

that the displacive inversion of  $B_{3-x}C_xA$  is most probably diffusionless and would not necessarily require a two-phase region of chemical equilibrium for conversion to the polymorphic modification.

1. Polymorphism of  $B_{4-x}C_xA$  Solid Solutions

The  $B_{4-x}C_xA$  solid solution containing 20 mole percent CaO was discovered, by XRD analysis, to exist as two polymorphic modifications. XRD patterns for the two polymorphs are shown in Figure 4.12. The high-temperature form (which will be referred to henceforth as Type I) was metastably preserved at room temperature by rapidly quenching the solid solution from above the liquidus to room temperature in a dynamic hydrogen atmosphere. The ability to "quench in" the Type I form indicates the transformation is diffusion-controlled and reconstructive as opposed to a displacive type of inversion. The Type I form converted completely to the low form (Type II) after a 15 minute heat treatment at  $1300^{\circ}\text{C}$ . XRD traces of melt-quenched samples held at temperatures between  $1475^{\circ}\text{C}$  and the solidus and then subsequently quenched to room temperature contained only reflections belonging to the Type I form. Similarly prepared samples heated below

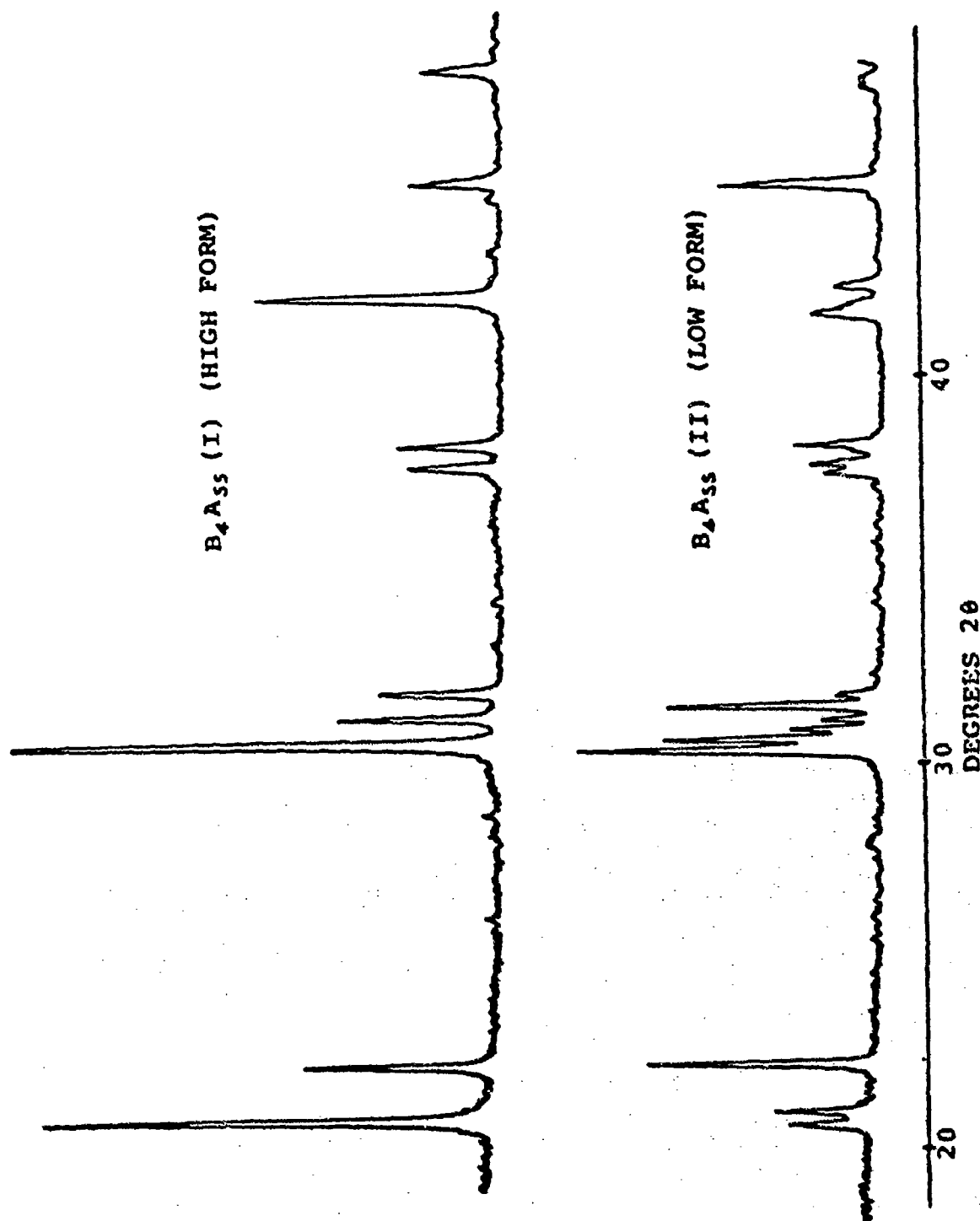


Figure 4.12. Comparison of the XRD Traces of the Two Polymorphic Forms of  $B_4-xC_xA$  containing 20 Mole Percent.

1475°C were found to contain a mixture of the two polymorphs. This established 1475°C as the inversion temperature. Samples containing only the Type II (low form) were heated at 1500°C for one hour and then were rapidly quenched to room temperature. The samples contained only a small amount of the Type I polymorph. It was determined that the kinetics for the Type II-to-Type I conversion in the solid state are much slower than for the reverse reaction. The ease with which the Type I polymorph is formed from the liquid derives from the fact that the atomic diffusion rates are generally several orders of magnitude higher in liquids than in solids. The high-temperature phase can easily be constructed by nucleation in the liquid, whereas nucleation in the solid state may involve significant energetic reconstruction from the low-temperature phase. Inspection of the XRD patterns of the Type I and Type II polymorphs shows that there are numerous reflections common to both forms. Some reflections appear to have split in the low form, which usually suggests a decrease in crystallographic symmetry.

Petrographic analysis yielded biaxial positive interference figures for both the high and low forms of

B<sub>3</sub>CA, with no significant differences in the estimated 2V angle between the two forms. Since the polymorphs possess a biaxial indicatrix, the crystallographic symmetry must be orthorhombic or lower. The similarities in the optical properties of the two polymorphs also suggests a close structural similarity with the Type II, form most probably a lower-symmetry derivative structure of the high form.

B<sub>4-x</sub>C<sub>x</sub>A solid solutions containing less than 20 mole percent CaO converted to the Type II form more slowly than B<sub>3</sub>CA and the inversion temperatures could not be easily measured and are not given. However, the solid solutions containing less than 20 mole percent CaO were stable at 1300°C, which suggests that the inversion temperature is lowered as the CaO content decreases. This effect is proposed in a vertical section presented in a later section.

## 2. Comparison of Diagrams with Previous Investigations

Comparison of the isothermal sections developed in this investigation with the 1250°C section reported by Appendino (23) reveals a number of marked differences. The main difference in the 1475°C section is the absence of the miscibility gap located along the B<sub>4-x</sub>C<sub>x</sub>A solid solution

series. This resulted in the disappearance of several compatibility relationships, including the three-phase region bounded by the  $B_{3-x}C_xA$ - $B_{4-x}C_xA$  solid solution lines. Also, the  $B_{4-x}C_xA$  series has been extended to include the composition  $B_3CA$ , which Appendino reported as being a unique compound.

The 1100°C isothermal section is somewhat similar in appearance to Appendino's diagram. A miscibility gap is shown in the  $B_{4-x}C_xA$  series, with the resulting three-phase region located above the solid solution line. However, the region containing  $B_3CA$  is presented as a polymorphic modification of the  $B_{4-x}C_xA$  series, exhibiting a compositional range extending from 13.3 to 21 mole percent CaO.

### 3. Crystallography of Barium Calcium Aluminate Phases

The crystal systems and lattice parameters were determined for  $B_3A$  and  $B_{4-x}C_xA$  Type I and II solid solutions. The results of the XRD powder pattern indexing calculations are summarized in Tables 4.1 and 4.2.

The compound  $B_3A$  was determined to belong to the orthorhombic crystal class. As can be seen from the lattice parameters, the length of the c cell edge is

Table 4.1. Crystal Data for  $B_3CA$  Type I and Type II Polymorphs

Form	system	a (Å)	b (Å)	c (Å)	$\beta$ (°)
Type I	orthorhombic	12.278	12.078	10.192	
Type II	monoclinic	8.867	18.154	9.080	82.30

Table 4.2. Crystal Data for  $B_3A$  and  $B_3A_{SS1}$

Composition	system	a (Å)	b (Å)	c (Å)
$B_3A$	orthorhombic	16.460	14.821	7.871
$B_3A_{SS1}$	cubic	16.183		

roughly one-half the length of the b cell edge. This characteristic of the material most likely explains the apparent uniaxial optical behavior observed with the polarizing microscope, since the doubling of the c axis would tend to simulate tetragonal symmetry. As  $\text{Ca}^{2+}$  substitution occurs, the crystal symmetry approaches a cubic structure by elongation of the b-axis.

Discussion of the crystallography of the  $\text{B}_4\text{-}_x\text{C}_x\text{A}$  solid solutions will precede that of  $\text{B}_4\text{A}$  due to the relevance of their indexings to the  $\text{B}_4\text{A}$  structure. The pattern of the  $\text{B}_4\text{-}_x\text{C}_x\text{A}$  Type I solid solution indexed satisfactorily to an orthorhombic unit cell. The a/b axial ratio was 1.016, indicating that the symmetry of the cell is very nearly tetragonal. The Type II solid solution indexed to a monoclinic cell. This result is consistent with common inorganic phase polymorphism, where the high-temperature form typically possesses a higher symmetry than the low form.

The XRD patterns of  $\text{B}_4\text{A}$  and the Type I solid solutions bear a close resemblance to one another in terms of the distribution of the strongest reflections. However, the pattern of  $\text{B}_4\text{A}$  contains many weaker reflections not



observed in the solid solutions. A comparison of the two patterns is presented in Figure 4.13. The extra reflections suggest a cell of lower symmetry than that of the type I solid solution, and that  $\text{Ca}^{2+}$  substitution on the divalent metal ion site may result in atomic rearrangements that actually increase the crystal symmetry. However, only a single crystal XRD analysis would confirm this. No completely satisfactory indexing could be obtained for the powder pattern of  $\text{B}_4\text{A}$ , however, the gross symmetry was assumed to be orthorhombic or pseudo-orthorhombic based on the similarity of the pattern to that of the Type I form.

C. INTERPRETATION OF HEATING AND COOLING CURVES

As a result of considerable confusion surrounding the interpretation of heating and cooling curves, a critical treatment will be presented here with particular attention given to the validity of heating-curve-derived liquidus temperatures. The following discussion will refer to previous investigations (3,12,20) where the dynamic heating curve method was used to determine phase equilibrium diagrams.

In a study of the  $\text{CaO-B}_2\text{O}_3$  system, Carlson (3) used

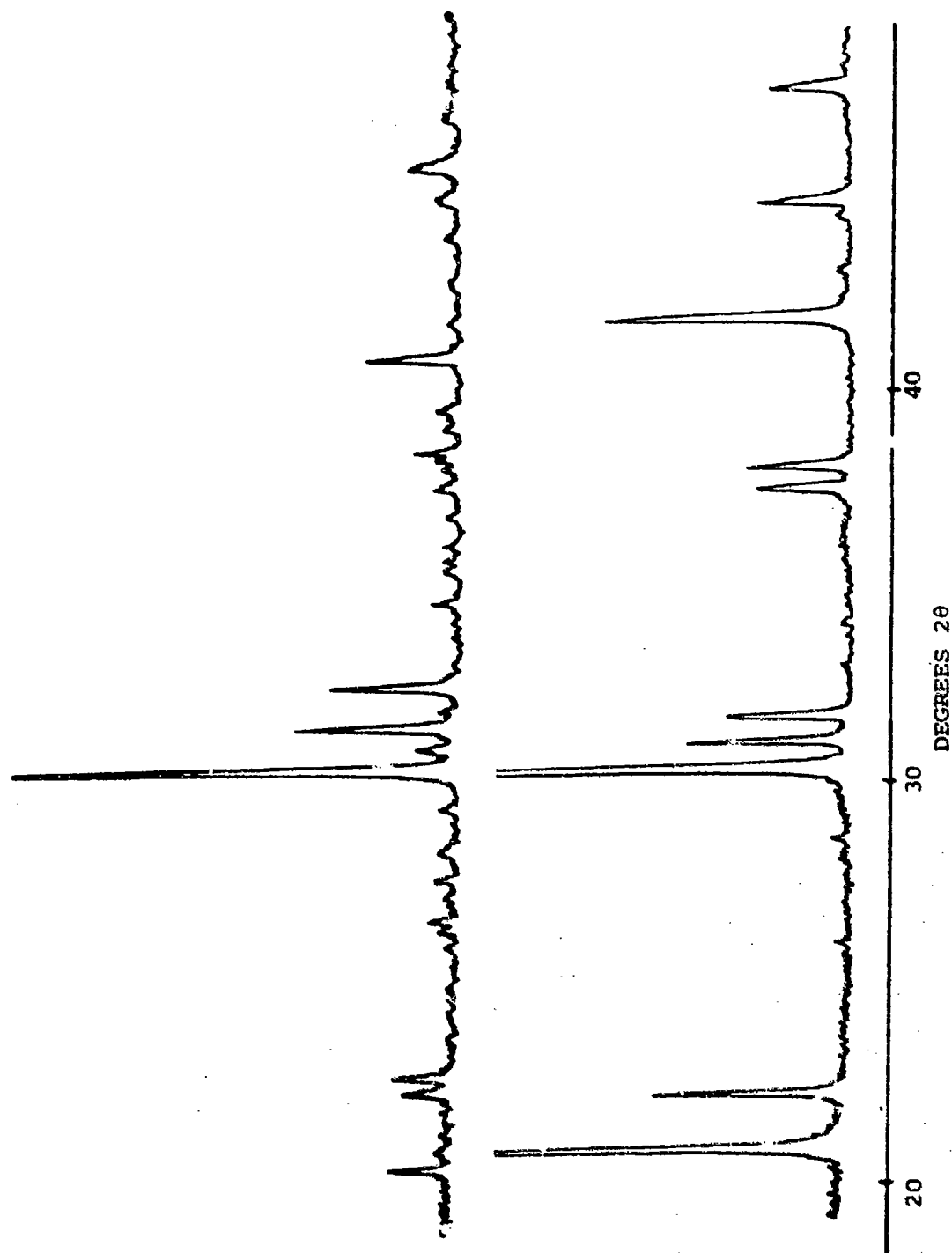


Figure 4.13. Comparison of the XRD Traces of B<sub>4</sub>A and B<sub>3.80</sub>Co<sub>0.20</sub>A.

heating curves generated by a differential thermocouple to determine the solidus and liquidus temperatures. For the curves produced by the melting of two-phase mixtures a solidus and liquidus temperature was assigned to two endothermic minimums (refer to Figure 2.1, Chapter II.) This leads the reader to believe that both events are associated with thermal arrests resulting from the interruption of heat flow to the sample thermocouple. Based on phase equilibrium theory of binary two-phase mixtures, the temperature of the sample at the solidus must remain constant until all of one solid has completely melted. No such restriction on temperature is imposed at the liquidus where the last remaining amount of the second solid is converted to liquid. Since the temperature is allowed to continuously vary through the liquidus event, no indication of an arrest should be observed. In order to confirm this, a DTA curve of the melting of a 50% lead-50% Tin mixture was obtained and is shown in Figure 4.14. It can easily be seen that, at the solidus, the interruption of heat flow from the sample to the thermocouple results in a sharp negative deviation from the DTA baseline. The difference in the onset temperature (true solidus

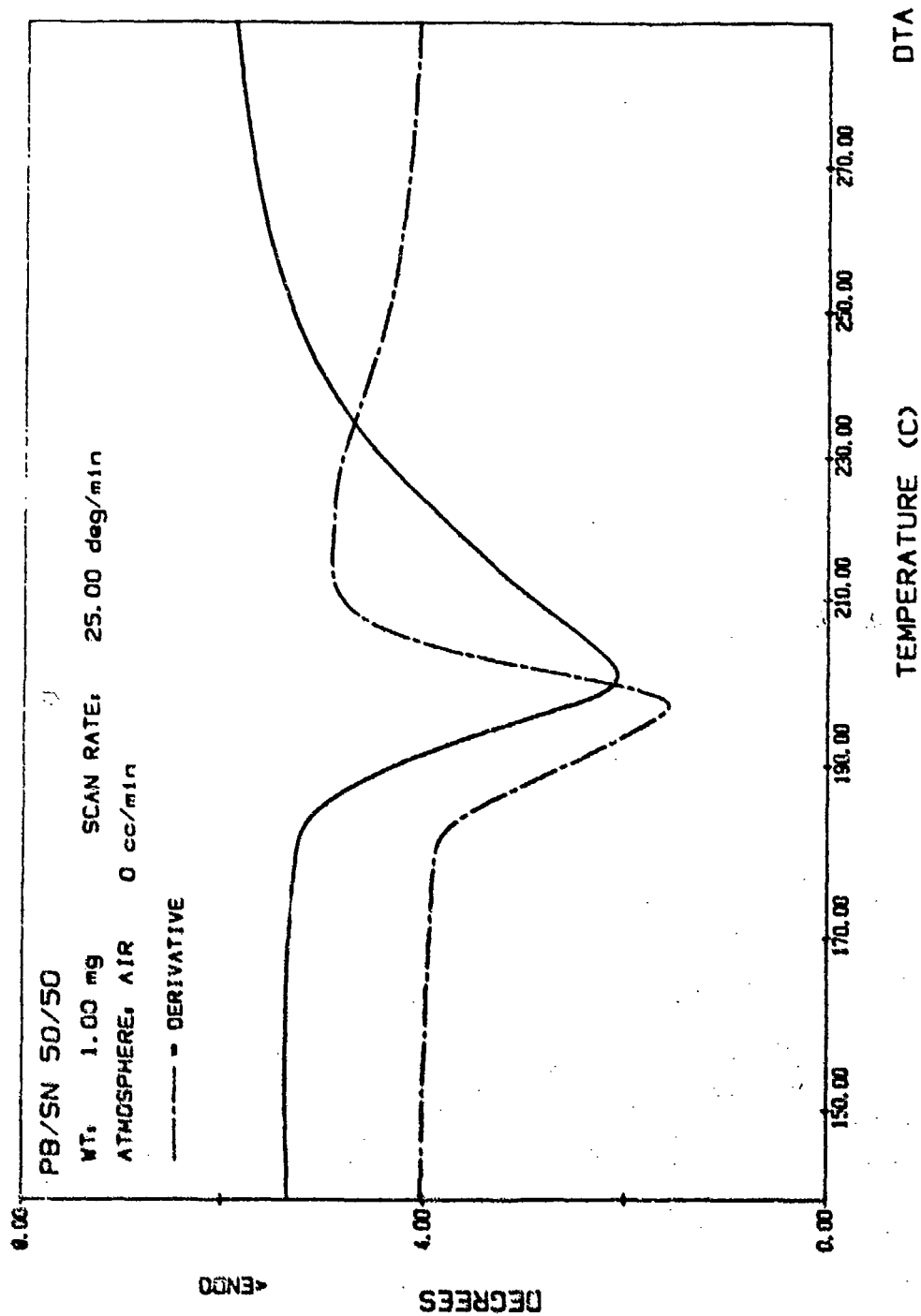


Figure 4.14. DTA Curve for a 50%Pb-50%Sn Mixture Showing Heat Effect Resulting from Melting.

temperature) and the temperature assigned to the minimum of the endotherm is caused by a thermal gradient across the sample during heating. The recovery portion of the curve is associated with the gradual conversion of the primary phase to a liquid. This portion of the curve is different in shape from the leading side in that it returns to the baseline more gradually. This is exemplified by the resulting asymmetry of the first derivative curve (dashed curve). The gradual return of trailing edge to the baseline results from the fact that some heat is required for conversion of the primary phase to a liquid. This heat requirement constantly decreases with the decreasing amount of the solid phase until the solid-to-liquid conversion is complete. At this point, all heat can then be utilized for thermal capacity of the liquid. A close approximation to the liquidus temperature would be the point where the recovery curve returns to the baseline. It can be seen that the temperature is allowed to vary continuously through the liquidus event without generating a second endothermic profile in the curve.

Based on the same reasoning, Wysni (5) and Tarter (12) presented heating curves in their respective studies

of the  $\text{CaO-Al}_2\text{O}_3$  and  $\text{BaO-CaO-Al}_2\text{O}_3$  systems which contained two thermal arrests labeled as solidus and liquidus events. It should be noted that the second arrest-like event can be attributed to other physical phenomena such as boiling. The event may not actually require an invariant situation at the boiling point for multi-component systems; however, the vigorous agitation may cause thermocouple movement and a false arrest. In comparing liquidus temperatures for several BCA compositions reported by Tarter with data obtained for the same compositions in this study (presented in the next section), it was found that his liquidus values were consistently higher (some as much as  $100^\circ\text{C}$ .) A typical heating curve obtained from melting the ternary composition  $\text{B}_3\text{C}_{.88}\text{A}$  is shown in Figure 4.15. The initial deviation from the liquidus temperature is easily observed. However, no distinct second event is featured in the curve. The point "a" on the curve is most reasonably interpreted as the point where the solidus reaction ends and heat is made available for thermal capacity. Above this point, heat is absorbed by conversion of the primary phase to a liquid and by thermal capacity of the liquid phase. Considering the rapid heating rates used to obtain curves

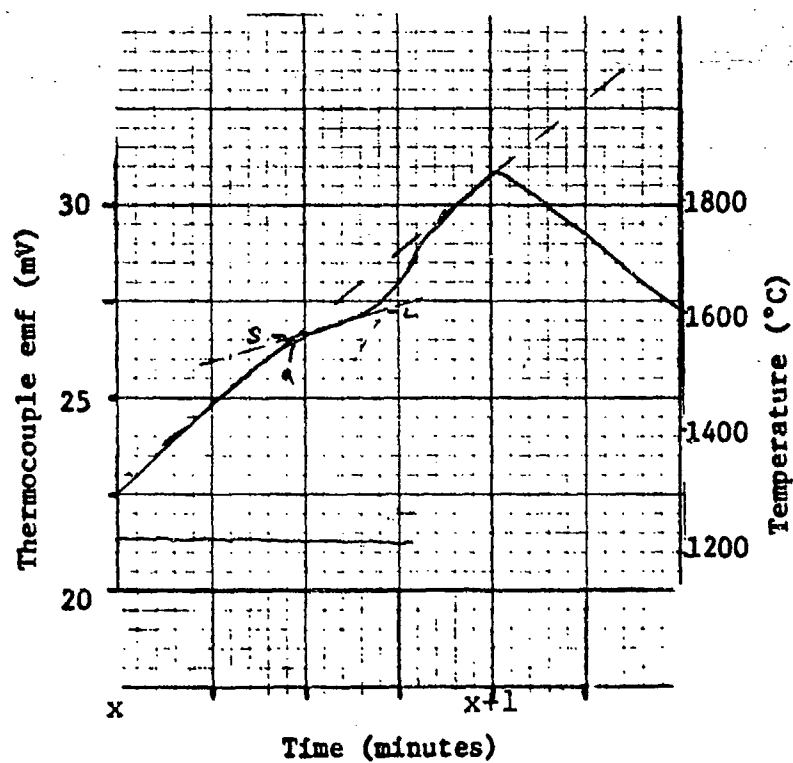


Figure 4.15. Heating Curve of  $B_{3.00}C_{0.88}A$  Showing Thermal Arrest.

with suitable arrests at the solidus ( $300-400^{\circ}\text{C}/\text{minute}$ ), the difficulty in unambiguously assigning a liquidus temperature to a point on the curve becomes readily apparent. In addition to possible existence of non-equilibrium or superheating conditions, homogeneity problems have also been observed during melting of BCA compositions. Observation of the melting process with a telescope revealed solid particles floating at the surface of the liquid. This situation leads to an error in temperature measurement due to a thermal gradient induced across the sample during rapid heating. The temperature of the liquid surface lags the temperature of the inner surface of the boat and thermocouple bead. If the liquidus were associated with an observable recorded event it would consistently be assigned a higher than actual temperature. With these limitations in mind, the validity of any liquidus temperature obtained from heating curves was considered questionable. The liquidus temperatures reported in this study were determined by visually observing the last solid to disappear at slow heating rates (approximately  $10^{\circ}\text{C}/\text{minute}$ ) and noting the thermocouple output at the time the event occurred. This



method served to minimize any thermal gradient across the sample and thus avoid non-equilibrium effects due to rapid heating. In order to determine wheather any significant gradient was present under these conditions, the temperature of the liquid surface was measured and compared to the temperature of the inner surface of the boat while constant power was being supplied to the strip. There was no observable difference in temperature. It was assumed that at the temperatures in question ( above  $1500^{\circ}\text{C}$ ), any thermal gradient induced in the sample at the slow heating rate was negligible.

The magnitude of the thermal arrest observed in the heating curves depend primarily on the amount of liquid formed at the solidus and the heat of transformation associated with the solid to liquid conversion. For a number of compositions, thermal arrests at the solidus were so weak as to be barely detectable. This was the case for many of the compositions located in solid solution regions. For these compositions, solidus temperatures were determined by visually observing slumping of the compacted pellets while heating at slow rates. Solidus temperatures determined by this method are typically higher than the

true solidus. This results from the requirement of a minimum amount of liquid needed to break down the structural integrity of the compacted pellet.

D. SOLIDUS AND LIQUIDUS TEMPERATURE DETERMINATIONS

Solidus and liquidus temperatures were determined for the BCA compositions shown in Figure 4.16. The composition points can be divided into a set of isopleths that make up four vertical planes running parallel to the temperature axis of the three dimensional prismatic volume. These planes appear as four lines in isothermal sections cut horizontally through the prism. Three planes are comprised of compositions containing 25.0, 20.0 and 15.0 mole percent  $\text{Al}_2\text{O}_3$  with variable  $\text{BaO}/\text{CaO}$  ratios, while a fourth plane extends from the compound  $\text{B}_3\text{A}$  to the  $\text{CaO}$  corner of the prism. Table 4.3 lists the solidus and liquidus temperatures for each composition. Using the solidus and liquidus measurements, a diagram containing a projection of the liquidus surface onto the  $1475^\circ\text{C}$  isothermal section was constructed and is presented in Figure 4.17. The locations of crystallization paths and primary phase fields were determined by observing discontinuities in the liquidus surface. Eutectic compositions were determined from

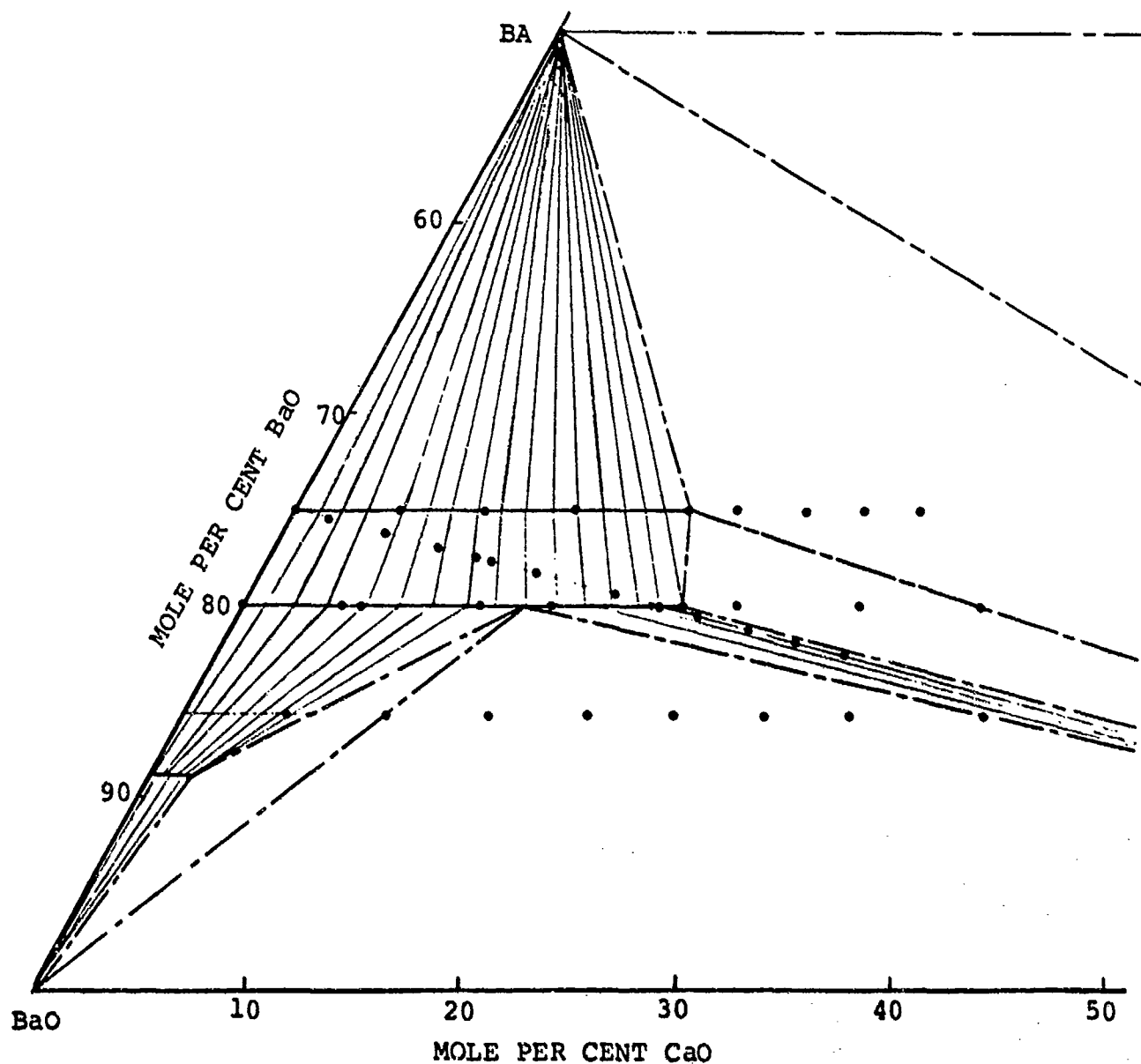


Figure 4.16. Partial Ternary Diagram of the BaO-CaO-Al<sub>2</sub>O<sub>3</sub> System Showing Location of Compositions used in Solidus/Liquidus Determinations.

Table 4.3a. Solidus and Liquidus Temperatures of Compositions along the constant 25 mole percent  $\text{Al}_2\text{O}_3$  plane.

Composition	Solidus ( $^{\circ}\text{C}$ )	Liquidus ( $^{\circ}\text{C}$ )
1	not observed	1580
2	1545	1610
3	1560	1640
4	1535	1685
5	1565	1650
6	1560	1610
7	1550	1645
8	not observed	1680
9	1550	1585

Table 4.3b. Solidus and Liquidus Temperatures along the  
B<sub>3</sub>A-CaO Psuedo-Binary.

Composition	Solidus (°C)	Liquidus (°C)
10	not observed	1602
11	1500	1625
12	1520	1635
13	not observed	1616
14	1555	1617
15	1535	1625
16	1543	1643
17	1530	1595
18	1560	1665
19	1555	1645
20	1550	1615
21	not observed	1650
22	1550	1650

Table 4.3c. Solidus and Liquidus Temperatures along the  
Constant 20 mole percent  $\text{Al}_2\text{O}_3$  Plane.

Composition	Solidus ( $^{\circ}\text{C}$ )	Liquidus ( $^{\circ}\text{C}$ )
23	not observed	1555
24	1540	1595
25	1555	1605
26	1555	1615
27	1565	1645
28	1560	1665
29	1560	1665
30	1555	1690
31	1555	1655
32	not observed	1685

Table 4.3d. Solidus and Liquidus Temperatures along the  
Constant 15 mole percent  $\text{Al}_2\text{O}_3$  Plane.

Composition	Solidus ( $^{\circ}\text{C}$ )	Liquidus ( $^{\circ}\text{C}$ )
33	not observed	1625
34	1470	1595
35	1470	1555
36	1470	1585
37	not observed	1603
38	1470	1610
39	1555	1585
40	1550	1650

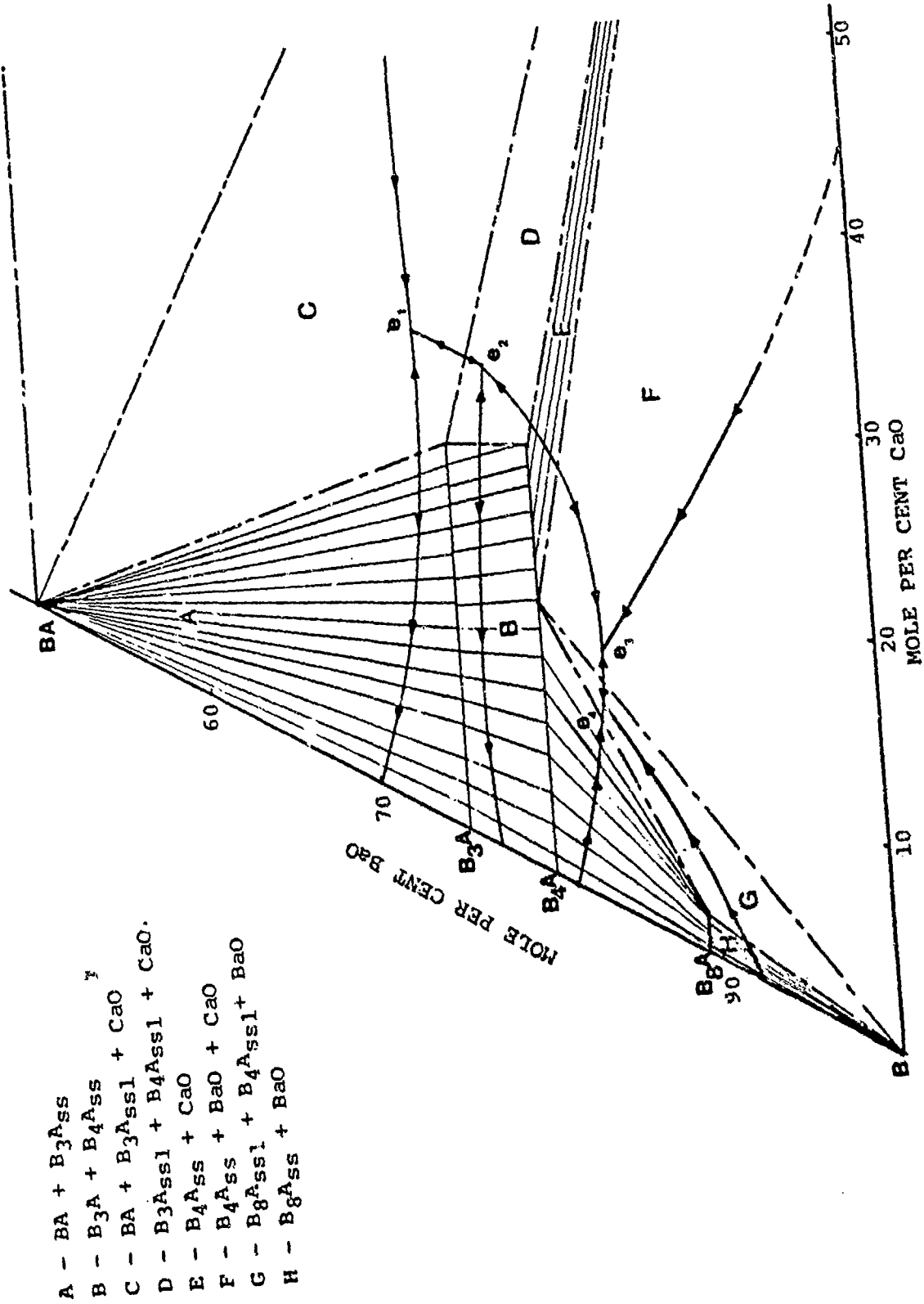


Figure 4.17. Projection of the Liquidus Surface onto the 1475 °C Isothermal Section for the High-BaO Portion of the BaO-CaO-Al<sub>2</sub>O<sub>3</sub> System.



microscopic analysis of solidified material, differences in solidus and liquidus temperatures, and the thermal slope of the liquidus surface for the various compatibility regions of the diagram. Eutectic compositions and temperatures are given in Table 4.4. The determination of the direction of falling temperature on the boundary curves projected onto solid solution two-phase regions will be discussed later.

1. Vertical Section Along the 25 Mole Percent  $\text{Al}_2\text{O}_3$  Plane

Compositions 1-9 are located along the constant 25 mole percent  $\text{Al}_2\text{O}_3$  vertical plane. This plane contains compositions comprising the  $\text{B}_3\text{A}$ -CaO solid solution series. The vertical section describing the equilibrium relationships along the constant 25 mole percent  $\text{Al}_2\text{O}_3$  plane is presented in Figure 4.18. Note that the liquidus temperature increases with increasing CaO content along the constant  $\text{Al}_2\text{O}_3$  line to a maximum of  $1660^\circ\text{C}$  at the CaO solubility limit (18.75 mole percent CaO) in  $\text{B}_{3-x}\text{C}_x\text{A}$ . A minimum in the liquidus curve occurs at the composition containing 22.5 mole percent CaO. Minima of this type indicate the intersection of the vertical section with a boundary curve separating two primary phase fields. This is illustrated in Figure 4.19 where the vertical section is

Table 4.4. Ternary Eutectic Compositions and Temperatures

$e_n$	composition	Temp ( $^{\circ}\text{C}$ )
$e_1$	$\text{B}_{1.83}\text{C}_{0.87}\text{A}$	1550
$e_2$	$\text{B}_{2.38}\text{C}_{1.05}\text{A}$	1555
$e_3$	$\text{B}_{4.32}\text{C}_{0.74}\text{A}$	1475
$e_4$	$\text{B}_{4.46}\text{C}_{0.59}\text{A}$	1475

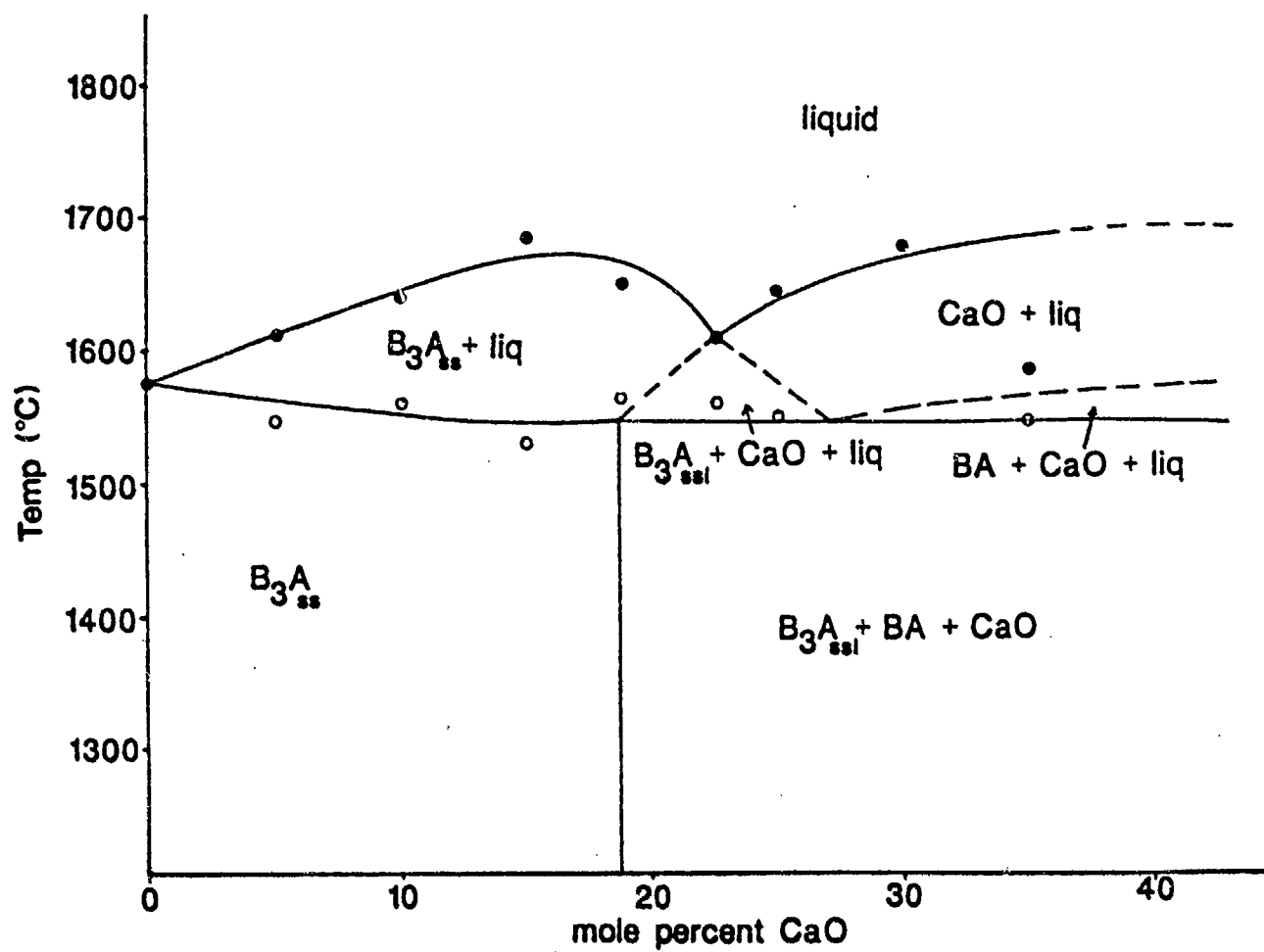


Figure 4.18. Vertical Section at the 25 Mole Percent  $\text{Al}_2\text{O}_3$  Plane.

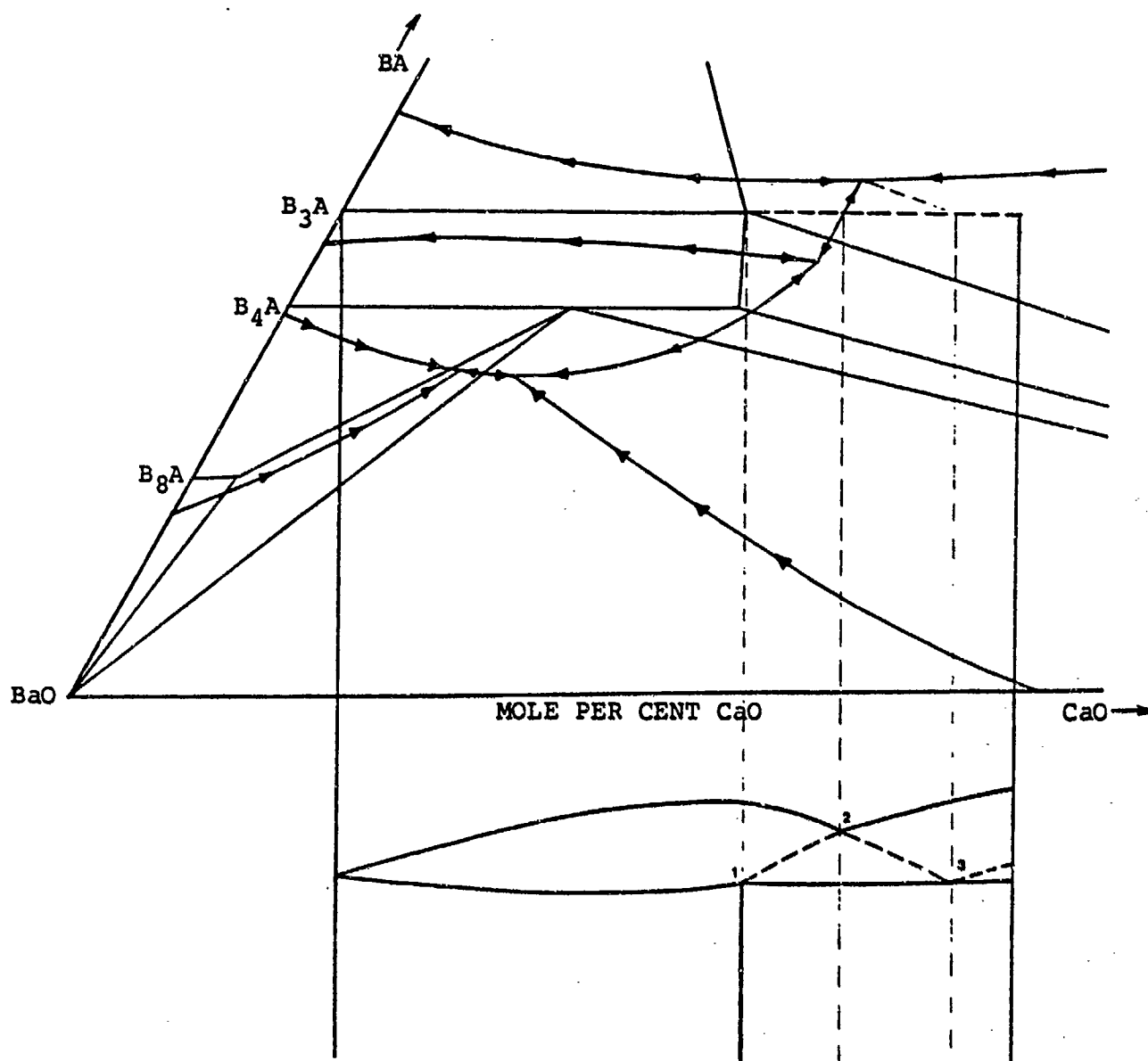


Figure 4.19. Illustration of the Relationship Between the Vertical Section at the 25 Mole Per Cent  $\text{Al}_2\text{O}_3$  Plane and the BCA Ternary Diagram.

presented in relation to the ternary liquidus surface. Isopleths associated with unique features of the vertical sections and ternary diagram are designated by number and will be used to describe various crystallization sequences presented in the following discussion. As the CaO content of the system is further increased past the minimum at 22.5 mole percent, the liquidus temperature once again gradually increases until the composition of the system reaches 30 mole percent CaO. Here a decrease in the liquidus temperature is observed. The 95° difference in liquidus temperature between Compositions 8 and 9 (30 and 35 mole percent CaO respectively) seems questionable. The low liquidus temperature observed for Composition 9 (35 mole percent CaO), could not be easily explained. It is possible that the BA-CaO boundary curve may move closer to the 25 mole percent  $Al_2O_3$  plane resulting in a flat liquidus curve along the plane. However, it is unlikely that a sharp decrease would occur. In view of this the low liquidus value measured for composition 9 was assumed to result from experimental error.

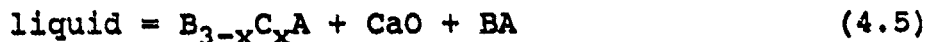
The solidus temperatures along the solid solution series exhibited some variation; although the solidus curve

had a generally flat appearance, it was assumed that the curve had a slight positive slope. The temperature of the solidus surface of the  $BA-B_{2.25}C_{0.75}A-CaO$  compatibility triangle was  $1550^{\circ}C$ .

The sub-liquidus fields in the vertical section arise from the presence of the boundary curves associated with the equilibrium crystallization of compositions located along the constant 25 mole percent  $Al_2O_3$  plane. Referring to Figure 4.19, note that , Compositions containing less than 18.75 mole percent  $CaO$  (Isopleth 1), on cooling from a melt, will first precipitate a  $B_{3-x}C_xA$  solid solution at the liquidus temperature. In the case of the  $B_{3-x}C_xA$  solid solution series, the composition of the precipitating solid solution changes continuously with decreasing temperature. No quantitative results can be obtained from the vertical section, however the positive slope of the liquidus curve suggest that on cooling from a melt, the liquid becomes depleted of  $CaO$  with decreasing temperature and that the last solid solution to crystallize is richest in  $CaO$ .

The compositions containing between 18.75 (Isopleth 1) and 22.5 mole percent  $CaO$  (Isopleth 2),

located along the constant 25 mole percent  $\text{Al}_2\text{O}_3$  plane, are also located within the  $\text{B}_3\text{A}$  primary phase field. However, these compositions consist of a three-phase assemblage upon completion of equilibrium crystallization. The portion of the vertical section associated with these compositions features a sub-liquidus boundary, indicated by a dashed line, separating the  $\text{B}_3\text{A}$  primary phase field and a field containing  $\text{B}_{3-x}\text{C}_x\text{A}$  solid solution,  $\text{CaO}$  and liquid. For any isopleth in this compositional region, the intersecting point on the sub-liquidus boundary indicates the temperature at which the liquid composition reaches the  $\text{B}_3\text{A}$ - $\text{CaO}$  boundary curve and marks the beginning of the simultaneous crystallization of  $\text{CaO}$  and  $\text{B}_{3-x}\text{C}_x\text{A}$ . At the solidus temperature, the liquid composition has reached the eutectic composition and the eutectic reaction,



proceeds until all the liquid has converted to the solid state.

A similar situation occurs on the right side of the  $\text{B}_3\text{A}$ - $\text{CaO}$  boundary curve (Isopleth 2) between 22.5 and 29.0 mole percent  $\text{CaO}$  (Isopleth 3), except that  $\text{CaO}$  is the

primary phase in the crystallization sequence. The composition Isopleth 2 intersecting the liquidus at the minimum located at 22.5 mole percent CaO would exhibit simultaneous crystallization of  $B_{3-x}C_xA$  and CaO at the liquidus temperature. This is due to the fact that this isopleth directly intersects the  $B_3A$ -CaO boundary curve.

The point at which the  $B_{3-x}C_xA$ -CaO sub-liquidus boundary intersects the solidus curve occurs at a composition that is located on the line connecting the  $B_3$ - $x$  $C_xA$ -CaO-BA eutectic composition and the CaO phase corner. This is illustrated by Isopleth 3 in Figure 4.19. The first solid to crystallize from the melt for this composition is CaO. The liquid composition travels across the CaO primary phase field directly toward the ternary eutectic,  $e_1$ , as the temperature decreases and does not intersect a boundary curve during the entire crystallization sequence. At the solidus temperature the liquid composition reaches the eutectic composition and final crystallization occurs according to reaction 4.5. Compositions containing more than 29 mole percent CaO will encounter a sub-liquidus field containing CaO, BA and liquid. This field is associated with the BA-CaO boundary



curve.

2. Vertical Section at 20 Mole Percent  $\text{Al}_2\text{O}_3$

The liquidus and solidus temperatures of compositions located along the constant 20 mole percent  $\text{Al}_2\text{O}_3$  plane (compositions 24 through 34) are presented in the form of a vertical section in Figure 4.20. The relationship of the vertical section with the ternary liquidus surface is shown in Figure 4.21. The end member of this vertical section is the compound  $\text{B}_4\text{A}$ . Lambert (1) suggested that  $\text{B}_4\text{A}$  melted incongruently to form a liquid and a higher-BaO compound (most likely  $\text{B}_8\text{A}$  or  $\text{B}_{10}\text{A}$ ). Her conclusion was based on the absence of a minimum in the liquidus curve between  $\text{B}_4\text{A}$  and BaO. However, if the eutectic composition is very near that of  $\text{B}_4\text{A}$ , then the slight depression in the liquidus curve could have easily been overlooked.

In this study a further attempt was made to characterize the melting behavior of  $\text{B}_4\text{A}$ . Samples of  $\text{B}_4\text{A}$  were completely fused at  $1650^\circ\text{C}$  and then rapidly quenched to room temperature. Petrographic and XRD analyses were performed on the fusion products to determine the resulting phase assemblage. The petrographic analysis indicated that

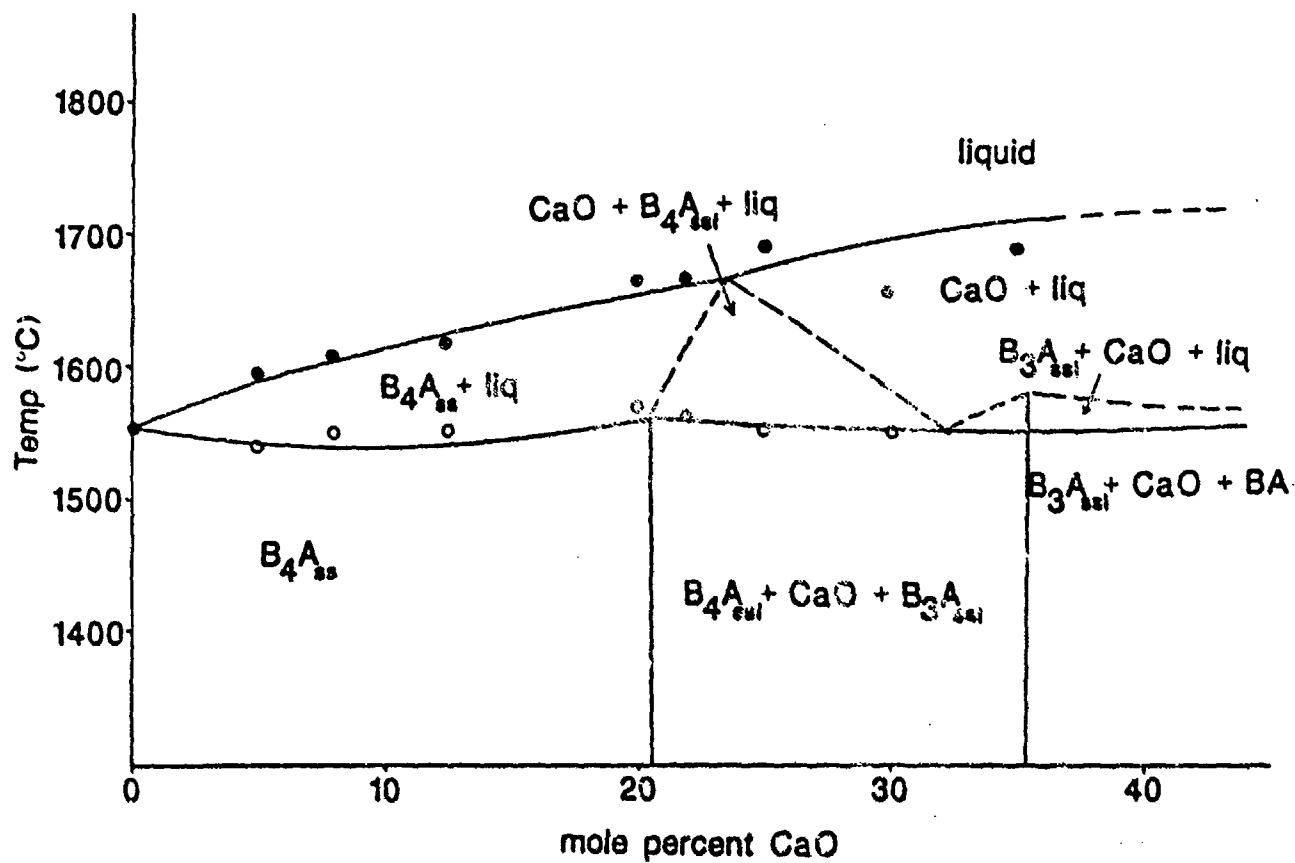


Figure 4.20. Vertical Section at the 20 Mole Percent  $\text{Al}_2\text{O}_3$  Plane.

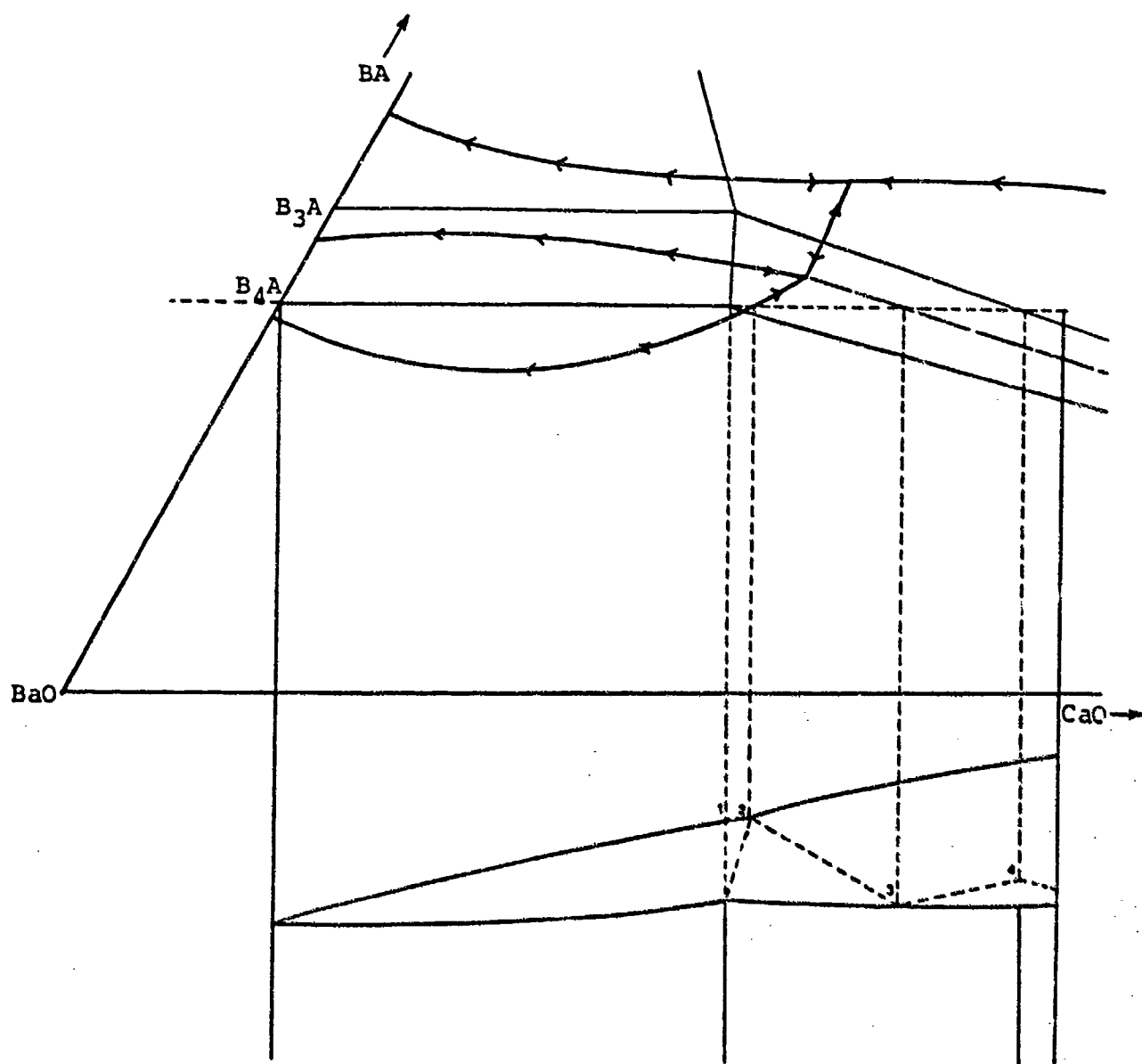


Figure 4.21. Illustration of the Relationship Between the Vertical Section at the 25 Mole Per Cent  $Al_2O_3$  Plane and the BCA Ternary Diagram.

only biaxial positive crystals (characteristic of pure  $B_4A$ ) were present in the melted material. The XRD analysis of the sample also supported the conclusion that the fusion product contained only pure  $B_4A$ . If  $B_4A$  melted incongruently, it is unlikely that the rapid quenching of the melt to room temperature would have allowed the high-BaO primary phase to react completely with the liquid to form  $B_4A$ , thus some of the high-BaO phase should have been observed in the fused material. Since no high-BaO phase was found, the compound  $B_4A$  was concluded to melt congruently. This method is commonly used for determining melting behavior of compounds and has even been successfully used in non-glass forming systems with highly fluid liquids (5). The revised portion of BaO- $Al_2O_3$  system containing  $B_4A$  is presented in Figure 4.22.

It is evident from the vertical section that substitution of  $Ca^{2+}$  for  $Ba^{2+}$  in the  $B_{4-x}C_xA$  structure results in an increase in the liquidus temperature. At 22 mole percent CaO (Isopleth 2) a shallow discontinuity is featured in the liquidus curve. This discontinuity in the liquidus temperature was associated with the intersection of the vertical section with the boundary curve separating

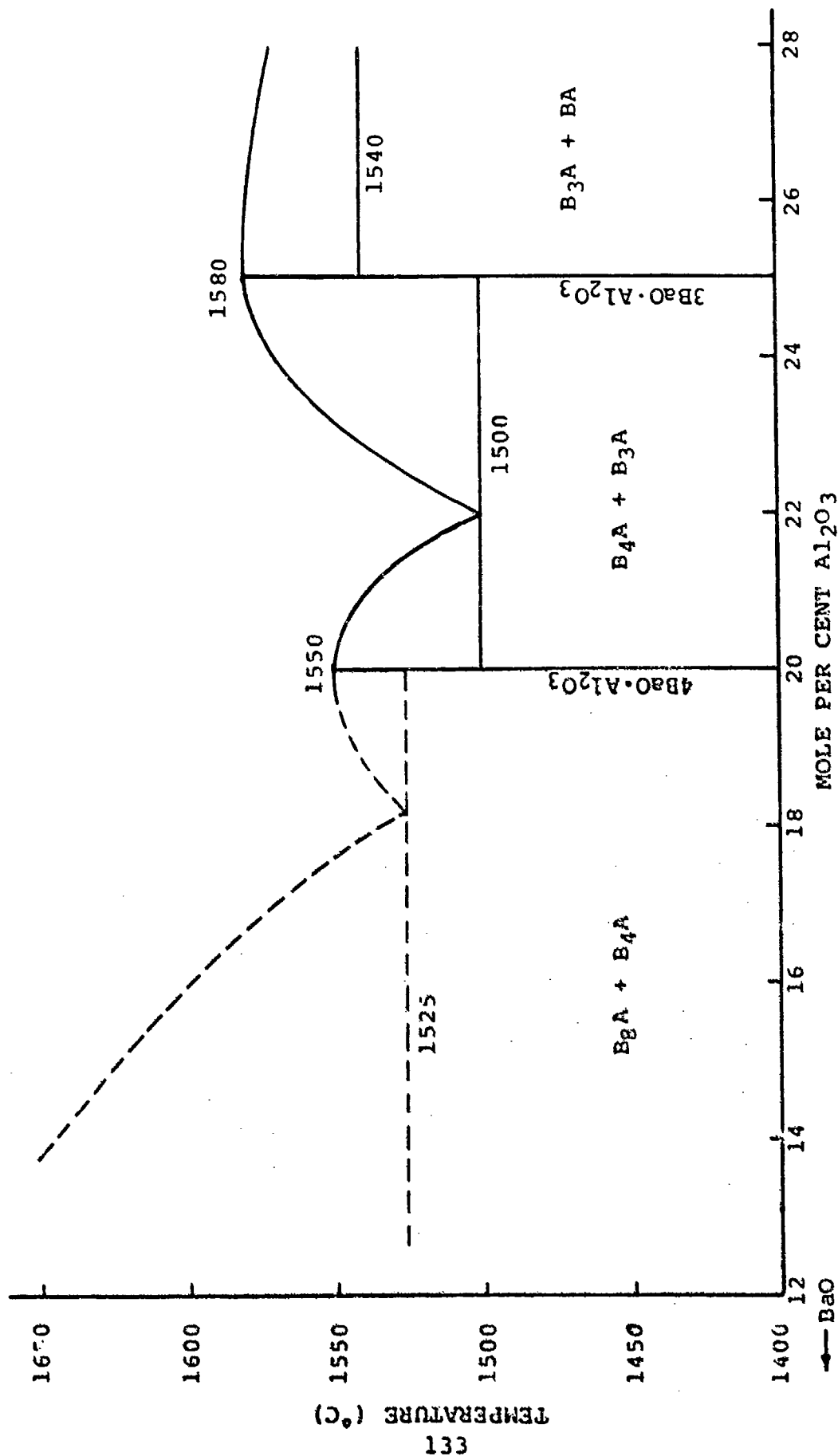
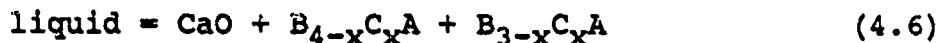


Figure 4.22. Revised portion of the BaO-Al<sub>2</sub>O<sub>3</sub> Diagram, Showing the Congruently Melting Compound B<sub>4</sub>A.

the primary phase fields of  $B_4A$  and  $CaO$ . Although the presence of the discontinuity is not strongly indicated by the liquidus data its existence and location is supported by microscopic analyses which will be discussed in a later section. The sub-liquidus boundary separating the  $CaO$  primary phase field and a field containing  $CaO$ ,  $B_{4-x}C_xA$  and liquid is shown as a dashed line for the portion of the system containing more than 22 mole percent  $CaO$ . Points along this boundary represent the temperature at which  $B_{4-x}C_xA$  and  $CaO$  begin to crystallize simultaneously from the liquid. Below this temperature crystallization of the two solids proceeds and the liquid composition moves along the  $B_4A$ - $CaO$  boundary curve toward the eutectic composition  $e_2$ . As shown in Figure 4.21, the minimum in the sub-liquidus boundary along the 20 mole percent  $Al_2O_3$  plane occurs at Isopleth 3 located on the line connecting the ternary eutectic composition and the  $CaO$  corner. Crystallization for this isopleth involves precipitation of  $CaO$  as the primary phase while the liquid composition moves directly toward the ternary eutectic  $e_2$ . Past this point, the crystallization sequence involves the  $B_3A$ - $CaO$  boundary curve and the resulting sub-liquidus boundary shown in the

vertical section which partitions the field containing CaO,  $B_{3-x}C_xA$  and liquid from the CaO primary phase field. At the eutectic temperature, 1555°C, the reaction,



occurs for all compositions located between 21 and 35 mole percent CaO and proceeds until all liquid is converted to the solid-state phase assemblage. The sub-liquidus maximum occurring at 35 mole percent CaO (Isopleth 4) results from the intersection of the  $B_3A$ -CaO boundary curve with the  $B_{3-x}C_xA_{\text{ss1}}$ -CaO Alkemade line. The final phase assemblage for crystallization along this isopleth would consist of  $B_3A_{\text{ss1}}$  and CaO. Also shown in the vertical section is the proposed location of the two-phase region containing the Type I and Type II polymorphs of the  $B_{4-x}C_xA$  solid solution series.

### 3. Vertical Section From $B_3A$ to CaO

The vertical section containing compositions lying along a line extending from  $B_3A$  to CaO is shown in Figure 4.23. Figure 4.24 shows the crystallization sequences for several isopleths located along this section with respect to the ternary diagram. As CaO is added to the system, a

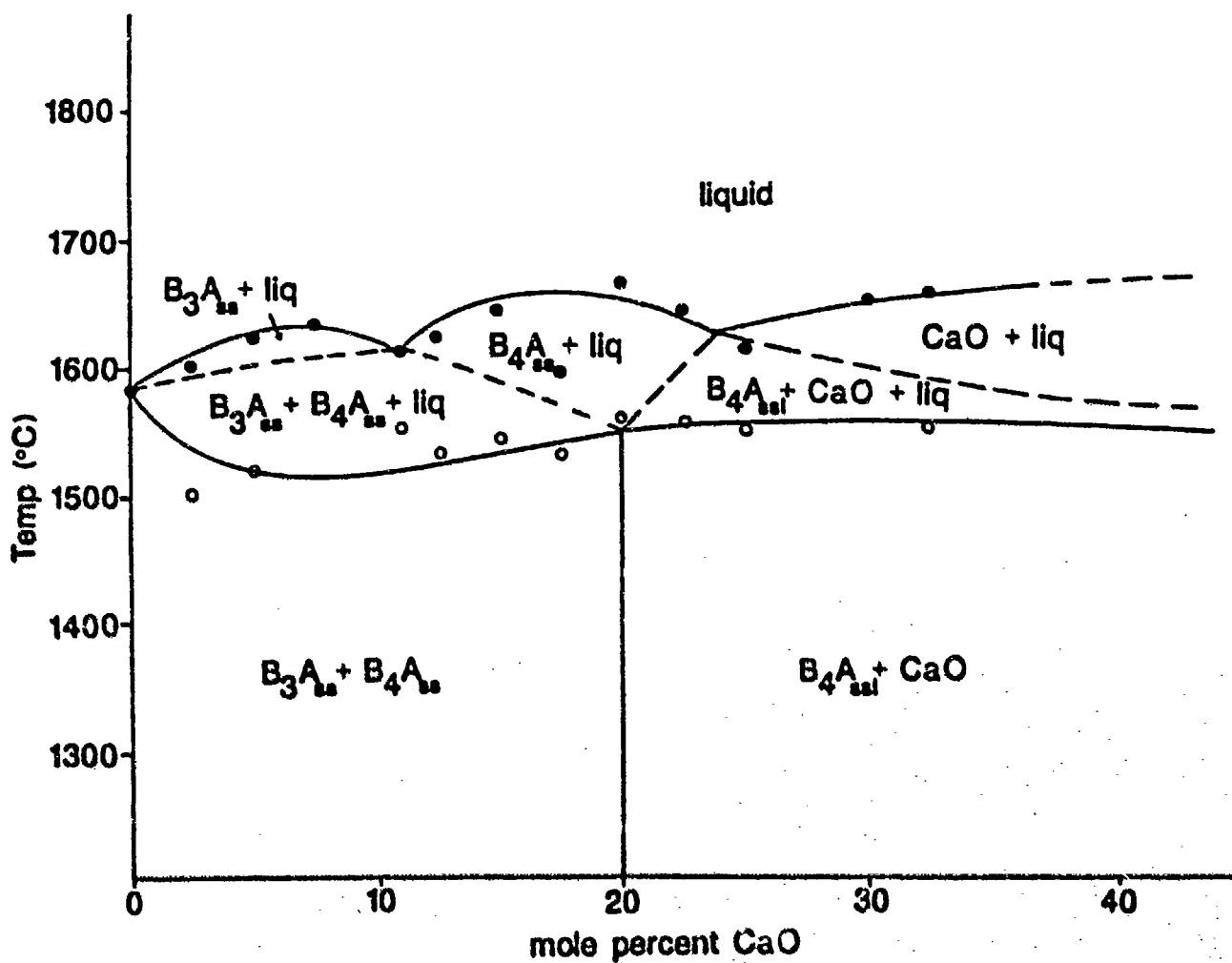
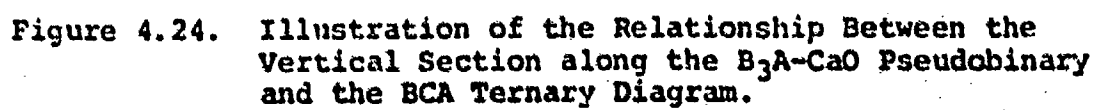


Figure 4.23. Vertical Section Along the  $B_3A$ - $CaO$  Pseudo-binary.





series of liquidus maxima and minima occur. The first minimum, located at 10.5 mole percent CaO (Isopleth 1), results from the intersection of the vertical section with the  $B_3A$ - $B_4A$  boundary curve that extends from the  $B_4A$ - $B_3A$  binary eutectic. This boundary curve separates the primary phase fields of  $B_3A$  and  $B_4A$  and can be projected onto the full length of the  $B_{3-x}C_xA$ - $B_{4-x}C_xA$  two-phase sub-solidus compatibility region. It should be noted from the ternary diagram that the direction of falling temperature along this length of the boundary curve is toward the binary eutectic. This type of characteristic is possible in ternary systems which exhibit solid solubility with one or more of the components.

The second liquidus minimum (Isopleth 3) occurs as a result of the intersection of the vertical section with the  $B_{4-x}C_xA$ -CaO boundary curve. The liquidus maxima occur as a result of the geometry from which the vertical section intersects the liquidus surface between the two substitutional solid solutions. For compositions containing more than 25 mole percent CaO, the liquidus temperature again begins to increase as the composition of the system extends farther into the CaO primary phase

field.

Two sub-liquidus fields are shown in the vertical section. The first sub-liquidus field contains  $B_{3-x}C_xA$ ,  $B_{4-x}C_xA$  and liquid. The boundaries were derived from the crystallization sequences occurring along the  $B_3A$ - $B_4A$  boundary curve, using the same principles described for the previous vertical sections. All compositions located between  $B_3A$  and point Isopleth 1 along the vertical section will first precipitate  $B_{3-x}C_xA$  as the primary phase. As the crystallization reaches the  $B_3A$ - $B_4A$  boundary curve, simultaneous crystallization of  $B_{3-x}C_xA$  and  $B_{4-x}C_xA$  occurs. At the point where the system temperature reaches the solidus, the reaction,



proceeds to completion, with the composition of the liquid and both solids continuously changing until all of the liquid has been depleted. As a result of the final two-phase solid solution assemblage, no eutectic reaction is involved in the sequence. Since the direction of falling temperature along the boundary curve is toward the binary eutectic, the CaO content of the liquid decreases with

decreasing temperature. Compositions located between Isopleths 1 and 3 crystallize in a similar manner, with the exception that  $B_{4-x}C_xA$  is the primary phase instead of  $B_{3-x}C_xA$ .

Isopleth 1 does not exhibit primary phase crystallization as a result of its location directly on the  $B_3A$ - $B_4A$  boundary curve. As the liquid is cooled, crystallization commences with nucleation and growth of both solid solution phases and then proceeds according to reaction 4.7. Isopleth 2 corresponds to the intersection of the vertical cut with the  $B_4A$ -CaO solid solution series. Since the crystallization phenomenon for this composition is that of a single-phase solid solution, no sub-liquidus fields are involved in the sequence. The solid solution formed after complete solidification has the formula  $B_3CA$ , and is represented by a single line in the sub-solidus portion of the vertical section.

The remaining sub-liquidus field in the section indicates the crystallization of  $B_{4-x}C_xA$  and CaO along the  $B_{4-x}C_xA$ -CaO boundary curve for compositions located in either the  $B_4A$  or CaO primary phase fields. All compositions in the vertical section that contain more than

20 mole percent CaO (Isopleth 2) will undergo the reaction,



at the solidus temperature, 1555°C, and the final liquid composition will be located on the B<sub>4</sub>A-CaO boundary curve projected onto the B<sub>4-x</sub>C<sub>x</sub>A-CaO compatibility region. The sharp depression in the solidus temperature between one and 2.5 mole percent CaO results from the close proximity of this region to the B<sub>3</sub>a-B<sub>4</sub>A binary eutectic.

#### 4. Vertical Section at 15 Mole Percent Al<sub>2</sub>O<sub>3</sub>

The vertical section containing compositions along the constant 15 mole percent Al<sub>2</sub>O<sub>3</sub> plane is shown in Figure 4.25 and its relation to the ternary diagram is illustrated in Figure 4.26. Two liquidus minima are featured in the vertical section. The first at Isopleth 1 was ascribed to the B<sub>8</sub>A-BaO boundary curve and the second (Isopleth 6) results from the intersection of the plane with the BaO-CaO boundary curve. It should be noted that the first liquidus minimum was not clearly defined from the liquidus data and that all features located to the left of Isopleth 3 should be considered only tentative. It is evident in the ternary diagram that the vertical section traverses two sub-solidus

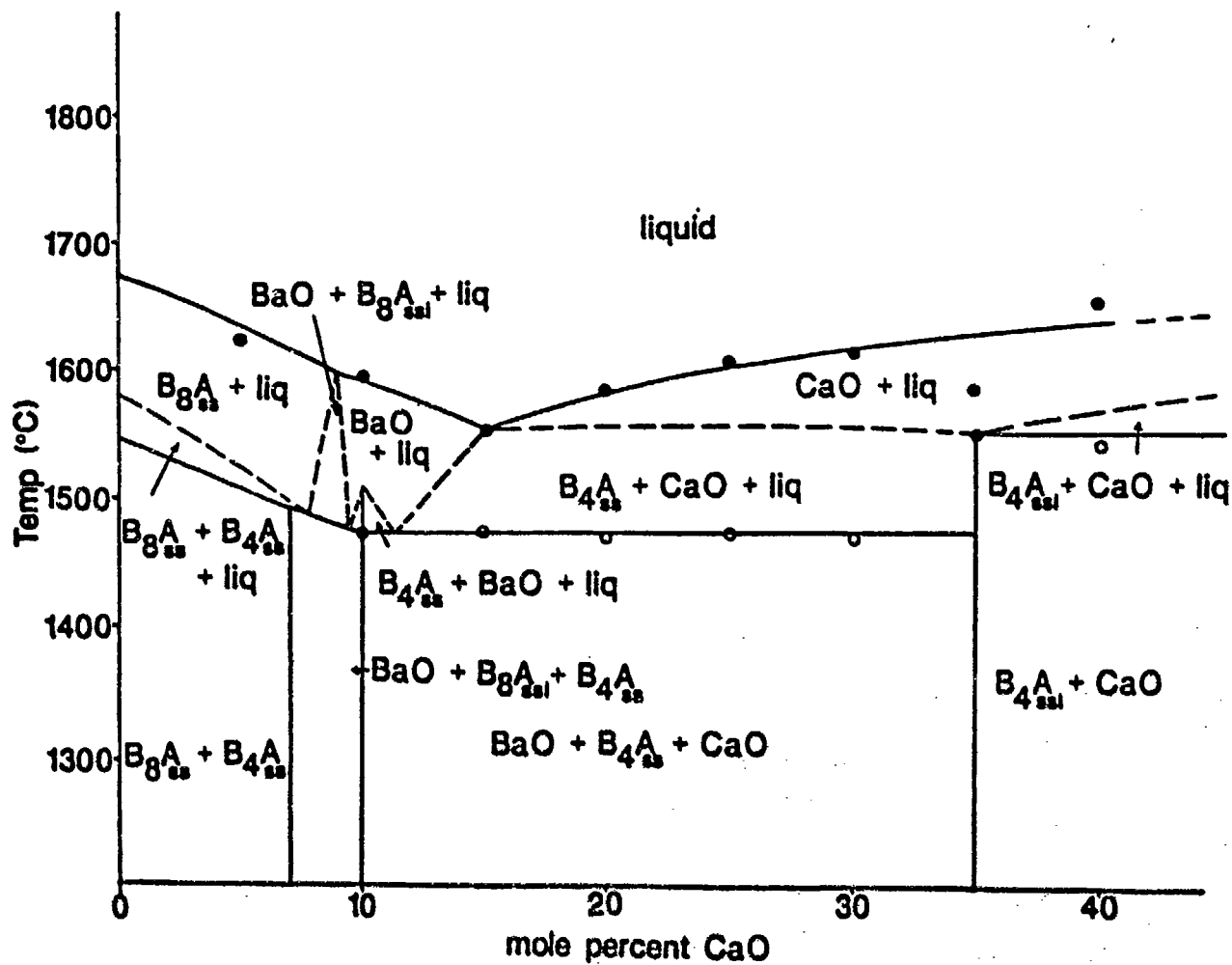


Figure 4.25. Vertical Section at the 15 Mole Percent  $\text{Al}_2\text{O}_3$  Plane.

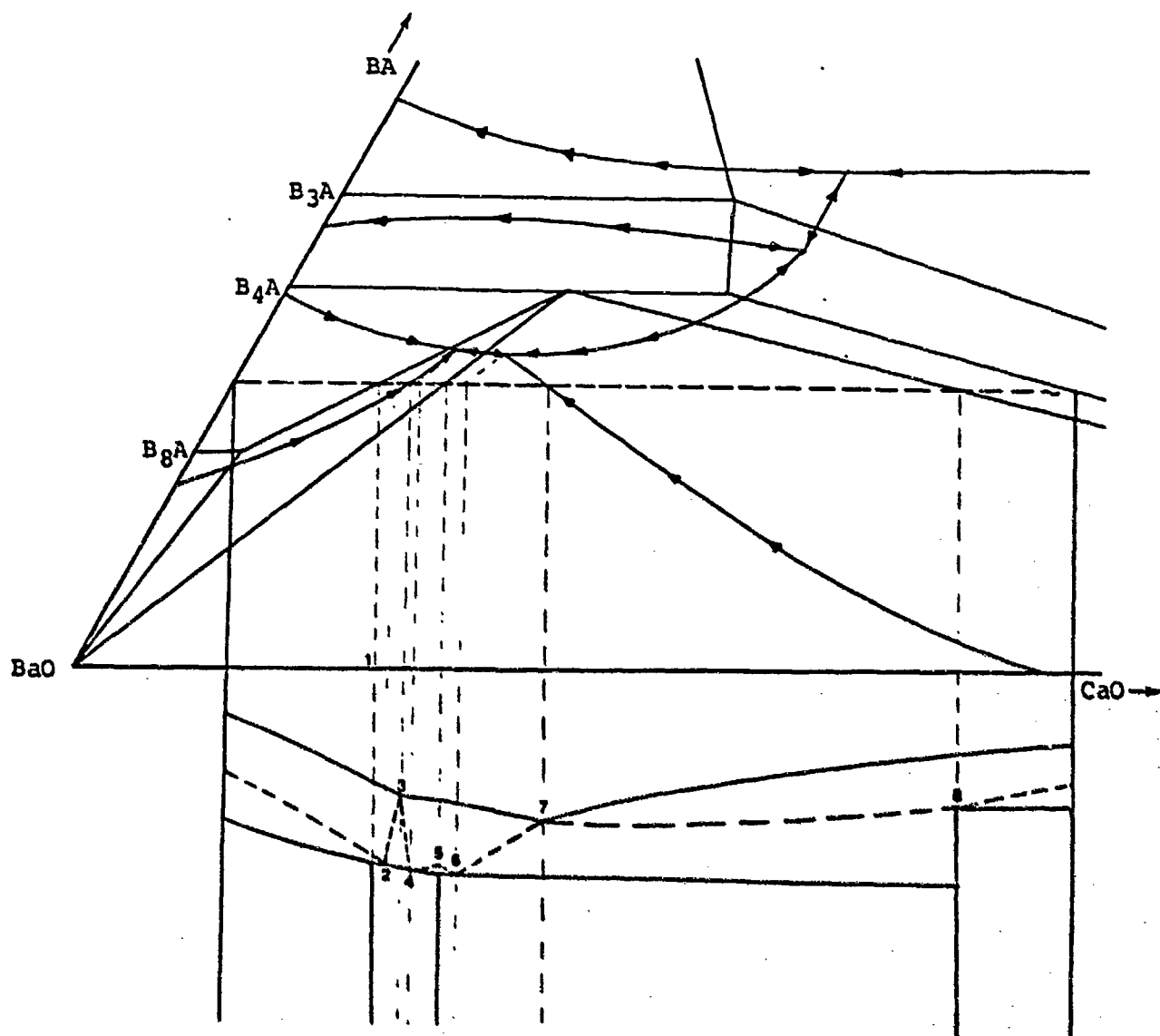
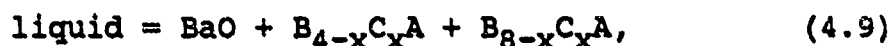


Figure 4.26. Illustration of the Relationship Between the Vertical Section at the 15 Mole Per Cent  $Al_2O_3$  Plane and the BCA Ternary Diagram.

compatibility regions containing the compound  $B_8A$  and its calcium substitutional solid solutions. In order to comply with this sub-solidus configuration, two sub-liquidus fields containing  $B_{8-x}C_xA$  solid solutions are proposed in the vertical section. The existence of the  $B_{4-x}C_xA$ - $B_{8-x}C_xA$ - $BaO$  compatibility triangle in the  $1475^\circ C$  isothermal section requires the presence of an associated peritectic or eutectic invariant point. On this basis, final crystallization in this triangle was assumed to occur according to the reaction,



and the corresponding eutectic,  $e_4$ , was included in the ternary diagram. Solidus temperatures along the vertical section range from  $1470^\circ$  to  $1555^\circ C$ . As mentioned earlier in the section on sub-solidus equilibria, a discontinuity was observed in the solidus curve at 30 mole percent  $CaO$  (Isopleth 7.) This was interpreted as the intersection of the vertical section with the  $B_{4-x}C_xA$ - $CaO$  Alkemade line.

The  $B_8A$  primary phase field was found to extend from zero to 8.5 mole percent  $CaO$  (Isopleth 2.) The  $BaO$  primary phase field is located between 8.5 (Isopleth 2) and



15 mole percent CaO (Isopleth 6.) The maximum in the  $B_4$ -BaO sub-liquidus field occurring at Isopleth 4 results from the intersection of the  $B_4A$ -BaO boundary curve with the  $B_4$ - $xC_xA$ -BaO Alkemade line. The sub-liquidus minima located at Isopleths 3 and 5 occur as a result of the direct travel of the liquid compositions across the BaO primary phase field to their respective eutectic compositions.

#### E. CRYSTALLIZATION AND MICROSTRUCTURE

Scanning electron microscopy and Energy-dispersive X-ray spectrometry of re-solidified compositions were used to firmly establish the location of the CaO primary phase field. A scanning electron micrograph of a polished section of  $B_5C_3A_2$  is shown in Figure 4.27. EDS analysis revealed that the primary phase dendrite was composed of essentially pure CaO. The surrounding matrix phase was found to contain barium, calcium and aluminum. A comparison of the X-ray spectra of the two areas is presented in Figure 4.28. It was determined from liquidus temperatures along the constant 20 mole percent  $Al_2O_3$  plane that the  $B_4A$ -CaO boundary curve intersected the plane at approximately 22 mole percent CaO. Compositions along the plane having CaO contents greater than 22 mole percent

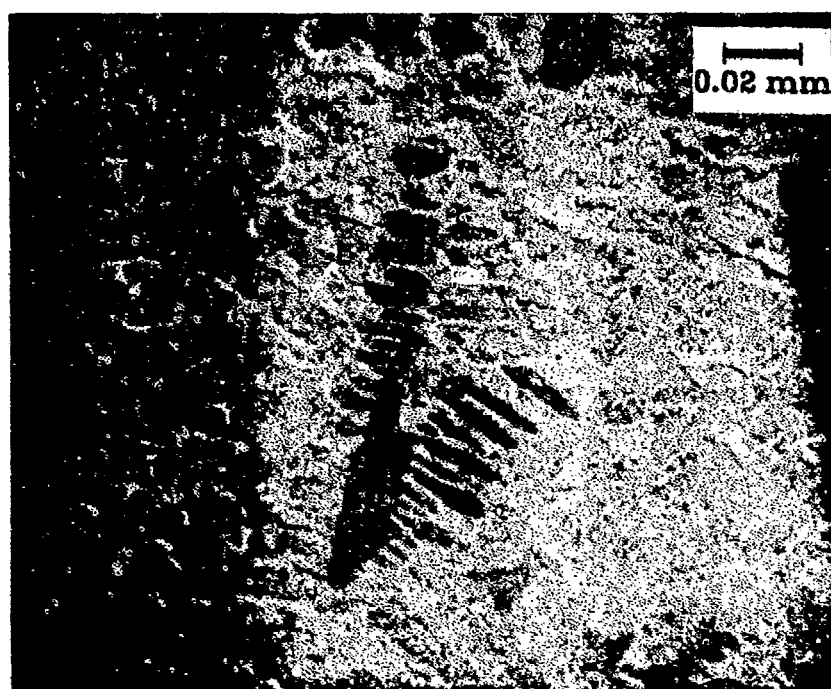


Figure 4.27. Scanning Electron Micrograph of a Polished Section of  $B_5C_3A_2$ .

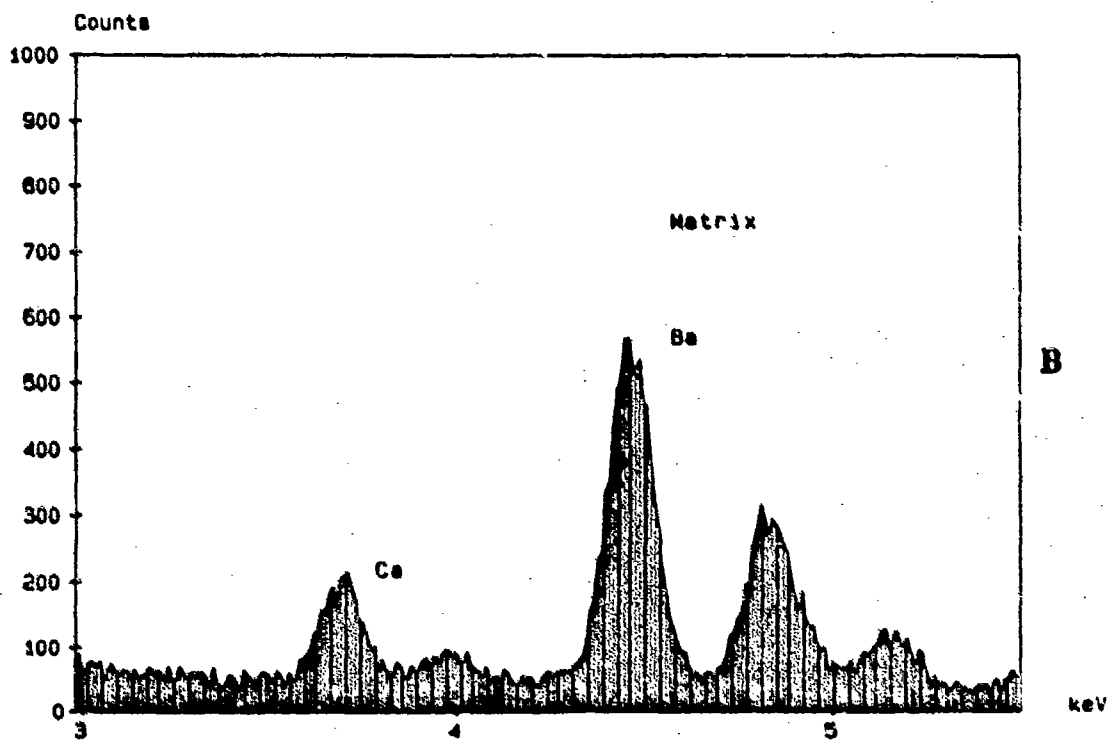
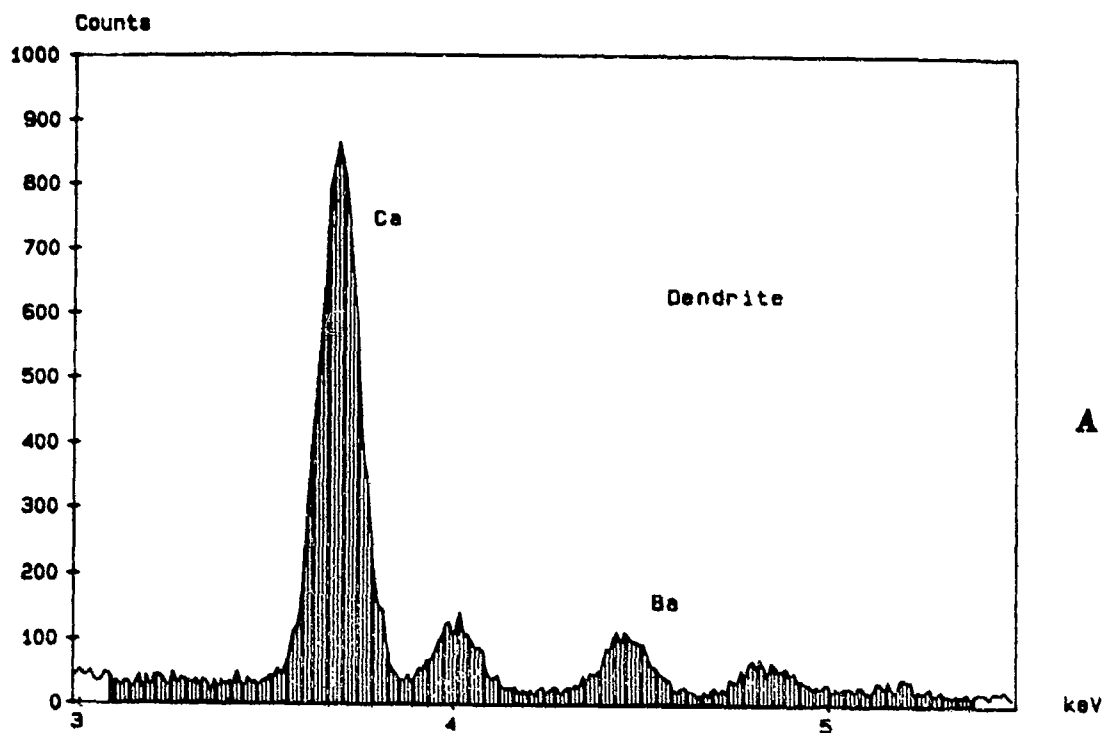


Figure 4.28. EDS Spectra of (a) Dendrite and (b) Matrix Region of the Polished Section of  $B_{2.75}C_{1.25}A$ .

would be expected to reside in the CaO primary phase field. The presence of the CaO primary phase dendrite in the polished section of  $B_5C_3A_2$  supports this conclusion and confirms the location of the boundary curve. In the scanning electron micrograph of a polished section of  $B_5C_3A_2$ , high-baria areas (as determined by quantitative EDS analysis) appear rough, whereas the smooth three-phase matrix did not significantly hydrate. According to the phase diagram, simultaneous crystallization of the limit solid solution of  $B_{4-x}C_xA_{ss1}$  and CaO will occur when the liquid composition reaches the  $B_4A$ -CaO boundary curve. If nucleation and growth of these two phases occur at a common point, isolated two-phase region would be expected to exist in the microstructure. This is the most probable phase assemblage of the rough regions on the polished section. These regions would also possess the highest baria content, since the three-phase matrix region will contain the limit solid solution of  $B_{3-x}C_xA$ . This crystallization sequence is consistent with both the microstructure and the quantitative EDS analysis for the  $B_5C_3A_2$  polished section.

A microscopic analysis was also used to confirm

the location of the ternary eutectic,  $e_1$ . A sample of  $B_2CA$  was prepared by slowly cooling the melt from above the liquidus until complete solidification had occurred. A polished section of the sample (Figure 4.29) revealed a microstructure containing aligned lamellae in a continuous matrix. This type of structure is characteristic of solidified eutectic or slightly off-eutectic mixtures.

F. MELTING POINT DETERMINATION OF BARIUM OXIDE

In determining the melting point of  $BaO$  by in situ oxidation of barium metal, both visual confirmation and thermal analysis heating curves were used. During heating, no liquid formation was observed at the  $BaO-BaCO_3$  eutectic temperature,  $1030^\circ C$ . The liquid associated with this eutectic is very reactive and usually results in contamination which would typically depress the melting temperature of the sample below the true melting point of pure  $BaO$ . This liquid was observed by Schumacher (7) in his determination of the melting point of carbonate-derived  $BaO$ .

The heating curve generated in this determination is presented in Figure 4.30. The thermal arrest associated with the melting event occurred at  $2250^\circ C$ . A hump

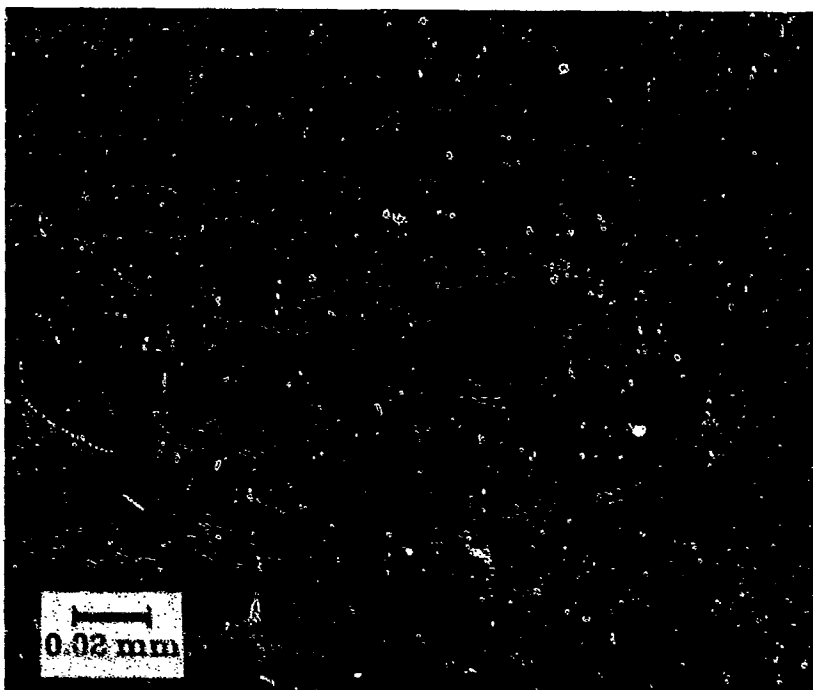


Figure 4.29. Reflecting Light Micrograph of a Polished Section of  $B_2CA$ .

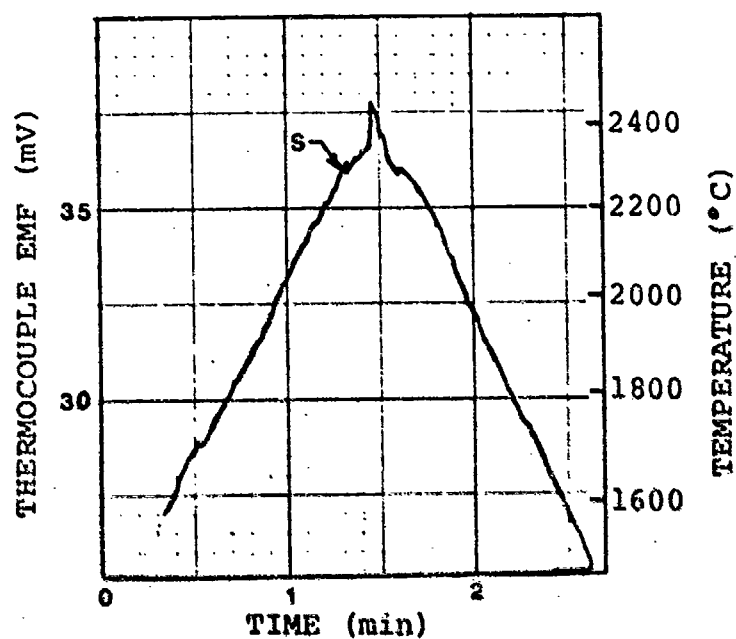


Figure 4.30. Heating Curve of BaO from In-situ Oxidation of Barium Metal.

characteristic of heat evolution from a dynamically supercooled liquid was observed in the cooling curve, confirming the validity of the melting event. Visual confirmation of liquid formation at this temperature was also established. The melting point determined by this method was  $335^{\circ}$  higher than that reported by Schumacher, which suggests that less contamination was present in the sample melted in this study.

G. CALCULATION OF THE BaO-CaO BINARY DIAGRAM

In view of the formidable experimental difficulties associated with very-high-BaO compositions, no BaO-CaO binary phase diagram exists in the literature. In order to better understand the uninvestigated portion of the system, a calculated binary diagram was developed from molal freezing point depression theory. The accuracy of calculated phase diagrams depends primarily on the amount of solid solubility present in the system and the magnitude of the deviation from ideality of the liquid with respect to the two components. Since solid solubility between the two components has been reported to be negligible for temperatures up to  $1100^{\circ}\text{C}$ , and since there is apparently no compound formation in the system, one would expect the BaO-



CaO binary system to be a good candidate for yielding a valid calculated diagram.

The liquidus curves were generated by the equations,

$$T = T_A + (RT_A^2 / H_A) \ln(1 - X_B) \quad (4.10)$$

$$T = T_B + (RT_B^2 / H_B) \ln(X_B) \quad (4.11)$$

where,

T is the liquidus temperature,

$T_{A,B}$  is the melting point of the compound A,B ,

H is the heat of fusion of the individual components,

and

$X_B$  is the mole fraction of component B.

For this calculation, component A was BaO and component B was CaO.

Two diagrams were generated, one based on the melting point of BaO (1915°C) as determined by Schumacher (7), and the second was calculated using the melting point of BaO (2250°C) determined in this investigation. Both diagrams are presented on the same axis in Figure 4.31 for comparison. The temperature at which the liquidus curves

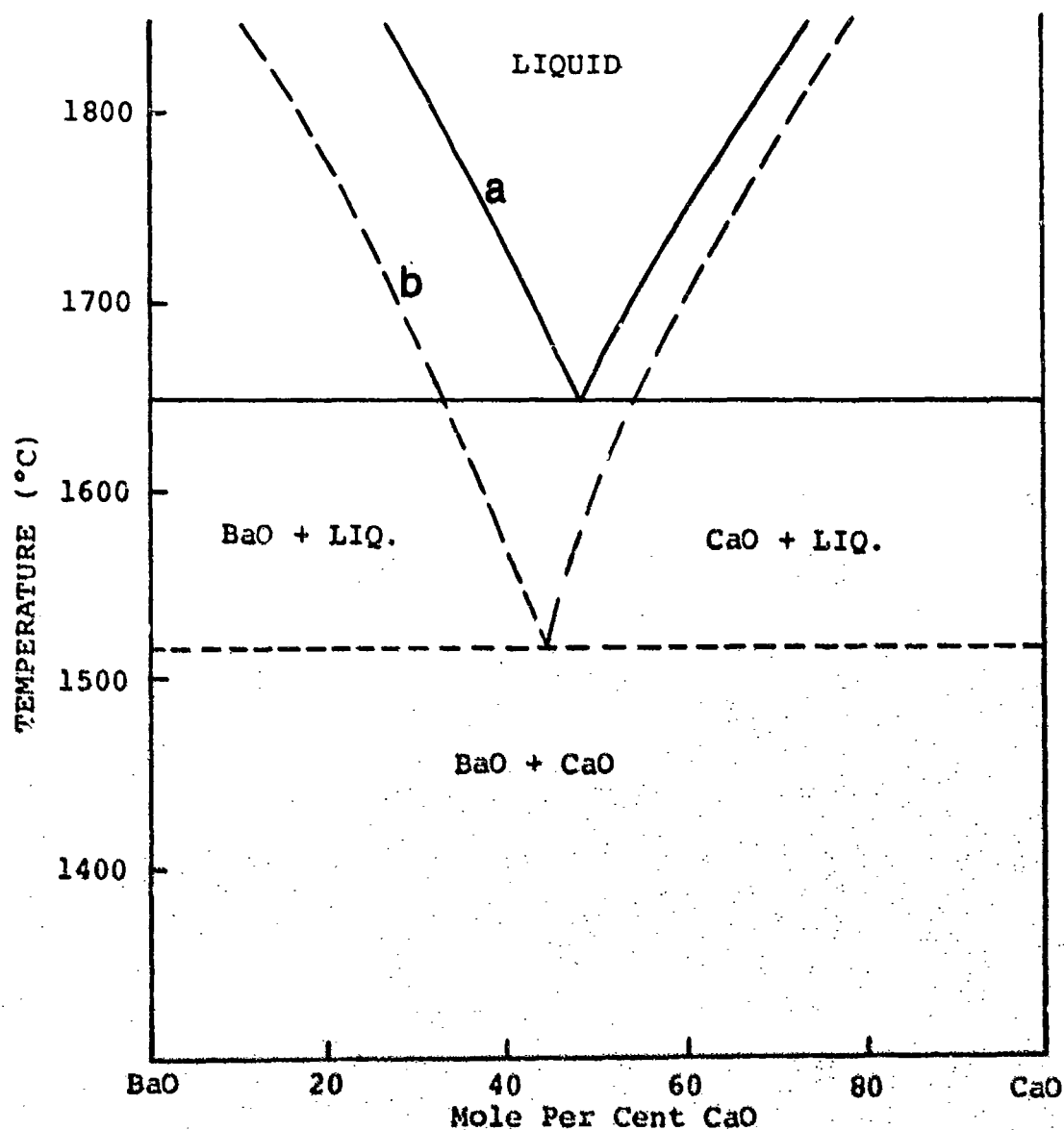


Figure 4.31. Comparison of Eutectic Points in the BaO-CaO System Calculated on the Basis of Melting Point Data for BaO (a) Obtained in this Study, and (b) Published by Schumacher<sup>7</sup>.

intersect is the eutectic temperature and the value of  $X_B$  for this event is the eutectic composition. The eutectic temperature calculated from Schumacher's data was  $1515^{\circ}\text{C}$  and occurred at the composition 56 mole percent BaO-44 mole percent CaO. The eutectic temperature calculated from data obtained in this work was  $1648^{\circ}\text{C}$  and the eutectic composition was shifted to 48 mole percent CaO. This was a result of the higher melting point of BaO used to generate the liquidus curve that extends down from the BaO end.

Both diagrams appear to be reasonable models for the BaO-CaO binary system with respect to actual experimental results from compositions along the constant 15 mole percent  $\text{Al}_2\text{O}_3$  plane. Compositions along this plane, located in the BaO-CaO- $\text{B}_4\text{-}_x\text{C}_x\text{A}$  compatibility triangle, had an average solidus temperature of  $1475^{\circ}\text{C}$ . This is  $173^{\circ}$  below the calculated binary eutectic temperature. Considering the distance from the calculated binary eutectic to the ternary eutectic  $e_3$ , this would seem to be a reasonable temperature difference. It should be noted that extrapolation of the location of the BaO-CaO boundary curve over to the calculated eutectic composition will place the boundary curve at approximately 30 mole

percent CaO along the constant 10 mole percent  $\text{Al}_2\text{O}_3$  plane. Experimental determination of the liquidus curve along this plane would provide the information needed to verify the accuracy of the calculated binary diagram; however, this was beyond the scope of this study.

H. DETERMINATION OF THE REACTION PRODUCTS BETWEEN VARIOUS BARIUM CALCIUM ALUMINATES AND TUNGSTEN AT 1100°

In order to better understand the chemical operation of dispenser cathodes, a preliminary investigation was conducted to determine the reaction products that occur in various mixtures of barium-calcium-aluminates and tungsten powder. The identity and thermal stability of the various phases was determined using x-ray powder diffraction (XRD) after each sample was heat treated for various times in an oxygen-free argon atmosphere.

The first system to be investigated was that of  $\text{B}_3\text{A}-\text{W}$ . The major phases resulting from the reaction were determined to be  $\text{BaAl}_2\text{O}_4$  and  $\text{BaWO}_4$  (Figure 4.32). Note that these phases formed after only two hours of heat treatment at 1100°C. There is also evidence that a minor phase,  $\text{Ba}_2\text{WO}_5$ , was present after 17 hours of heat treatment at 1100°C.

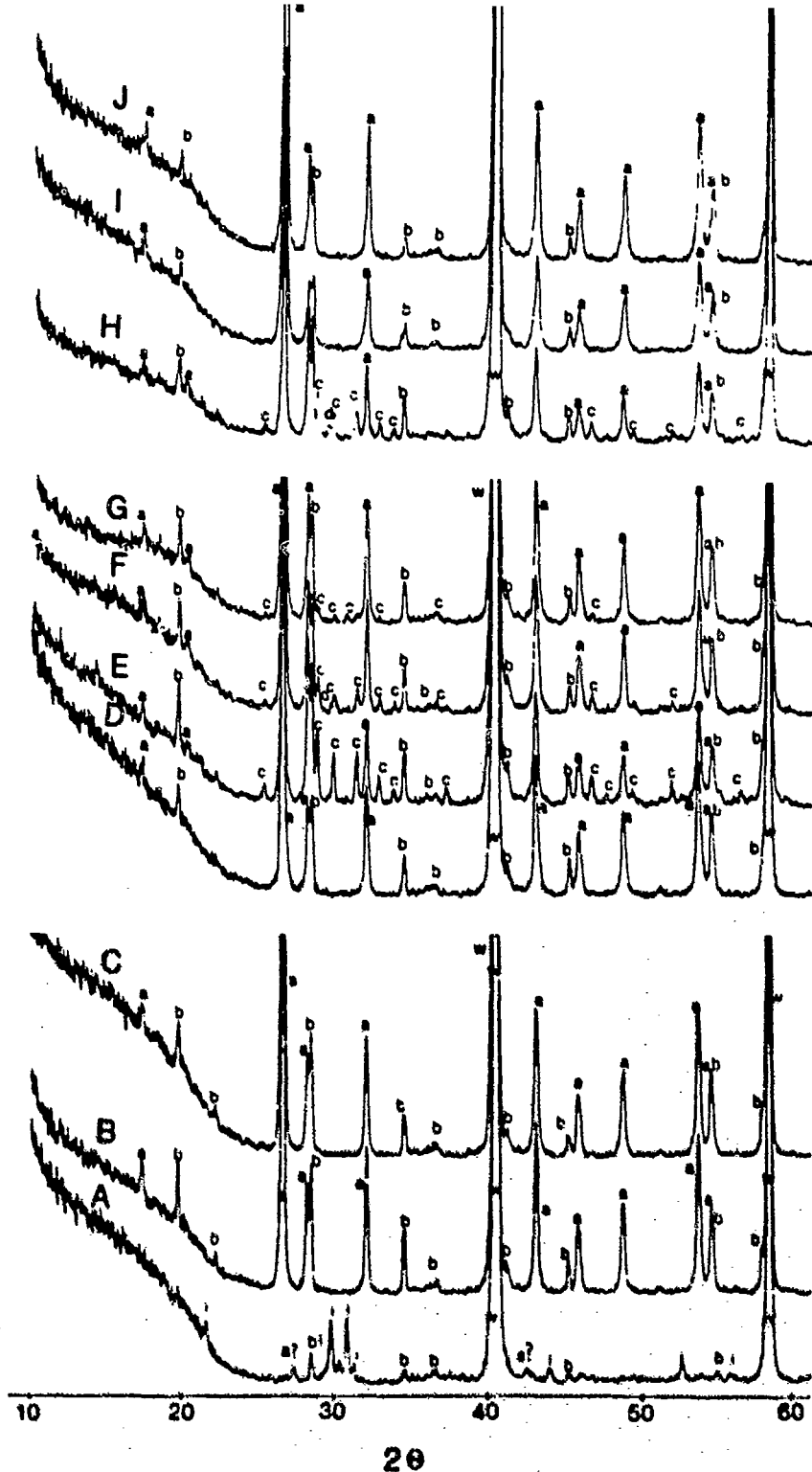


Figure 4.32. X-ray Diffraction Patterns for a  $0.15\text{B}_3\text{A}-0.85\text{W}$  Mixture, Heated to  $1650^\circ\text{C}$  in  $\text{H}_2$  to Fuse the  $\text{B}_3\text{A}$  (Curve A), Then Heat Treated at  $1100^\circ\text{C}$  in Ar for 2, 4, 8, 17, 34, 39, 45, 69, & 90 Hours (Patterns B-J respectively). Phase Designations are: a -  $\text{BaWO}_4$ , b -  $\text{BaAl}_2\text{O}_4$ , & c -  $\text{Ba}_2\text{WO}_5$ .

The next system investigated, which is of commercial significance to the cathode industry, was  $B_4CA-W$ . The major phases identified from the reaction, which were present after only 2 hours of heat treatment at  $1100^{\circ}C$ , were  $BaWO_4$ ,  $Ba_2CaWO_6$  and  $BaAl_2O_4$  (Figure 4.33). The minor phases  $CaWO_4$  and  $Al_2(WO_4)_3$  were also detected after 8 hours of heat treatment at  $1100^{\circ}C$ . It should be noted that the identification of  $Al_2(WO_4)_3$  was based on only one visible reflection and its existence was considered questionable.

Another commercially significant system investigated was  $B_6CA_2-W$ . The major phases identified from this reaction were  $Ba_2CaWO_6$ ,  $BaWO_4$  and  $BaAl_2O_4$  and these phases occurred with only 2 hours of heat treatment at  $1100^{\circ}C$  (Figure 4.34). It was also noted that the minor phase of  $Ba_2WO_5$  was also present intermittently in these XRD patterns.

The final system investigated was the  $B_5C_3A_2-W$ . The major phases, which were present after only 2 hours of heat-treatment at  $1100^{\circ}C$ , were identified as  $Ba_2CaWO_6$ ,  $BaWO_4$ ,  $BaAl_2O_4$  and  $Ca_3WO_6$ . The minor phases,  $CaWO_4$  and  $Al_2WO_4$ , were also detected intermittently throughout the heat treatments. (Figure 4.35).

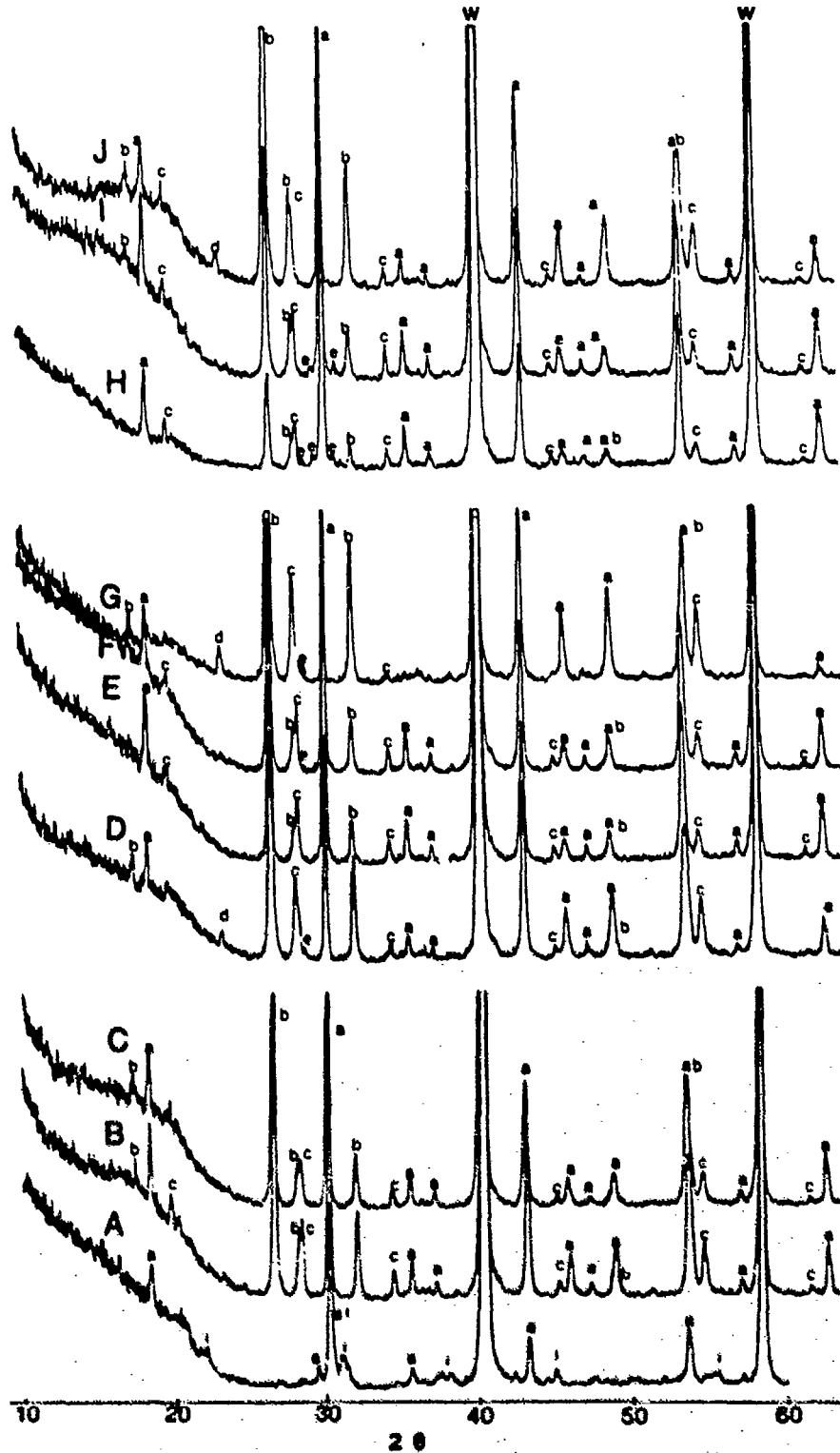


Figure 4.33. X-ray Diffraction Patterns for a 0.15B<sub>4</sub>CA-0.85W Mixture, Heated to 1700°C in H<sub>2</sub> to Fuse the B<sub>4</sub>CA (Pattern A), Then Heat Treated at 1100°C in Ar for 2, 4, 8, 17, 34, 39, 45, 69, & 90 Hours (Patterns B-J respectively). Phase Designations are: a - Ba<sub>2</sub>CaWO<sub>6</sub>, c - BaAl<sub>2</sub>(WO<sub>4</sub>)<sub>3</sub>, e - CaWO<sub>4</sub>, i - B<sub>3</sub>CA, & w - Tungsten.

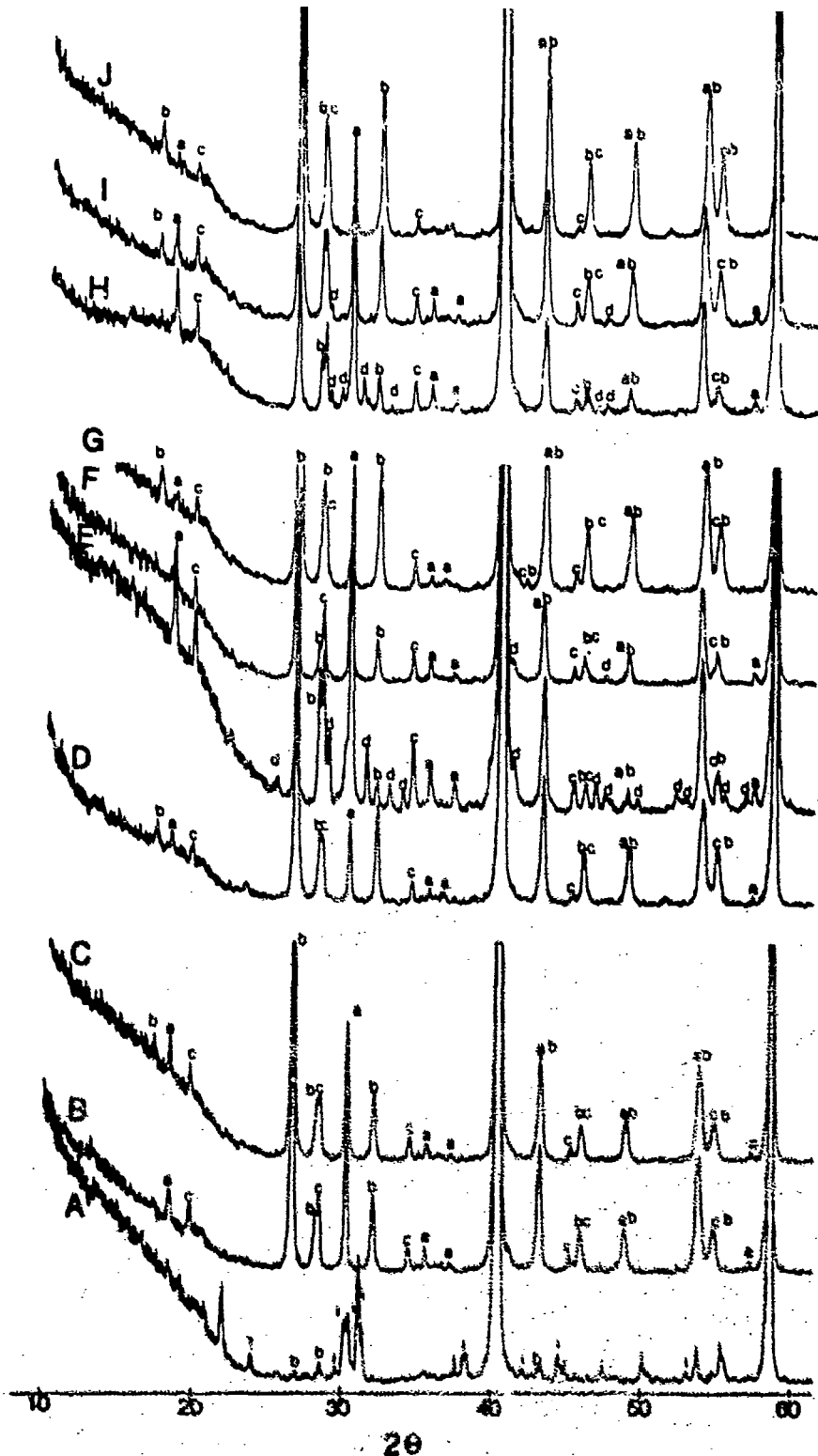


Figure 4.34. X-ray Diffraction Patterns for a  $0.15\text{Ba}_2\text{CaWO}_6$ - $0.85\text{BaWO}_4$  Mixture, Heated to  $1700^\circ\text{C}$  in  $\text{H}_2$  to Fuse the  $\text{Ba}_2\text{CaWO}_6$  (Pattern A), Then Heat Treated at  $1100^\circ\text{C}$  in Ar for 2, 4, 8, 17, 34, 39, 45, 69, & 90 Hours (Patterns B-J respectively). Phase Designations are: a -  $\text{Ba}_2\text{CaWO}_6$ , b -  $\text{BaWO}_4$ , c -  $\text{BaAl}_2\text{O}_4$  and d -  $\text{Ba}_2\text{WO}_5$ .



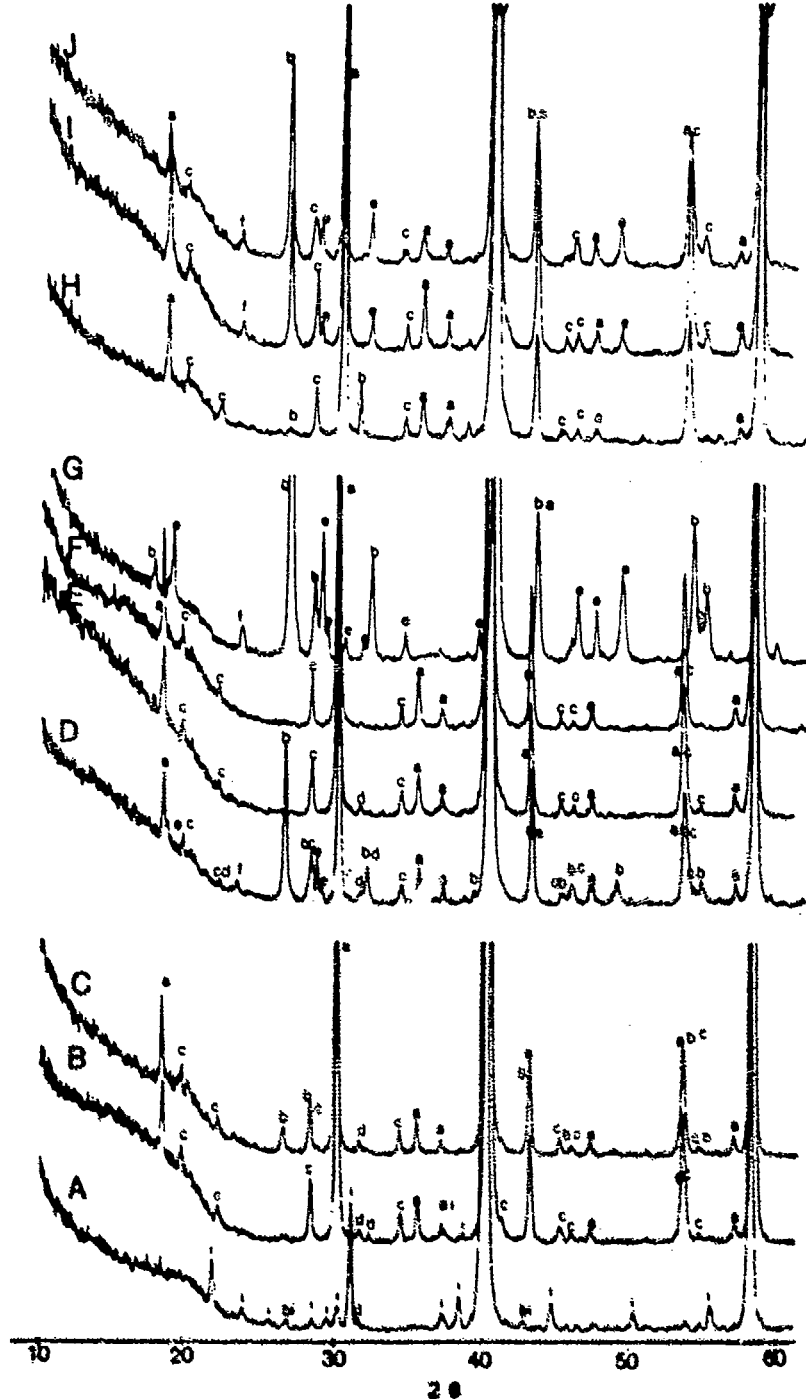


Figure 4.35. X-ray Diffraction Patterns for a  $0.15\text{B}_5\text{C}_3\text{A}_2$ - $0.85\text{W}$  Mixture, Heated to  $1700^\circ\text{C}$  in  $\text{H}_2$  to Fuse the  $\text{B}_5\text{C}_3\text{A}_2$  (Pattern A), Then Heat Treated at  $1100^\circ\text{C}$  in Ar for 2, 4, 8, 17, 34, 39, 45, 69, & 90 Hours (Patterns B-J respectively). Phase Designations are: a -  $\text{Ba}_2\text{CaWO}_6$ , b -  $\text{BaWO}_4$ , c -  $\text{BaAl}_2\text{O}_4$ , d -  $\text{Ca}_3\text{WO}_6$ , e -  $\text{CaWO}_4$ , f -  $\text{Al}_2(\text{WO}_4)_3$ , i -  $\text{B}_5\text{C}_3\text{A}_2$ .

## CHAPTER V

### CONCLUSIONS

The sub-solidus and liquid/solid equilibria of the high-baria portion of the BaO-CaO-Al<sub>2</sub>O<sub>3</sub> system has been determined. This also includes delineation of the unit cells of the phases, B<sub>3</sub>A, B<sub>4-x</sub>C<sub>x</sub>A (Type I) and B<sub>4-x</sub>C<sub>x</sub>A (Type II). The melting point of BaO was redetermined and a calculated BaO-CaO binary phase diagram was generated using molal freezing-point depression theory.

Parametric treatment of x-ray powder diffraction data obtained from B<sub>3-x</sub>C<sub>x</sub>A solid solution compositions gave a solubility of 18.75 mole percent Ca<sup>2+</sup> over the temperature range 1100°C to 1475°C. The solubility of Ca<sup>2+</sup> in B<sub>4-x</sub>C<sub>x</sub>A was determined to be 20.5 mole percent between 1100°C and 1475°C. At 1100°C, substitution of Ca<sup>2+</sup> for Ba<sup>2+</sup> in the crystal structure of B<sub>4-x</sub>C<sub>x</sub>A produced a lowering of the crystallographic symmetry of the unit cell. This consequently resulted in a two-phase miscibility gap along the solid solution series extending from 8 to 13.4 mole percent CaO along the 20 mole percent Al<sub>2</sub>O<sub>3</sub> plane.

B<sub>4-x</sub>C<sub>x</sub>A solid solutions were found to exist as two

polymorphic modifications. The high-temperature form (Type I), stable above 1475°C, possesses orthorhombic symmetry; the low-temperature form (Type II), stable below 1475°C, has a monoclinic unit cell. The polymorphic inversion involved with the two forms was found to be reconstructive. Pure  $B_3A$  exhibits a rapid, reversible, displacive-type polymorphic phase transformation at 366°C. The heat of transformation associated with the inversion is 0.11 calories/gm. Substitution of  $Ca^{2+}$  for  $Ba^{2+}$  in the structure lowers the heat of transformation and completely eliminates the inversion at the solubility limit (18.75 mole percent CaO.) It was also found that pure  $B_3A$  crystals possess an apparent uniaxial negative optical indicatrix under white (polychromatic) light.  $Ca^{2+}$  substitution reduces the birefringence of the crystals, and crystals of the limit solid solution composition (18.75 mole percent CaO) were completely isotropic. Similarly,  $Ca^{2+}$  substitution reduced the crystallographic anisotropy of the unit cell by elongation of the b-axis.

Four ternary eutectics are located in the portion of the system bounded by  $BaAl_2O_4$ -BaO-CaO. The eutectic temperatures ranged from 1475°C to 1555°C. It was found

that the liquidus temperatures of both  $B_{3-x}C_xA$  and  $B_{4-x}C_xA$  solid solutions increased with increasing calcium content. Crystallization from the melt of compositions located in the CaO primary phase field produced well-defined CaO dendrites. Lamellar structures were observed for slightly off-eutectic compositions.

The melting point of BaO was determined by in-situ oxidation of barium metal using the tungsten-strip microfurnace. The measured melting point was  $2250^{\circ}\text{C}$  determined by visual observation of melting and supported by the presence of dynamic supercooling detected from the cooling curve. Molal freezing-point depression theory and experimentally determined melting points, along with heats of fusion of both BaO and CaO, were used to generate BaO-CaO binary phase diagrams. Using the melting point of BaO determined in this investigation, the calculated eutectic temperature was  $1648^{\circ}\text{C}$  and the eutectic composition was 48 mole percent CaO.

## APPENDIX

### XRD DATA FOR VARIOUS BARIUM CALCIUM ALUMINATE COMPOSITIONS

This section contains the XRD data for all powder patterns presented in this document. The patterns used for the unit cell determinations are also given.

Table A-1. XRD Data for B<sub>3</sub>A Quenched from above Liquidus.

Line No.	2 $\theta$ (degrees)	d (Å)	Intensity (CPS)	Relative Intensity
1	21.58	4.114	300	33
2	21.90	4.054	90	10
3	23.23	3.823	80	8
4	23.96	3.710	80	8
5	25.61	3.475	140	15
6	25.79	3.451	80	8
7	26.17	3.402	80	8
8	26.33	3.381	90	10
9	26.59	3.349	80	8
10	29.54	3.021	160	17
11	29.98	2.977	180	20
12	30.08	2.968	440	48
13	30.14	2.962	300	33
14	30.62	2.917	900	100
15	30.68	2.911	640	71
16	31.03	2.879	200	22
17	37.31	2.408	280	31
18	38.08	2.361	120	13
19	38.19	2.354	110	12

Table A-1. (concluded)

Line No.	$2\theta$ (degrees)	$d$ (Å)	Intensity (CPS)	Relative Intensity
20	38.36	2.344	110	12
21	38.47	2.338	100	11
22	43.77	2.066	150	16
23	43.90	2.060	200	22
24	44.59	2.030	140	15
25	48.63	1.870	110	12
26	49.27	1.847	110	12
27	49.88	1.826	140	15
28	53.77	1.703	190	21
29	54.13	1.692	80	8
30	54.28	1.688	80	8
31	54.91	1.670	140	15
32	56.64	1.623	100	11
33	57.49	1.601	80	8
34	57.63	1.598	80	8
35	57.81	1.593	80	8
36	62.01	1.495	80	8
37	63.72	1.459	100	11
38	63.91	1.455	80	8
39	64.97	1.434	100	11

Table A-2. XRD Data for  $B_{3.70}C_{0.30}A$  Quenched from  $1100^{\circ}C/1$  Hour Soak.

Line No.	$2\theta$ (degrees)	d (Å)	Intensity (CPS)	Relative Intensity
1	16.71	5.300	180	18
2	17.10	5.180	170	17
3	19.93	4.451	240	24
4	22.01	4.034	500	50
5	24.13	3.684	110	11
6	25.79	3.451	180	18
7	26.89	3.312	170	17
8	27.93	3.191	190	19
9	29.87	2.988	1000	100
10	30.83	2.897	550	55
11	31.77	2.814	540	54
12	33.95	2.638	110	11
13	35.43	2.531	90	9
14	37.00	2.427	200	20
15	37.78	2.379	240	24
16	44.83	2.019	360	36
17	44.93	2.015	270	27
18	46.47	1.952	110	11
19	49.51	1.839	140	14



Table A-2. (concluded)

Line No.	$2\theta$ (degrees)	$d$ (Å)	Intensity (CPS)	Relative Intensity
20	51.12	1.785	110	11
21	52.41	1.744	120	12
22	54.17	1.691	190	19
23	55.38	1.657	240	24
24	62.06	1.494	110	11

Table A-3. XRD Data for B<sub>4</sub>A Quenched from 1100°C/1 Hour Soak.

Line No.	2 $\theta$ (degrees)	d (Å)	Intensity (CPS)	Relative Intensity
1	16.81	5.269	180	18
2	19.43	4.564	160	16
3	21.31	4.165	170	17
4	21.70	4.091	230	23
5	25.50	3.490	140	14
6	26.58	3.350	140	14
7	29.32	3.043	1000	100
8	29.89	2.986	140	14
9	30.41	2.936	470	47
10	30.83	2.897	110	11
11	31.49	2.838	330	33
12	33.58	2.666	100	10
13	35.06	2.557	90	9
14	35.76	2.508	100	10
15	36.45	2.462	130	13
16	37.31	2.408	130	13
17	38.32	2.346	90	9
18	39.60	2.273	220	22
19	41.51	2.173	70	7

Table A-3. (concluded)

Line No.	$2\theta$ (degrees)	$d$ (Å)	Intensity (CPS)	Relative Intensity
20	42.66	2.112	70	7
21	43.51	2.078	80	8
22	44.40	2.038	240	24
23	48.96	1.858	100	10
24	51.11	1.785	140	14
25	51.78	1.764	100	10
26	53.80	1.702	160	16
27	53.92	1.698	130	13
28	55.12	1.664	120	12
29	55.38	1.657	100	10
30	57.01	1.613	60	6
31	58.22	1.583	100	10
32	58.44	1.577	90	9

Table A-4. XRD Data for  $B_{2.5}C_{0.5}A$  Quenched from above Liquidus.

Line No.	$2\theta$ (degrees)	d (Å)	Intensity (CPS)	Relative Intensity
1	20.74	4.279	85	8
2	21.85	4.064	680	68
3	23.93	3.715	250	25
4	25.62	3.473	130	13
5	26.76	3.328	120	12
6	28.43	3.136	190	19
7	29.52	3.023	170	17
8	29.97	2.978	150	15
9	30.31	2.946	220	22
10	30.53	2.920	220	22
11	31.10	2.873	1000	100
12	38.23	2.352	310	31
13	38.47	2.338	300	30
14	39.49	2.279	130	13
15	40.36	2.232	80	8
16	41.05	2.190	150	15
17	41.43	2.177	90	9
18	42.59	2.120	100	10
19	44.43	2.037	300	30

Table A-4. (concluded)

Line No.	$2\theta$ (degrees)	$d$ (Å)	Intensity (CPS)	Relative Intensity
20	44.92	2.016	280	28
21	45.55	1.989	110	11
22	47.26	1.921	100	10
23	50.00	1.822	180	18
24	50.98	1.789	90	9
25	51.97	1.758	60	6
26	53.62	1.707	70	7
27	55.18	1.663	390	39

Table A-5. XRD Data for B<sub>3</sub>CA Quenched from 1100°C/1 Hour Soak.

Line No.	2θ (degrees)	d (Å)	Intensity (CPS)	Relative Intensity
1	20.65	4.297	240	45
2	20.93	4.240	170	32
3	22.91	3.878	300	56
4	29.21	3.054	120	22
5	30.12	2.964	300	56
6	30.50	2.928	530	100
7	30.63	2.916	300	56
8	30.72	2.907	360	67
9	31.06	2.876	230	43
10	31.38	2.848	500	94
11	37.34	2.406	150	28
12	37.66	2.386	250	47
13	38.18	2.355	250	47
14	42.21	2.139	150	28
15	42.75	2.113	110	20
16	44.54	2.032	120	22
17	44.83	2.019	180	33
18	44.94	2.015	180	33
19	48.14	1.888	80	15

Table A-5. (concluded)

Line No.	$2\theta$ (degrees)	$d$ (Å)	Intensity (CPS)	Relative Intensity
20	50.03	1.821	80	15
21	50.50	1.803	100	18
22	50.64	1.801	100	18
23	54.13	1.692	130	24
24	54.88	1.671	120	22
25	55.83	1.645	110	20
26	56.08	1.638	90	16
27	56.53	1.626	140	26

Table A-6. XRD Data for  $B_{2.38}C_{0.63}A$  Quenched from 1100°C/1 Hour Soak.

Line No.	$2\theta$ (degrees)	$d$ (Å)	Intensity (CPS)	Relative Intensity
1	20.18	4.396	190	20
2	20.79	4.268	120	13
3	22.02	4.033	340	36
4	25.80	3.450	80	8
5	26.85	3.317	70	7
6	27.89	3.196	70	7
7	29.99	2.976	920	100
8	30.45	2.933	150	16
9	30.70	2.900	90	9
10	30	2.889	230	25
11	30	2.855	130	14
12	31.74	2.816	280	30
13	32.26	2.766	60	6
14	32.32	2.750	60	6
15	33.06	2.635	50	5
16	37.17	2.416	150	17
17	37.30	2.409	100	10
18	37.84	2.375	170	18
19	38.13	2.358	60	6



Table A-6. (concluded)

Line No.	$2\theta$ (degrees)	$d$ (Å)	Intensity (CPS)	Relative Intensity
20	38.42	2.340	70	7
21	40.82	2.208	110	11
22	41.03	2.197	70	7
23	42.18	2.140	50	5
24	44.65	2.027	150	16
25	44.89	2.017	240	26
26	46.09	1.967	40	4
27	46.95	1.933	50	5
28	49.66	1.834	90	9
29	49.98	1.823	60	6
30	51.04	1.787	60	6
31	52.05	1.755	90	9
32	52.62	1.737	80	8
33	54.39	1.685	110	11
34	55.38	1.657	130	14
35	62.37	1.487	60	6

Table A-7. XRD Data for B<sub>3</sub>CA Quenched from above the Liquidus.

Line No.	2 $\theta$ (degrees)	d (Å)	Intensity CPS	Relative Intensity
1	20.70	4.287	940	94
2	22.09	4.020	420	42
3	30.45	2.933	1000	100
4	31.05	2.877	350	35
5	31.78	2.813	270	27
6	37.63	2.388	210	21
7	38.08	2.361	230	23
8	42.03	2.147	490	49
9	43.22	2.091	50	5
10	43.36	2.085	50	5
11	44.67	2.026	50	5
12	45.02	2.011	200	20
13	48.00	1.893	170	12

Table A-8. XRD Data for  $B_{3.70}C_{0.92}A$  Quenched from  
1100°C/1 Hour Soak.

Line No.	$2\theta$ (degrees)	$d$ (Å)	Intensity (CPS)	Relative Intensity
1	20.02	4.431	50	9
2	20.79	4.268	30	5
3	21.98	4.040	200	36
4	24.17	3.679	20	3
5	25.77	3.454	30	5
6	26.84	3.318	30	5
7	29.97	2.978	555	100
8	30.44	2.933	30	5
9	30.86	2.895	150	27
10	31.30	2.855	30	5
11	31.63	2.826	180	32
12	32.22	2.775	30	5
13	33.93	2.639	20	3
14	37.12	2.419	70	12
15	37.36	2.404	70	12
16	37.82	2.376	100	18
17	40.82	2.208	50	9
18	44.80	2.021	140	25
19	49.56	1.837	30	5

Table A-8. (concluded)

Line No.	$2\theta$ (degrees)	$d$ (Å)	Intensity (CPS)	Relative Intensity
20	54.24	1.689	50	9
21	55.37	1.657	50	9
22	62.22	1.490	40	7
23	64.94	1.434	50	9

Table A-9. XRD Data for  $B_{3.47}C_{0.79}A$  Quenched from  $1100^{\circ}C$ /1 Hour Soak.

Line No.	$2\theta$ (degrees)	$d$ (Å)	Intensity (CPS)	Relative Intensity
1	22.28	3.986	90	11
2	20.78	4.270	50	6
3	22.08	4.022	290	38
4	24.27	3.664	20	2
5	25.82	3.447	20	2
6	30.16	2.960	760	100
7	30.52	2.926	210	27
8	30.76	2.904	110	14
9	30.97	2.884	200	26
10	31.38	2.848	170	22
11	31.72	2.818	200	26
12	32.49	2.753	30	3
13	34	2.634	30	3
14	37.31	2.408	100	13
15	37.68	2.385	70	9
16	37.93	2.370	110	14
17	38.2	2.353	70	9
18	41.18	2.190	70	9
19	42.25	2.137	40	5

Table A-9. (concluded)

Line No.	$2\theta$ (degrees)	$d$ (Å)	Intensity (CPS)	Relative Intensity
20	44.63	2.028	150	19
21	44.91	2.016	170	22
22	47.13	1.926	40	5
23	49.72	1.832	50	6
24	52.37	1.745	30	3
25	52.82	1.731	40	5
26	54.48	1.682	60	7
27	55.43	1.656	70	9
28	55.57	1.652	60	7
29	62.48	1.485	30	3
30	64.97	1.434	30	3

## BIBLIOGRAPHY

1. J. E. Lambert, "Development of a Phase Diagram for the High-Barium Portion of the Barium Aluminate Binary System," Masters Thesis, School of Ceramic Engineering, Georgia Institute of Technology, Atlanta, Georgia (1983).
2. W. P. White, "Melting Point Determinations," Am. J. Sci. 28, 453-89 (1909).
3. E. T. Carlson, "The System  $\text{CaO-B}_2\text{O}_3$ ," J. Res. NBS 9, 827-9 (1932).
4. H. T. Smyth, "Temperature Distribution During Mineral Inversion and Its Significance in Differential Thermal Analysis," J. Am. Cer. Soc. 34, 221-4 (1951).
5. L. G. Wisnyi, "The High Alumina Phases in the System Lime-Alumina," Doctoral Dissertation, School of Ceramic Engineering, Rutgers University, New Brunswick, New Jersey (1955).
6. R. E. Latta and R. E. Fryxell, "Determination of Solidus-Liquidus Temperatures in the  $\text{UO}_2$  x System," J. Nuclear Materials 35, 195-210 (1970).
7. E. E. Schumacher, "Melting Points of Barium, Strontium, and Calcium Oxides," J. Am. Chem. Soc. 48, 396-402 (1926).
8. H. S. Roberts and G. W. Morey, "A Microfurnace for Temperatures Above  $1000^\circ\text{C}$ ," J. Res. NBS 1, 576-80 (1930).
9. M. L. Keith and R. Roy, "Structural Relations Among Double Oxides of Trivalent Elements," American Mineralogist 39, 1-7 (1954).
10. D. E. Rase and R. Roy, "Phase Equilibria in the System  $\text{BaO-TiO}_2$ ," J. Am. Cer. Soc. 38, 104 (1955).

11. D. Asselanis, "Investigation of Solidus and Liquidus Temperatures for the High Barium Oxide Portion of the  $\text{BaO-CaO-Al}_2\text{O}_3$  System," Master's Thesis, School of Ceramic Engineering, Georgia Institute of Technology, Atlanta, Georgia (1979).
12. J. O. Tarter, "Melting Characteristics of Barium Calcium Aluminate Dispenser Cathode Impregnants," Master's Thesis, Georgia Institute of Technology, Atlanta, Georgia (1982).
13. H. Wartenberg and H. J. Rensch, Anorg. Allg. Chem. 207, 1 (1932).
14. N. A. Toropov, Dolk. Akad. Nauk. SSSR 1, 147 (1935).
15. S. Wallmark and A. Westgren, "X-Ray Analysis of Barium Aluminates," Ark. Kemi. Mineral Geol. 12B, 1-4 (1937).
16. E. T. Carlson, T. S. Chaconas, and L. S. Wells, "Study of the System Barium Oxide-Aluminum Oxide-Water at  $30^\circ\text{C}$ ," J. Res. NBS 45, 381-98 (1950).
17. N. A. Toropov and F. J. Galachow, Dolk. Akad. Nauk. SSSR 82, 69 (1952).
18. G. Pirt, Radex-Randschau 4, 198-201 (1960).
19. P. Appendino, "Research on the More Basic Region of the System  $\text{BaO-Al}_2\text{O}_3$ ," Ann. Chem. 61, 822-30 (1971).
20. J. Day, "Phase Relationships and Long-Term Stability in the High Zirconia Region of the Calcia-Alumina-Zirconia System," Masters's Thesis, School of Ceramic Engineering, Georgia Institute of Technology, Atlanta, Georgia (1976).
21. F. M. Lea and C. H. Desch, The Chemistry of Cement and Concrete, 2nd ed., p. 52, Edward Arnold Co., London (1956).



22. R. W. Nurse, J. H. Welch, and A. J. Majumdar, "The  $\text{CaO-Al}_2\text{O}_3$  System in a Moisture-Free Atmosphere," Tran. Brit. Cer. Soc. 64, 6, 409-418 (1965).
23. P. Appendino, "Research on the Ternary System  $\text{CaO-BaO-Al}_2\text{O}_3$ ," Ceramurgia Anno 11 Numerc 2, pp. 103-6 (1972).
25. V. V. Lapin, Dolk. Akad. Nauk. SSSR 96, 1037 (1954).
26. C. Brisi and M. Montorsi, Ann. Chim. 52, 785-94 (1962).
27. F. Massazza, Ann. Chim. 53, 1002-17 (1963).
28. G. M. Wolten, "An Appraisal of the Ternary System  $\text{BaO-CaO-Al}_2\text{O}_3$ ," Interim Report # SD-TR-80-67 (1980).
29. E. M. Levin and H. F. McMurdie, "The System  $\text{BaO-B}_2\text{O}_3$ ," J. Am. Cer. Soc. 32, 100 (1949).
30. E. H. Baker, "The Barium Oxide-Carbon Dioxide System in the Pressure Range 0.01 to 450 Atmospheres," J. Chem. Soc. (London) 137, 699-704 (1964).
31. T. S. Sneider and C. L. McDaniel, "The  $\text{BaO-Pt}$  System in Air," J. Amer. Cer. Soc. 52, 518-19 (1969).
32. J. J. Lander "The Phase System  $\text{BaO-NiO}$ ," J. Amer. Chem. Soc. 73, 2450-2 (1951).
33. M. G. Inghram, W. A. Chupka, and R. F. Porter "Mass Spectrometric Study of Barium Oxide Vapor," J. Chem. Phys. 23, 2159-65 (1955).
34. K. Hilpert and H. Gerads, High Temp. Sci. 7, 11 (1975).
35. K. Hilpert, et al. "Mass Spectrometric Study of the Vaporation of  $\text{Ba}_3\text{Al}_2\text{O}_6$  and  $\text{BaAl}_2\text{O}_9$ ," High Temp. Sci. 7, 159-166 (1975).
36. R. A. Lipeles and H. K. A. Kan, "Chemical Stability of Barium Calcium Aluminate Dispenser Cathode Impregnants," Appl. Surf. Sci. 16, 189 (1983).

37. P. Mondal and J. W. Jeffery, "The Crystal Structure of Tricalcium Aluminate,  $\text{Ca}_3\text{Al}_2\text{O}_6$ ," Acta. Cryst. B31, 68 (1975).
38. D. N. Hill, Georgia Institute of Technology, Personal Communication, June 1984.
39. E. M. Levin, C. R. Robbins, and H. F. McMurdie, Phase Diagrams for Ceramist, American Ceramic Society, 569 (1964).
40. B. D. Cullity, Elements of X-ray Diffraction, 98, 2nd ed., Addison-Wesley Pub. Co., Mass. (1978).
41. D. Louer and R. Vargas, J. Appl. Cryst. 15, 542-545 (1982).
42. F. P. Glasser, "Polymorphism of  $\text{Ba}_3\text{Al}_2\text{O}_6$  and Solid Solution between  $\text{Ba}_3\text{Al}_2\text{O}_6$ ,  $\text{Sr}_3\text{Al}_2\text{O}_6$ , and  $\text{Ca}_3\text{Al}_2\text{O}_6$ ," Cement and Concrete Res., 4, 745-752 (1974).



## *MISSION of Rome Air Development Center*

RADC plans and executes research, development, test and selected acquisition programs in support of Command, Control, Communications and Intelligence (C<sup>3</sup>I) activities. Technical and engineering support within areas of competence is provided to ESD Program Offices (POs) and other ESD elements to perform effective acquisition of C<sup>3</sup>I systems. The areas of technical competence include communications, command and control, battle management, information processing, surveillance sensors, intelligence data collection and handling, solid state sciences, electromagnetics, and propagation, and electronic, maintainability, and compatibility.